

# Skoltech

Skolkovo Institute of Science and Technology

## Proceedings of the Skoltech Energy PhD Seminar

2018/19

$\frac{2(n-m)^2}{m^2n^2} \cdot \frac{2(n-m)^2}{m^2n^2} \cdot \frac{m^2n^2}{mn} = mn \cdot 4 = \frac{4mn}{m^2n^2}$ 
 $\Rightarrow \frac{(x-2)^2}{9} - \frac{(y-3)^2}{16} = 1 \quad e = \frac{c}{a}$ 
 $\frac{2(n-m)}{mn} \cdot \frac{2}{-(m-n)} = 5$

$y - 161 = 0$ 
 $5) \frac{2(n-m)^2}{m^2n^2} \cdot \frac{(m-n)^2}{2mn} \cdot \frac{54}{-18} = \frac{2(n-m)^2}{m^2n^2} \cdot \frac{(m^2-n)(m+n)}{2mn}$ 
 $c = 3$   
 $a = 2$

$S = -5k \cdot b$   
 $AD \perp CB$ 
 $\begin{cases} 5 = -k \cdot 5 + b \\ 1 = k \cdot 3 + b \end{cases} \Leftrightarrow \begin{cases} 5 = -5k + b \\ 1 = 3k + b \end{cases}$

$2 - 54y - 161 = 0$ 
 $5 = -5k + b$ 
 $\begin{cases} -5k + b = 5 \\ 3k + b = 1 \end{cases}$

$\frac{(n^2-m^2)}{m^2n^2} - \frac{4mn}{m^2n^2} = \frac{2(n^2+m^2)}{m^2n^2} - c \cdot \frac{\beta^2}{4a}$ 
 $\bar{n} = (-4, 11, -3)$ 
 $1 = 3k + b$

$\alpha \left( \frac{x+b}{2a} \right)^2 - c \cdot \frac{\beta^2}{4a}$ 
 $\alpha = \sqrt{(x_2 - x_1)^2 + (y_2 - y_1)^2}$

$k + c = 0$ 
 $l > 1$ 
 $Ex. c = 6$   
 $a = 3$

$y^2 - 64x - 54y - 161 = 0$ 
 $16(x - \frac{64}{32})^2 = 16(x-2)^2$ 
 $\frac{(m^2-n)(m+n)}{2mn}$

$\frac{2(n-m)}{mn} \cdot \frac{2}{-(m-n)}$ 
 $16(x-2)^2 - 9(y-3)^2 = 144$ 
 $\frac{(x-2)^2}{9} - \frac{(y-3)^2}{16} = 1$ 
 $b = x = a/c$

$3) \frac{4}{m-n} \cdot \frac{m-n}{mn} = \frac{4}{mn}$ 
 $\frac{2(n^2+m^2)}{m^2n^2} - \frac{4}{mn} = \frac{2(n^2+m^2)}{m^2n^2} - \frac{4mn}{m^2n^2}$

$-54y - 161 = 0$ 
 $e = \frac{c}{a}$

$\frac{-3/2}{2/1,5}$ 
 $\frac{10}{10}$ 
 $\frac{10}{10}$ 
 $l = \frac{6}{3} = 2$ 
 $\frac{m^2n^2}{m^2n^2} = 1 \cdot \frac{2(n^2+m^2)}{m^2n^2} = \frac{2(n^2+m^2)}{m^2n^2}$

$16x^2 - 9y^2 - 64x - 54y - 161 = 0$ 
 $16x^2 - 64x - 161 = 0$ 
 $c = \frac{\beta^2}{4a} - 9y^2 - 54y - 161 = 0$

$-161 = 0$ 
 $\frac{x-x_1}{m} = \frac{y-y_1}{n} = \frac{z-z_1}{p}$ 
 $16(x - \frac{64}{32})^2 = 16(x-2)^2$ 
 $\frac{(m^2-n)(m+n)}{2mn}$

$\alpha \left( \frac{x+b}{2a} \right)^2 - n$ 
 $(\bar{r} = (m, n, p))$ 
 $\frac{4}{1} \cdot \frac{1}{mn} = \frac{4}{mn}$ 
 $\frac{2(n-m)^2}{m^2n^2} \cdot y$ 
 $A(-5, 5) \Rightarrow 5 = -k \cdot 5 + b$   
 $B(3, 1) \Rightarrow 1 = k \cdot 3 + b$

$V_1 + V_2 + V_3 + V_5 = V_a - r_1 \cdot I$   
 $+ V_1 + E_1 + V_2 - r_2 \cdot I +$   
 $+ V_3 - E_2$   
 $I(r_1 + r_2) = V_a - V_5 + E_1$   
 $I = \frac{V_a - V_5 + E_1 - E_2}{r_1 + r_2}$

$E = V_1 - V_2$ 
 $V_1/B \cdot V_a - r_1 \cdot I$ 
 $U = I_2 = V_1 - V_2$ 
 $V_2 = V_1 + E_1$ 
 $V_3 = V_2 - r_2 \cdot I$

$V_a$ 
 $r_1$ 
 $I$ 
 $E_1$ 
 $r_2$ 
 $I$ 
 $E_2$ 
 $V_5$

$V_1$ 
 $V_2$ 
 $V_3$ 
 $V_4$ 
 $V_5$ 
 $V_6$ 
 $V_7$ 
 $V_8$ 
 $V_9$ 
 $V_{10}$ 
 $V_{11}$ 
 $V_{12}$

$2 = \frac{V}{I}$ 
 $r = \frac{V}{I}$ 
 $x = \pm \sqrt{z^2 - p^2}$ 
 $\frac{V_3 - V_1 + E_1}{r_1} = g_1 \cdot (V_3 - V_1 + E_1)$ 
 $g = \frac{1}{r}$

# Skoltech

Skolkovo Institute of Science and Technology

## Proceedings of the Skoltech Energy PhD Seminar

2018/19

# Proceedings of the Skoltech Energy PhD Seminar 2018/19

**T**HE *Proceedings* is a collection of the original research papers written by the participants of the third Skoltech PhD Energy Seminar in the 2018-2019 academic year.

The Skoltech PhD Energy Seminar unites students enrolled on Skoltech PhD Programs associated with the Centers of Energy Science and Technology, Hydrocarbon Recovery, Photonics and Quantum Materials, and eventually some others.

The Seminar promotes the exchange of knowledge, methodologies, and research questions across the fundamentally different scientific areas in accordance with the Skoltech vision of multidisciplinary research and education oriented to innovation. The main goal of the Seminar is to create and maintain interdisciplinary links between students doing research related to energy resources, generation, storage and distribution, as well as methods, models, devices and materials for efficient energy use.

Besides its immediate research-oriented goal, the pragmatic aim of the Seminar is to engage PhD students in professional academic communication activities based on the principles of ethics and peer review. During the Seminar, students were required to present the results of their research, write an article for the *Proceedings* according to a template, and peer review two papers submitted by the Seminar participants.

In preparation for the *Proceedings*, each paper was anonymously reviewed by two peers and checked by a language instructor. The final versions had to incorporate comments from the referees and editors to be accepted for the *Proceedings*.

We believe that this exercise provides the students with useful experience as well as results in the *Proceedings* of reasonable quality. We appreciate that the students may prefer to disseminate their outstanding research results in more wimpactful publications.

We also use this occasion to congratulate the participants of the past Skoltech PhD Energy Seminars, Evgeniya Gilshteyn and Tatiana Bondarenko, who were the first to receive the Skoltech PhD degree in *Materials Science and Engineering and Petroleum Engineering*, respectively.

We appreciate the efforts and devotion of all the Seminar attendees and the contributions of their supervisors. We are grateful to the Skoltech Dean of Education Dr. Anna Derevnina for supporting the Seminar initiative. We also thank Mrs. Ksenia Sattarova for preparing this document for publication.

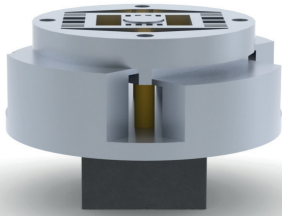
**Alexei Buchachenko** (Seminar instructor)

**Anna Sharova**

**Elizaveta Tikhomirova**

August 2019

## RESEARCH ARTICLE:



## Design of an optimized nanostage for high-speed atomic force microscope

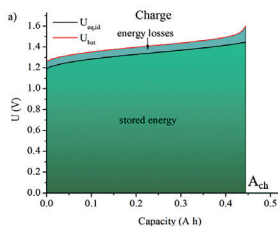
**Maria Zhilyaeva, Fardad Azarmi, Iman Soltani Bozchalooi, Kamal Youcef-Toumi**

An Optimized Nanostage for high-speed Atomic Force Microscope is developed. During the work, all specification requirements were fulfilled/exceeded and validated with Finite Element Analysis. The design offers:

- X, Y bandwidth 6.8 kHz
- X, Y range 5.4x5.0  $\mu\text{m}$
- Z-axis bandwidth 2.4 kHz
- Z-axis range 13.5  $\mu\text{m}$

08

## RESEARCH ARTICLE:



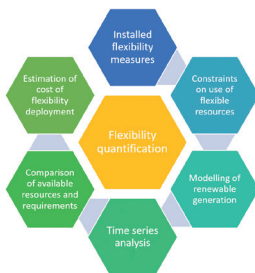
## Energy efficiency analysis of vanadium redox flow battery cell

**M. Pugach, A. Bischi**

- A new approach for estimation of cell energy efficiency is proposed
- Energy losses are investigated for charge and discharge processes individually
- Contribution of internal processes to the energy losses is analysed

20

## SMALL REVIEW:



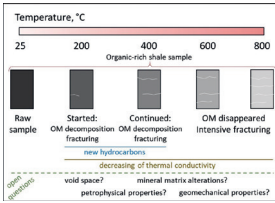
## Review of energy systems flexibility measures and quantification approaches

**Alvaro Gonzalez-Castellanos, Aldo Bischi**

- The paper presents an analysis of the flexibility assessment in energy systems
- The main flexibility measures for an energy system are presented
- A review of the flexibility quantification in an energy system are described
- Based on the analyzed flexibility metrics, research challenges and future directions are provided

30

**SMALL REVIEW:**



**Alterations of organic-rich shales during heating: an overview**

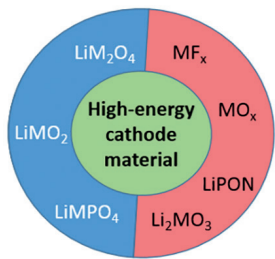
**Tagir I. Karamov**

Alterations of organic-rich shales during heating:

- Fracturing along lamination. First fractures appear at  $\approx 200\text{ }^\circ\text{C}$
- OM decomposition (destruction). OM decomposition starts at  $\approx 200\text{ }^\circ\text{C}$
- Significant weight loss due to OM destruction
- Increasing of porosity and permeability
- Decreasing of thermal conductivity

**45**

**SMALL REVIEW:**



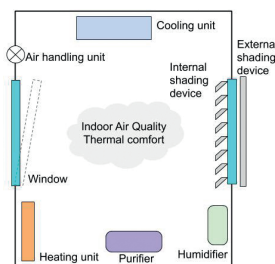
**Overview of protective coatings for cathode materials for li-ion batteries**

**A. Shevtsov**

- Core-shells can be synthesized using sol-gel route, chemical vapor deposition, atomic layer deposition, mechanical activation, solvothermal method, hydroxide and carbonate coprecipitation
- Coatings for positive electrodes are structurally diverse, they include: oxides, fluorides, electrolytes and cathode materials
- The structure of a protective layer may be a core-shell, ultrathin layer, double layer or a concentration gradient

**53**

**SMALL REVIEW:**



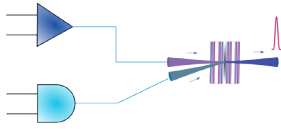
**Concepts of commercial and patented smart indoor microclimate contro; solutions: a review**

**Arseniy A. Sleptsov**

- A gap between the theory and application of control techniques of facility providing an indoor air quality and thermal comfort of a built environment was identified
- Technological concepts of both the commercial and patented solutions were accessed and summarized
- Barriers to reduce to practice of control strategies presented in scientific papers were discussed

**64**

## FOCUS:

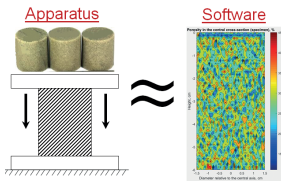
Towards organic polariton devices

**Anton V. Baranikov, Anton V. Zasedatelev, Pavlos G. Lagoudakis**

- Polaritons are hot topic from both fundamental and practical point of view
- Polariton optical devices are not a dream, they were already shown
- Organic polaritonics is coming to create room temperature devices

**73**

## FOCUS:

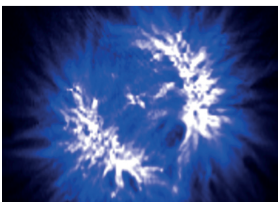
Axial splitting in uniaxial compressive testing: a focus

**Mikhail Y. Nikolaev**

- Uniaxial compression test (UCT) is the basic geomechanical investigation during which rock core samples experience cracking
- Axial cracks appear as a result of a complicated physical process after the appearance of radial cracks
- Numerical simulation of UCT is possible using the Matlab soft-ware for the cross-section of a cylindrical rock core sample
- Numerical simulation of UCT allows performing cross-validation of laboratory data and simulation results and preventing samples and expensive geomechanical equipment from unnecessary use

**78**

## FOCUS:

Polariton lasing in organic-based microcavities

**T. F. Yagafarov, D. A. Sannikov, P. G. Lagoudakis**

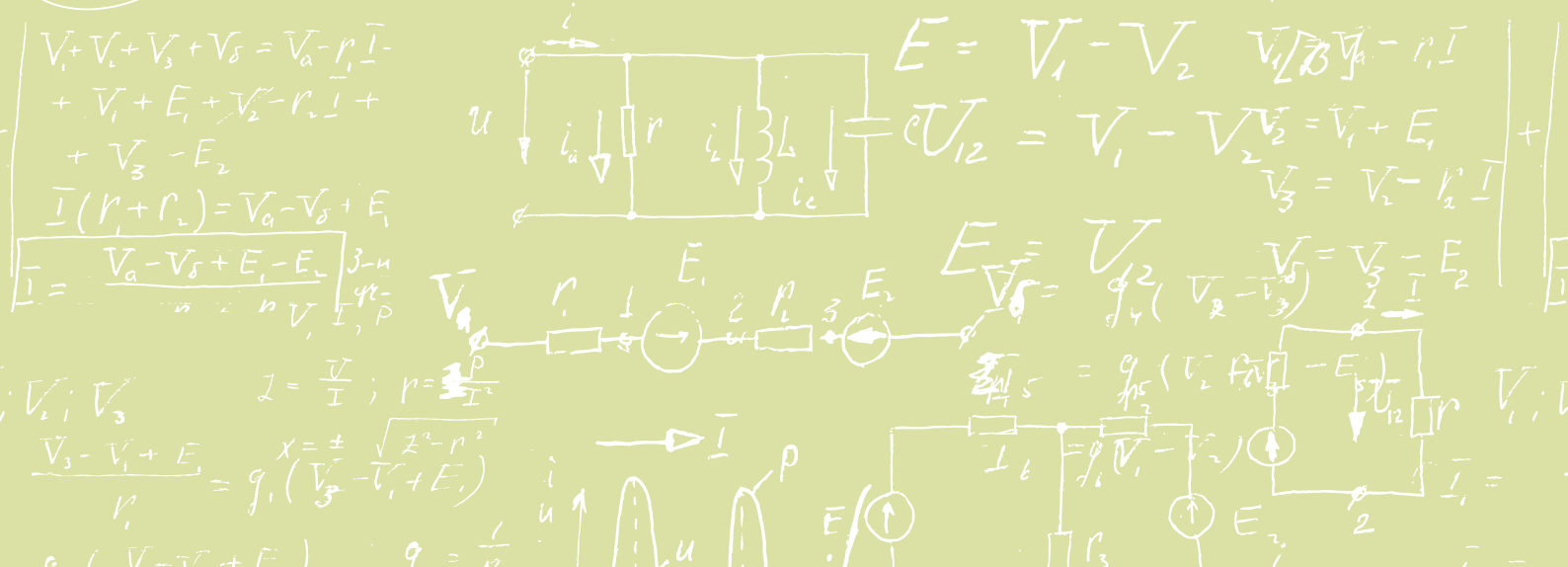
- Polariton lasers based on organic-filled microcavities can operate at room temperatures
- High quantum yield and cheap fabrication techniques of organic polariton lasers makes them promising candidates in microdisplays and retinal laser projectors for deep color augmented reality applications
- Tunable polariton laser realized on organic-filled microcavity

**89**





**Research Articles:**



# Design of an Optimized Nanopositioning Stage for High-Speed Atomic Force Microscope

Maria Zhilyaeva\*, Fardad Azarmi, Iman Soltani Bozchalooi, Kamal Youcef-Toumi

## Abstract

Atomic Force Microscope provides a nano-scale resolution image of surface topography by scanning a small cantilever tip over the sample. However, Atomic Force Microscope speed is limited by hysteresis, creep, thermal drift, mechanical resonance, and serial-point-collection bases of operation. Through optimized mechanical design and control system, the operating speed can be significantly increased. In this work, a multi-actuated nanopositioning scanner stage is developed. It is composed of flexure-guided frames, made from 7075 aluminum alloy, and ten nanopositioners with different bandwidth and range characteristics, which are capable of operating at high speed and over large lateral and out-of-plane scan ranges. Symmetric structure and heat sink design reduce the negative consequence of thermal drift. This study contributes to the design of a novel Atomic Force Microscope scanner. The frequency and static finite element analysis simulations show the high-speed capability of the nanopositioning stage and its ability to operate short-range scanner with 6.8 kHz bandwidth in 5.4×5.0 μm lateral scan range and with 2.4 kHz bandwidth in 13.5 μm out-of-plane scan range. Modular design provides for simple replacement and setting up of new components for future improved instrumental designs.

## Index Terms

High-speed atomic force microscope; nanopositioner; nanopositioning stage.

\* **M. A. Zhilyaeva** (Goncharova) is with the Center for Photonics and Quantum Materials, Skolkovo Institute of Science and Technology, Skolkovo Innovation Center, Building 3, Moscow, 121205, Russia (e-mail: Maria.Goncharova@skoltech.ru).

**Fardad Azarmi** was with Skolkovo Institute of Science and Technology, Center for Design, Manufacturing and Materials. He is now with the Department of Mechanical Engineering, North Dakota State University, Fargo, ND 58108, USA (e-mail: fardad.azarmi@ndsu.edu).

**Iman Soltani Bozchalooi** is with Department of Mechanical Engineering Massachusetts Institute of Technology, 77 Massachusetts Avenue, Cambridge, Massachusetts 02139, USA (e-mail: isoltani@mit.edu).

**Kamal Youcef-Toumi** is with Department of Mechanical Engineering Massachusetts Institute of Technology, 77 Massachusetts Avenue, Cambridge, Massachusetts 02139, USA (e-mail: youcef@mit.edu).

---

## I NOMENCLATURE

$k$	stiffness of the structure (N / $\mu\text{m}$ )
$F$	force (N)
$\Delta L$	displacement ( $\mu\text{m}$ )
$\omega_r$	resonance frequency (Hz)
$\zeta$	damping ratio (-)
$G(s)$	transfer function

---

## II INTRODUCTION

**A**TOMIC force microscopy (AFM) is a nanometer scale technology for three-dimensional (3D) and high-resolution studies of surface details [1], [2]. Using this technique, we can obtain images with atomic resolution and Ångström scale resolution for the data on the surface landscape. The instrument may be used for different materials such as hard and soft synthetics and even for biological structures like cells and biomolecules. It does not have any restrictions related to the opaqueness or conductivity [3]. Regardless of the configuration chosen for developing AFM, there is a technical challenge with developing high-speed scanners. This is related to the fact that traditional scanners have low first resonant frequencies, which mean they go into resonance faster. Scientists like Ando et al. have made progress in building high-speed scanners by stacking up piezoelectric materials to achieve higher frequencies of up to 240 kHz [4]-[6], but small travel range. Using fast scanners, high scan rates of up to 80 ms per frame can be achieved in the intermittent contact mode in liquid [5]. Even faster rates of 1 ms can be attained in contact mode, although without full feedback control [7]. The biggest challenge with making high-speed scanner is creating a z-axis positioner that is fast enough to respond to sharp changes in sample height due to fast x-y scanning over [8]. Unfortunately, hysteresis, creep, thermal drift, mechanical resonance, and serial-point-collection bases of operation of the instrument limit its speed. Through optimized mechanical design, the operating speed can be significantly increased. This work presents the design of an optimized nanopositioning stage for a novel AFM.

---

## III DESIGN PROCESS

The design of Nanopositioner is always iterative (design – Finite Element Analysis (FEA) – design) [9]. To achieve higher bandwidth and better resolution, piezo actuators have to be small. The tradeoff is a balance between achieving higher mechanical bandwidth and the travel range that needs to be accomplished. To increase the travel range, flexure hinges are usually used as mechanical amplifiers.

## A. Requirements

The previous Scanner [7], designed at MIT, faced a problem of self-heating of piezo actuators and, as a result, thermal drift. One of the goals of the new design is to prevent this phenomenon. To achieve competitive results for High-Speed AFM at MIT Mechatronics Laboratory [10] specific parameters are required. As a result, the following technical requirements were set up:

- X,Y bandwidth > 5 kHz
- X,Y range > 5 micron \* 5 micron
- Z-axis bandwidth > 1.5 kHz
- Z-axis range > 13 micron

It was also decided to consider interchangeable design.

## B. Challenges of nanopositioning stages

Nanopositioning systems, based on piezo actuators, face the following challenges. Due to their effectively infinite resolution, piezoelectric actuators are universally employed in nanopositioning applications. However, the positioning accuracy of piezoelectric actuators is limited by hysteresis over large displacements, creep, and thermal drift which is present at low-frequencies. Another major problem with nanopositioning systems is the presence of lightly damped mechanical resonances. These dynamics can result in large oscillations, particularly when step-changes or high-frequency inputs are involved. The impact of these detrimental phenomena is discussed below [9].

### HYSTERESIS

When employed in an actuating role, piezoelectric transducers display a significant hysteresis in the transfer function of the applied voltage to the resulting strain or displacement [11]. In dynamic applications, hysteresis is considered the foremost limitation of performance. It leads to poor positioning accuracy, poor repeatability, and mixing of harmonic content into the displacement response [9].

### CREEP

When a piezoelectric transducer is commanded by a step change in voltage, the response speed is limited only by the mechanical resonance of the host structure or transducer. Creep is the phenomenon where actuator deflection slowly “creeps” upward after an increase in applied voltage. The time constant is typically a few minutes. Creep severely degrades the low-frequency and static positioning ability of piezoelectric actuators [9].

### THERMAL DRIFT

Even though piezoelectric materials are first of all electromechanical, temperature greatly affects these electromechanical properties. Temperature changes can cause

thermal drift which affects the positioning of the piezoelectric actuator. As an example, a 50° C temperature could result in a rise in displacement sensitivity (in this case it causes a 20% rise). The result of this is a drift of about 0.4% which is larger than the mechanical drift [9]. Using piezoelectric transducers means taking into consideration the thermal drift that may occur as a result of temperature rise.

#### MECHANICAL RESONANCE

A nanopositioning platform has several moving and interacting parts. The movements of these parts mean that mechanical resonances occur as the platform mass interacts with the actuators and support flexures. As with other applications, the lowest resonance frequency is usually the determinant of the dynamics, which can be estimated using a unity gain second-order low pass system as follows:

$$G(s) = \frac{\omega_r^2}{s + 2\omega_r\zeta s + \omega_r^2} \quad (1)$$

where  $\omega_r$  and  $\zeta$  are the resonance frequency and damping ratio.

In order to prevent the excitation of the mechanical resonance, the frequency of the driving signals is typically constrained to about 1-10% of the lowest resonance frequency. Another way to mitigate mechanical resonance, especially in high-speed AFM, is to operate the nanopositioner in an open loop and shape the driving signals to reduce harmonic content [12]-[15].

Possibly the most effective way to improve the transient response of a nanopositioner is by actively damping the first resonance mode. Doing this can greatly reduce the settling time by more than 90% and thus improve the scan speed [9].

#### C. Flexure hinges

One hindrance with using piezo actuators is the limitation of the motion range. To put this in perspective, consider that a 10-mm long piezo-stack actuator at a drive voltage of 200 V will extend only 11  $\mu\text{m}$  in unconstrained conditions. To achieve bigger displacements, actuators are made longer or mechanical amplifiers are deployed. However, using longer actuators or mechanical amplifiers reduces the mechanical bandwidth because of the effective stiffness of the design. This is due to the fact that the actuator's maximum stroke is inversely proportional to the first resonance frequency.

Several flexure hinge design concepts developed in this study are shown in Fig. 1.

The flexure hinge is a thin elastic component connecting two rigid bodies and providing a limited relative bending or flexing motion. The flexure hinges help guide the motion of a mass sample (red in the figure) along with a straight path [9]. A flexure hinge is different from classical mechanical joints because the center of rotation of flexure hinge is non collocated, whereas for mechanical joints (rotational bearing) it is collocated. Moreover, usual limitations of classical joints such as friction, hysteresis do not apply to flexure hinges.

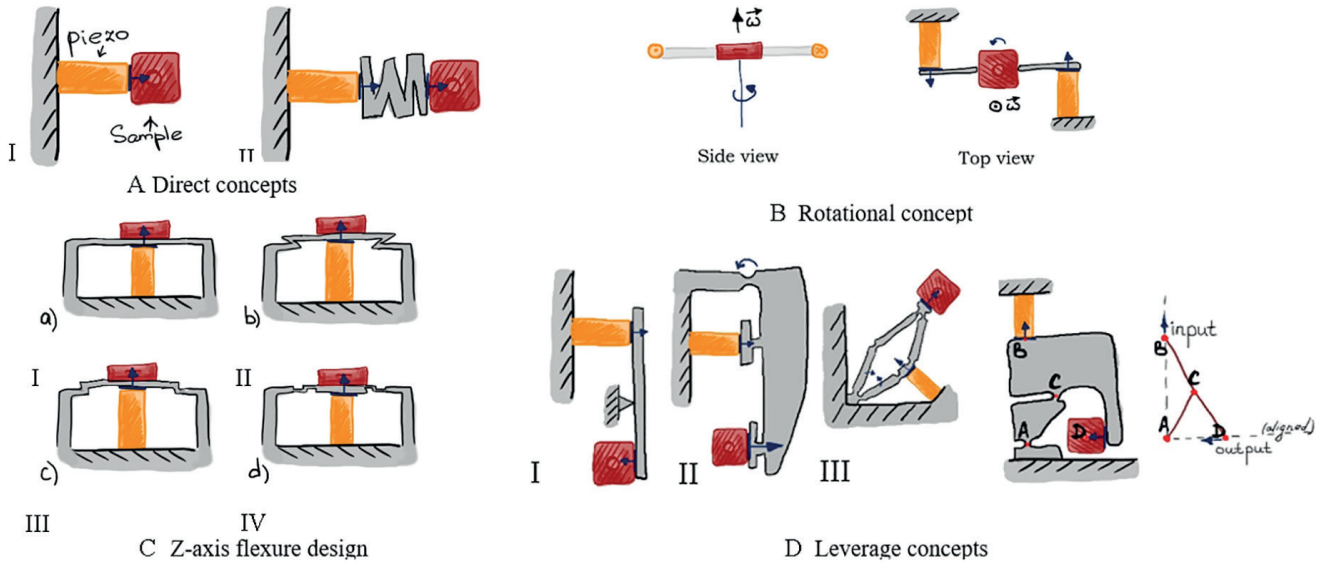


Fig. 1. Flexure hinge design concepts.

For the purpose of this project, the direct concept of flexure connection was chosen for its simplicity and cost-effectiveness.

#### D. Material selection

Selecting the materials for the different components of a nanopositioning stage is critical to the overall performance of the stage.

Some of the materials commonly used for the frame and flexure hinges are described in Table I.

TABLE I. Widely used materials for nanopositioning systems [4]

Material	Density (kg/m <sup>3</sup> )	Young's Modulus (GPa)	Thermal Conductivity (W/m*°C)	Coefficient of Thermal Expansion (10 <sup>-6</sup> /°C)
6061 Aluminum	2710	70	167	23.6
7075 Aluminum	2800	72	130	23.6
Stainless steel	7920	190	16.3	17.3
Titanium	4730	115	15.6	9.5
Invar (Invar 36)	8130	144	13.8	1.6
Super Invar	8137	144	10.5	0.3

Some of the critical criteria for selecting the materials for the frame and flexure hinges are machinabilities and the density-to-stiffness ratio of the material. Other important factors include favorable (low) thermal expansion coefficient and anti-corrosion properties.

For other components like the sample platform, aluminum is commonly used because of its high stiffness-to-density ratio. For the base, stainless steel is the material choice due to its anti-corrosion properties and high elastic modulus.

In order to increase the dynamic performance of the system, materials with high Young's modulus ( $E$ ) to low density ( $\rho$ ) ratio are used [16]. Materials with such properties are usually lightweight and stiff, which increases the bandwidth of the platform.

### E. Final design

During the development process, several iterations of different designs were created. This section presents the results of the final design choice and specifications of the AFM Nanopositioning Stage created.

An optimized serial-kinematic three axis nanopositioning stage was developed. Its final design is shown in Fig. 2.

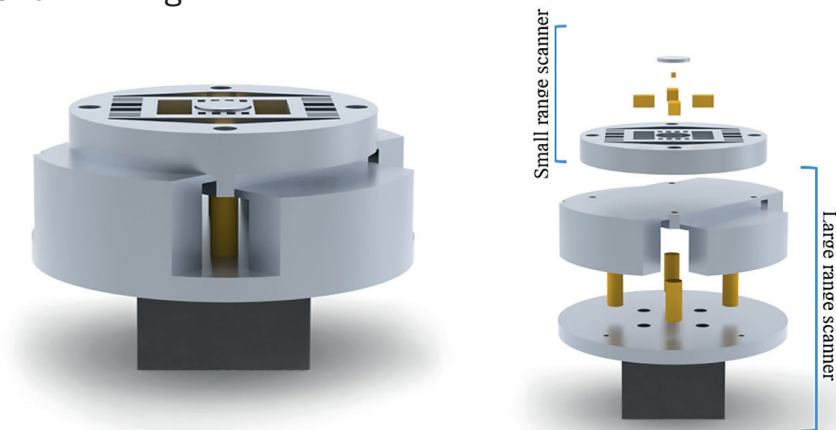


Fig. 2. Final design. Assembled and disassembled view.

The design of a Scanner for the High-Speed AFM is based on the multi-actuating concept.

There is a hybrid system of two levels (see exploded view in Fig. 2) of independent scanners (nanopositioners): small range ( $5 \times 5,4 \times 1,7 \mu\text{m}$ ) and large range ( $120 \times 120 \times 13 \mu\text{m}$ ). Both levels are made from 7075 aluminum alloy, chosen before. The modular design allows ease of interchangeability of the Small Range Scanner, and future designs set up.

#### LARGE RANGE SCANNER

Fig. 3 shows the Large Range Scanner design developed as part of this project. It consists of

- XY Positioner, which is commercially available (P-611. XY PICMA® Nanopositioner [17]);

- Stage, 6mm height, for mounting the construction to XY Positioner;
- Set of 4 Piezoelectric actuators P-007.10 PICMA® Piezo Actuator [17];
- Z-positioner aligns out-of-plane motion (Fig. 4). A precise cross-bladed translator actuation method for Z-axis is used in the design. According to a literature review, there are no nanopositioners using this concept. This mechanism is suited for precision applications where only one translational degree of freedom (DOF) is required. All other motions are constrained. Rounded walls are fixed. The central stage (6mm thick) is free to translate in the vertical direction glued by 2mm thick horizontal flexures. The translational DOF is orthogonal to the plane of the ground [18].

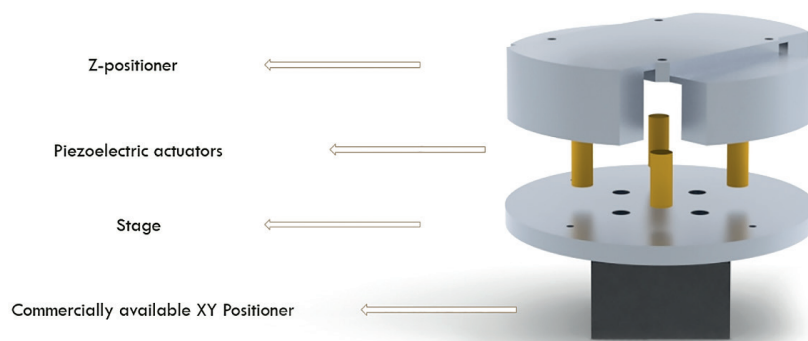


Fig. 3. Large range scanner.

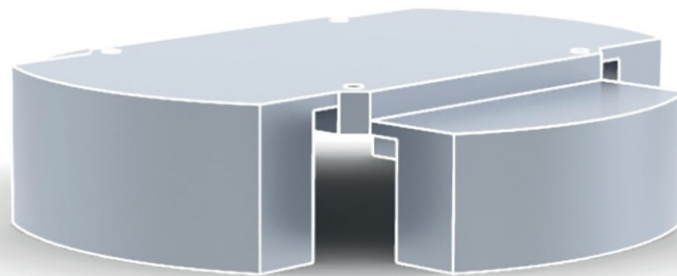


Fig. 4. Z positioner. Cross-bladed translator.

#### SMALL RANGE SCANNER

The Small Range Scanner is mounted on the Large Range Scanner. Its goal is to fast and precisely move central (round) stage with a sample. Serial-kinematic configuration is implemented as a positioning concept. Fig. 5 illustrates Small Range Scanner composition.

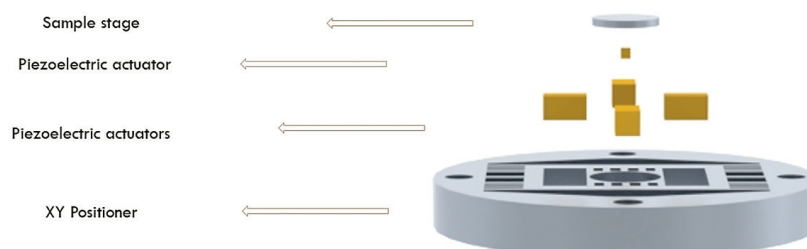


Fig. 5. Small range scanner.



The small range scanner consists of the following:

- XY Positioner. For lateral positioning, there is a double-frame system (100 mm thick) (Fig. 6). Each frame moves the sample in one direction (X/Y). Push-pull preload and displacement principles are the same for each flexure diaphragm. Optimized cavities near piezo actuators are designed for a heat sink (Fig. 6). Symmetrical structure and its composition compensate for piezo thermal expansion and its negative effects on Nanopositioner performance.
- Piezoelectric actuators (P-885.11 PICMA® Stack Actuator [17]) are set up into XY positioner to provide lateral displacement for the sample.
- Piezoelectric actuator (PLO22.30 PICMA® Chip Actuator [17]) moves the sample in Z-direction. Fig. 6 shows a sliced view of a Small Range Scanner, and how the compact actuator is attached to the sample stage and the XY Positioner.
- Sample stage (1,5 mm thick) holds the sample.

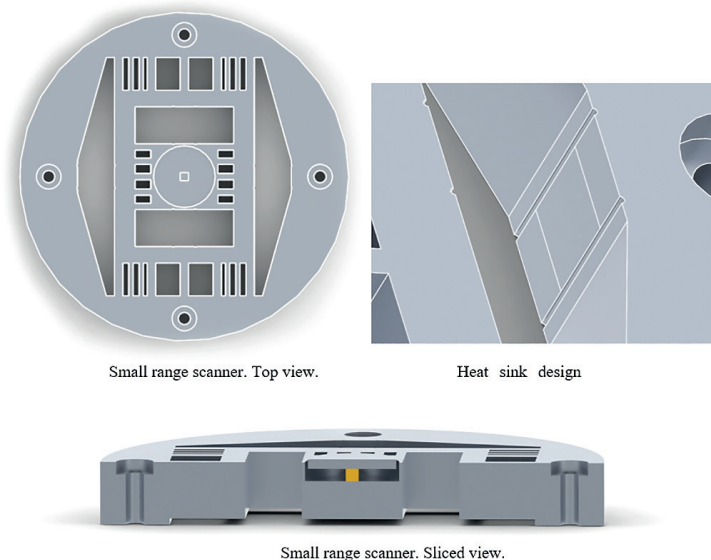


Fig. 6. Small range scanner design.

## F. Piezo actuator selection

FEA simulation was used to choose the coefficient of stiffness and displacements, the optimal piezo stack actuators, and their parameters (blocking force, area, and maximum displacement). While selecting the optimal actuators, the following technical requirements were considered:

- X,Y bandwidth > 5 kHz
- X,Y range > 5 micron \* 5 micron
- Z-axis bandwidth > 1.5 kHz
- Z-axis range > 13 micron

The algorithm for choosing the actuator's parameters (on the example of large range Z-displacement) is presented further.

Consider P-007.10 PICA Stack Piezo Actuators for 15  $\mu\text{m}$  range.

$$\text{Blocking force of 1 piezo} = 850 \text{ N} \quad (2)$$

$$850 \text{ N} \cdot \frac{3}{2} = 1275 \text{ N}. \quad (3)$$

According to the FEA, the total maximum scanner X-displacement for P-007.10 is 0,060 mm. According to Hook's law, the stiffness of the structure  $k_{\text{scanner}}$  is:

$$k_{\text{scanner}} = \frac{F_{\text{blocking force}/2}}{\text{Displacement}} = \frac{1275 \text{ N}}{60\mu\text{m}} \approx 21 \text{ N}/\mu\text{m} \quad (4)$$

$$k_{\text{piezo}} = 3 \cdot k_{\text{single actuator}} = 3 \cdot 59 \text{ N}/\mu\text{m} = 177 \text{ N}/\mu\text{m} \quad (5)$$

where  $k_{\text{single actuator}}$  is a stiffness of each actuator (from datasheet). Then,

$$\begin{aligned} \Delta L_{\text{system}} &= \Delta L_{\text{piezo}} \cdot \left( \frac{k_{\text{piezo}}}{k_{\text{piezo}} + k_{\text{scanner}}} \right) \\ &= 15\mu\text{m} \\ &\quad \cdot \left( \frac{177 \text{ N}/\mu\text{m}}{177 \text{ N}/\mu\text{m} + 14.1 \text{ N}/\mu\text{m}} \right) \\ &= 15\mu\text{m} \cdot 0.93 = 13,95\mu\text{m} \\ &\approx 14\mu\text{m} \end{aligned}$$

where  $\Delta L_{\text{system}}$  – resulting displacement.

As a result, after numerous calculations with different parameters of commercially available piezo stack actuators, the optimal actuators are:

- For Large Range Scanner:
  - XY-positioning: P-611. XY PICMA® Nanopositioner [17];
  - Z-positioning: P-007.10 PICMA® Piezo Actuator [17].
- For Small Range Scanner:
  - XY-positioning: P-885.11 PICMA® Stack Actuator [17];
  - Z-positioning: PL022.30 PICMA® Chip Actuator [17].

## G. Results validation

The greatest challenge in the design process of a Nanopositioning Stage is to find a trade-off between bandwidth and displacement. At resonance frequency, any structure

tends to vibrate. Each natural frequency has its shape, which is called the mode shape. At resonance frequency, the structure is subject to large displacements and stresses.

The following considerations guided the FEA:

- Direct Sparse Solver was used;
- Boundary conditions:
  - Piezo and metal are bonded,
  - Fixed geometry for screw holes.
- Meshed model and meshing parameters are shown in Fig. 7.

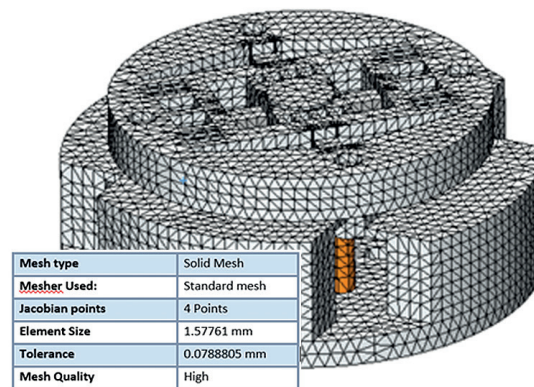


Fig. 7. Meshed model and the parameter.

- Frequency FEA (results are shown in Fig. 8).
- Static FEA was simulated with half of the blocking force applied on the mounting area between metal and actuator.

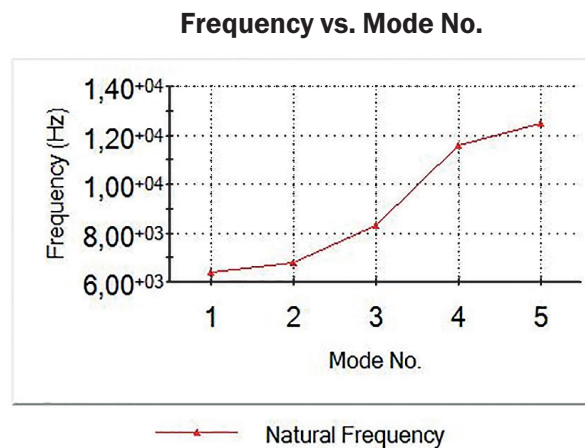


Fig. 8. Frequency modes of the structure.

As a result of the FEA simulation, the following characteristics of the Nanopositioning Stage were obtained:

- X, Y bandwidth 6.8 kHz
- X, Y range 5.4x5.0  $\mu\text{m}$

- Z-axis bandwidth 2.4 kHz
- Z-axis range 13.5  $\mu\text{m}$ .

## H. Rapid prototyping

During the design process, various 3D models of the Nanopositioning Stage were drawn. In order to check their ergonomics and ease of assembly, the 3D models were printed using UltiMaker 2 [19] 3D printer (PLA filament, and 0,4 mm diameter nozzle). Fig. 9 shows a photograph of printed models, where (1) is the semifinal design, and (2) is the final design. These figures are made on a scale of 1:1. Each of the models could be contained in a volume of 10 x 10 x 4 cm.



Fig. 9. Photograph of printed and assembled prototypes of the Nanopositioner. Left – semi-finalized design; right – the final design of a Nanopositioner.

---

## IV. CONCLUSIONS

The article describes the development of an Optimized Nanopositioning Stage for high-speed Atomic Force Microscope. During the work the optimal actuation method, actuators themselves, material, force transducing concept were chosen. The design provides a serial-kinematic three-axis nanopositioning stage for high-bandwidth applications, including include video-rate Atomic Force Microscopy, while taking into consideration

- Heat sink
- Interchangeability
- Symmetrical structure to compensate for piezo thermal expansion.

All specification requirements were fulfilled/exceeded and validated with Finite Element Analysis. The design offers:

- X, Y bandwidth 6.8 kHz
- X, Y range 5.4x5.0  $\mu\text{m}$
- Z-axis bandwidth 2.4 kHz
- Z-axis range 13.5  $\mu\text{m}$

Presented parameters are validated with Frequency and Static Finite Element Analysis. The prototypes of the designs were 3D printed, assembled, and checked for their ergonomics and ease of assembly. Furthermore, the device can be manufactured using existing technologies. The final Nanopositioner could be implemented in many systems, requiring fast and precise movement.

---

## REFERENCES

- [1] B. D Terris, J. E. Stern, D. Rugar, H. J. Mamin, "Contact electrification using force microscopy," *Phys. Rev. Lett.*, vol. 63, no. 24, pp. 2669–2672, Dec. 1988.
- [2] G. Haugstad, *Atomic Force Microscopy*. New Jersey: JohnWiley & Sons, Inc., 2012.
- [3] T. Ando, T. Uchihashi, N. Kodera, "High-speed AFM and applications to biomolecular systems," *Annu. Rev. Biophys.*, vol. 42, pp. 393–414, 2013.
- [4] M. Yokokawa, S. H. Yoshimura, Y. Naito, T. Ando, A. Yagi, N. Sakai, K. Takeyasu, "Fast-scanning atomic force microscopy reveals the molecular mechanism of DNA cleavage by Apal endonuclease," *IEE Proc. Nanobiotechnol.*, vol. 153, no. 4, pp. 60–66, Aug. 2006.
- [5] T. Ando, N. Kodera, Y. Naito, T. Kinoshita, K. Furuta, Y. Y. Toyoshima, "A High-speed Atomic Force Microscope for Studying Biological Macromolecules in Action," *ChemPhysChem*, vol. 4, no. 11, pp. 1196–1202, Nov. 2003.
- [6] L. M. Picco, L. Bozec, A. Ulcinas, D. J. Engledew, M. Antognozzi, M. A. Horton, M. J. Miles, "Breaking the speed limit with atomic force microscopy," *Nanotechnology*, vol. 18, no. 4, pp. 044030, Dec. 2007.
- [7] P. Eaton, P. West, *Atomic force microscopy*. New York: Oxford University Press Inc., 2010.
- [8] A. J. Fleming, K. K. Leang, *Design, Modeling and Control of Nanopositioning Systems*. New York: Springer, 2014.
- [9] I. Soltani Bozchalooi, A. Careaga Houck, J. M. AlGhamdi, K. Youcef-Toumi, "Design and control of multi-actuated atomic force microscope for large-range and high-speed imaging," *Ultramicroscopy*, vol. 160, pp. 213–224, Jan. 2016.
- [10] H. J. M. T. A. Adriaens, W. L. de Koning, R. Banning, "Modeling piezoelectric actuators," *IEEE/ASME Trans. Mechatronics*, vol. 5, no. 4, pp. 331–341, Dec. 2000.
- [11] G. Schitter, K. J. Åström, B. E. DeMartini, P. J. Thurner, K. L. Turner, P. K. Hansma, "Design and modeling of a high-speed AFM-scanner," *IEEE Trans. Control Syst. Technol.*, vol. 15, no. 5, pp. 906–915, Sept. 2007.
- [12] T. Ando, T. Uchihashi, N. Kodera, A. Miyagi, R. Nakakita, H. Yamashita, M. Sakashita, "High-speed atomic force microscopy for capturing dynamic behavior of protein molecules at work," *Jpn. J. Appl. Phys.*, vol. 45, no. 3B, pp. 1897–1903, 2006.
- [13] A. D. L. Humphris, M. J. Miles, J. K. Hobbs, "A mechanical microscope: High-speed atomic force microscopy," *Appl. Phys. Lett.*, vol. 86, no. 3, pp. 034106, Jan. 2005.
- [14] M. J. Rost, L. Crama, P. Schakel, E. van Tol, G. B. E. M. van Velzen-Williams, C. F. Overgaw, H. ter Horst, H. Dekker, B. Okhuijsen, M. Seynen, A. Vijftigschild, P. Han, A. J. Katan, K. Schoots, R. Schumm, W. van Loo, T. H. Oosterkamp, J. W. M. Frenken, "Scanning probe microscopes go video rate and beyond," *Rev. Sci. Instrum.*, vol. 76, no. 5, pp. 053710, May 2005.
- [15] P. Wang, Z. Zhang, P. Yan, "Design of a novel parallel flexure-based large stroke XY nano-positioner," in *Proc. 2015 27th Chinese Control Decis. Conf. CCDC 2015*, pp. 4264–4269, 2015.
- [16] Physik Instrumente (PI) GmbH & Co. KG, "PI – Solution for precision motion and positioning." [Online]. Available: <https://www.physikinstrumente.com/en/>.
- [17] L. L. Howell, S. P. Magleby, B. M. Olsen, *Handbook of Compliant Mechanisms*. John Wiley and Sons, 2013.
- [18] Ultimaker, "Ultimaker 3D Printing Products." [Online]. Available: <https://ultimaker.com/en/products>.

# Energy Efficiency Analysis of Vanadium Redox Flow Battery Cell

M. Pugach\*, A. Bischi

## Abstract

A simulation-based Vanadium Redox Flow Batteries (VRFB) efficiency estimation approach is proposed followed by a detailed study of a VRFB cell energy performance in a wide range of current densities (40-100 mA cm<sup>-2</sup>). Energy losses are evaluated for charge and discharge processes individually; energy efficiency is determined by a comparison with equilibrium potential curve that corresponds to the voltage of an ideal cell (without losses). The results show that charge and discharge energy efficiencies decline linearly with the increase of current density having the same slope. The charge efficiency lies in the range of 95-98%, while the discharge efficiency is a bit smaller and lies in the range of 93-96%. Energy losses in charge process are mainly determined by ohmic overvoltages, while in discharge they are additionally affected by concentration overvoltages and crossover. The presented results can provide the guidelines for a potential improvement of VRFB systems and the development of more efficient cells with high power density in economically viable VRFB systems for practical applications.

## Index Terms

Vanadium Redox Flow Batteries; energy efficiency; internal losses; capacity losses; ohmic overvoltages; concentration overvoltages; ions crossover.

## I NOMENCLATURE

$A$	battery capacity (A h)
$c$	molar concentration (mol m <sup>-3</sup> )
$c_0$	initial molar concentration of vanadium in the electrolyte (mol m <sup>-3</sup> )

This work was supported by the Next Generation Program: Skoltech – MIT Joint Projects.

\* **M. Pugach** is with the Center of Energy Science and Technology, Skolkovo Institute of Science and Technology, Skolkovo Innovation Center, Building 3, Moscow, 121205, Russia (e-mail: mikhail.pugach@skolkovotech.ru).

**A. Bischi** is with the Center of Energy Science and Technology, Skolkovo Institute of Science and Technology, Skolkovo Innovation Center, Building 3, Moscow, 121205, Russia (e-mail: a.bischi@skoltech.ru).

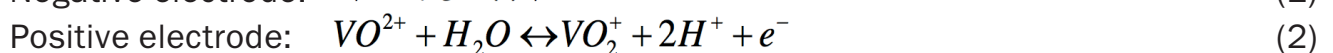
<i>conc</i>	concentration losses
<i>cros</i>	crossover losses
<i>I</i>	current (A)
<i>ohm</i>	ohmic losses
<i>t</i>	time (s)
$U_{bat}$	battery voltage (V)
$U_{eq}$	cell equilibrium potential (V)
$\eta_{EE}$	energy efficiency
<i>ch</i>	charge
<i>dis</i>	discharge
<i>id</i>	ideal
<i>init</i>	initial
<i>SOC</i>	state of charge

---

## II INTRODUCTION

**V**ANADIUM Redox Flow Battery (VRFB) is one of the most promising solutions for large scale stationary energy storage systems [1]. VRFB stores energy in the electrolytes based on the vanadium salts stored in two external separated tanks and pumped through cells where electrochemical conversion is taking place. Such technological concept allows splitting the power and energy ratings and scaling them independently. Moreover, VRFB has very long life time (20+ years), good cycling operation (10000+ cycles) and very low self-discharge [2]-[4]. One of the main obstacles for commercialization of this technology is the high cost of the components [5]. Therefore, development of more efficient cells with higher power density is one of the possible ways to reduce the cost of the VRFB technology [6]. In order to do that, the cells should operate under higher current densities and electrolyte flow rates while avoiding the increase of internal losses, which would worsen the battery performance.

VRFB works with V(II)/V(III) and V(IV)/V(V) redox couples dissolved in sulphuric acid and used as negative and positive electrolyte, respectively. The electrolytes are stored in the separate tanks (2) and pumped through half-cells separated by a polymeric membrane (1) (Fig. 1). The electrochemical reactions in the negative and positive half-cells are described by the following equations:



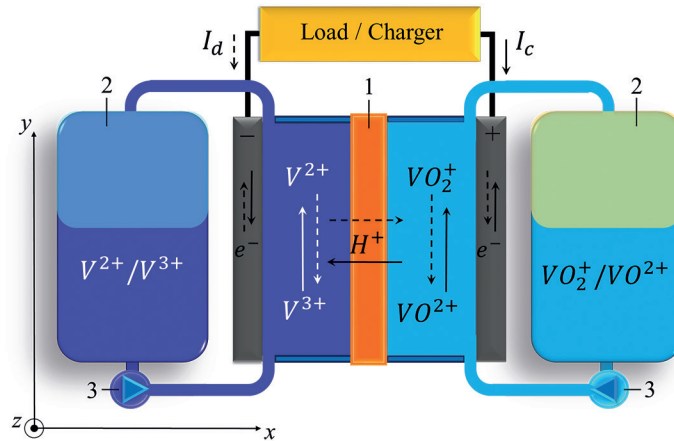


Fig. 1. Working scheme of VRFB system [7].

The internal losses in the cell are presented by activation overvoltages (due to activation energy of electrochemical reactions), ohmic overvoltages (due to electric resistance of cells' components), concentration overvoltages (due to mass transport limitations on the surface of electrode) and crossover (transfer of vanadium ions across the membrane) [8].

Activation and ohmic losses affect the battery voltage during the whole operation process while the concentration losses become pronounced at the end of the process when the concentration of reactants becomes limited [9]. In addition, the crossover results in the side reactions [10] that reduces available battery capacity [6], [11]-[13]. Understanding of these phenomena and their contribution to the total energy and capacity losses is very important for the development of efficient VRFB facilities. Nevertheless, to the best of the author's knowledge, this issue has not been considerably investigated to date. Many works devoted to this topic [14]-[18] present only the round trip energy efficiency indicators calculated for the whole charge-discharge cycle. While these indicators can provide information about the losses observed in the cycling operation, they do not allow estimation of the energy performance of VRFB in comparison to the ideal case (without losses). However, this information can be valuable for the improvement of the cell design determining optimal operating constraints. In addition, the round-trip indicators do not reflect the degradation of the battery performance due to deterioration of transport properties of membrane and electrodes during long operation of the battery. Accordingly, energy losses need to be analyzed separately for charge and discharge process. Such approach was mentioned by Zhang et al. [20], where they presented the charge and discharge energy efficiency for a VRFB cell stack as a function of its power. Hence, these data are highly connected to the configuration of the considered stack. Moreover, no calculation method of the mentioned efficiencies was presented, which makes these data rather difficult to implement in other VRFB systems.

In this paper, a simulation-based VRFB efficiency estimation approach is proposed, and a detailed study for energy performance of a VRFB cell is performed. Energy losses are estimated in charging and discharging operation individually with application of energy efficiency, which was determined by comparison with the voltage of ideal cell (without losses) that corresponded to the equilibrium potential. The results of this study can facilitate determination of optimal operating conditions that could maximize energy efficiency of VRFB systems while ensuring their long-term operation.



---

### III MATHEMATICAL MODEL

The study is based on the 0-D dynamic model [7]. The proposed mathematical model determines the battery voltage ( $U_{bat}(t)$ ) depending on the operating conditions: electric current ( $I$ ), electrolyte flow rate ( $Q$ ) and ambient temperature ( $T$ ).

The model was derived basing on the following assumptions:

1. Electrodes and electrolytes are homogeneous and isotropic;
2. Cell resistance is constant;
3. Battery temperature is constant;
4. Electrolytes in the cell and the tanks are continually mixed (stirred reactors);
5. Crossover flux is determined by diffusion, migration and conversation;
6. There are no reactions in the membrane.

#### A. Simulation details

The simulation study was carried out for a single cell battery stack with flow-by configuration and membrane area of 5 cm<sup>2</sup>. The half-cells were separated by the Nafion 115 membrane. The tanks contained 20 ml of electrolyte (each) comprising 1 M vanadium and 2.5 M of sulfuric acid. Cell resistance is assumed to be 0.12 Ω. The battery operated between 5 and 95% of State of Charge (SOC) at constant flow rate 0.86 mL s<sup>-1</sup>, fixed current density, room temperature of 25° C and voltage limits between 0.8 V and 1.6 V. Detailed simulation parameters are described in [7]. Calculations were made for a set of current densities: 40, 60, 80, 100 mA cm<sup>-2</sup>.

#### B. Initial conditions

The initial values (at the moment  $t = 0$ ) of vanadium ions concentrations in the tank and in the half-cell were obtained from initial value of battery State of Charge ( $SOC_{init}$ ) [20]:

$$\begin{cases} c_2(0) = c_0 SOC_{init} \\ c_3(0) = c_0 (1 - SOC_{init}) \\ c_4(0) = c_0 (1 - SOC_{init}) \\ c_5(0) = c_0 SOC_{init} \end{cases} \quad (3)$$

---

### IV PERFORMANCE INDICATORS

The impact of internal losses on the battery voltage in charging and discharging operation is presented on the Fig. 2, where green area presents the stored energy in charge and used in discharge and the grey area presents the energy losses in the process.

The energy performances of a cell can be evaluated by application of the energy charge and discharge efficiencies, which can be calculated with the following formulas (4) and (5). All indicators were compared in respect to the Nernst potential curve without crossover ( $U_{eq,id}$ ), which represents the voltage of the ideal cell operating without any losses.

The charge efficiency was derived as the ratio of energy saved in the process over the energy spent for battery charge (Fig. 2a):

$$\eta_{EE,ch} = \frac{\int_0^{A_{ch}} IU_{eq,id} dt}{\int_0^{A_{ch}} IU_{bat,ch} dt} \quad (4)$$

The discharge efficiency was derived as the ratio of energy used in the process over the energy that could be obtained from the ideal cell (Fig. 2b):

$$\eta_{EE,dis} = \frac{\int_0^{A_{dis}} IU_{bat,dis} dt}{\int_0^{A_{dis}} IU_{eq,id} dt} \quad (5)$$

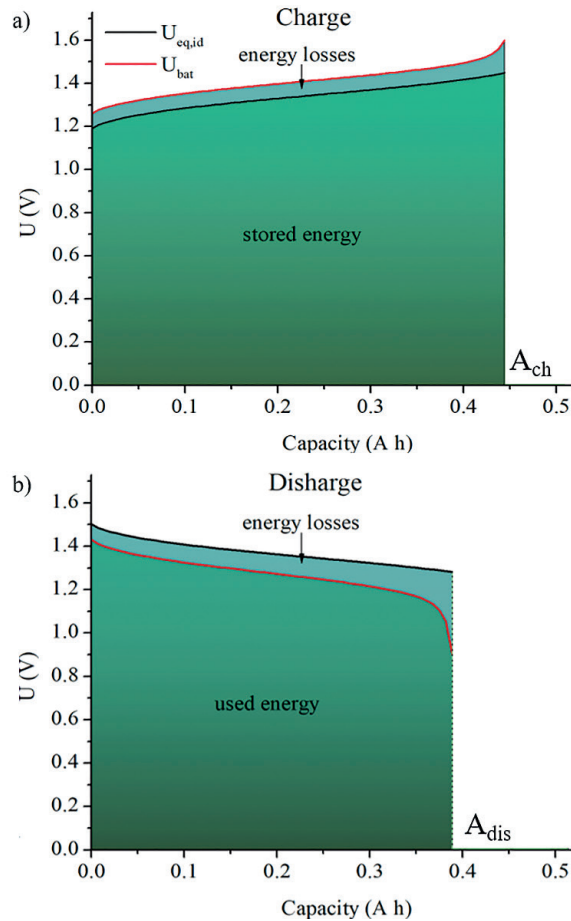


Fig. 2. Energy losses in (a) charge processes; (b) discharge processes.

## V RESULTS AND DISCUSSION

First, the energy losses in the charge process were analyzed. The charge energy efficiency was calculated in accordance with (4). As it can be seen (Fig. 3), the energy efficiency shows the downward trend with increase of current density, however the cell demonstrates rather good energy performance having the energy efficiency higher than 95% (that is in agreement with the value used in **[21]**) in the whole range of considered current densities.

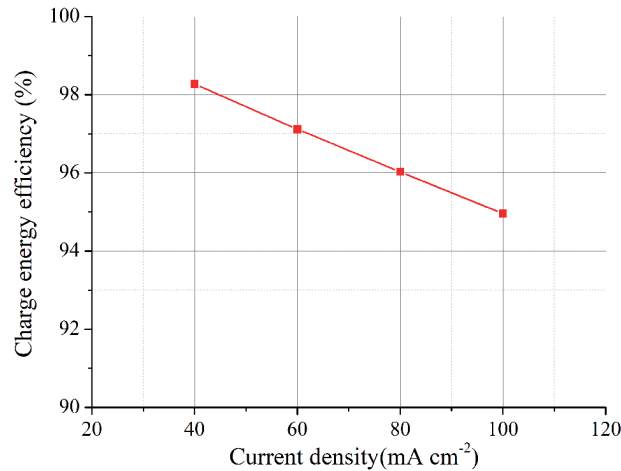


Fig. 3. Charge energy efficiency and share of internal losses.

The shares of ohmic and concentration losses in the observed total energy losses are presented in Fig. 4. The results showed that the major contribution belongs to ohmic losses which present more than 90% at all considered current densities, while the concentration losses are well under the ohmic losses and reach the maximum value of 8% only for the highest current density.

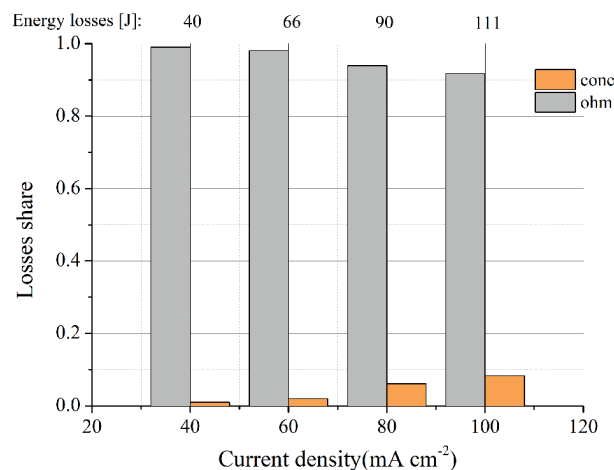


Fig. 4. The shares of internal losses in the energy losses (charge process).

Second, the energy losses in the discharge process were analyzed. The discharge energy efficiency is calculated in accordance with (5). As it can be seen, the efficiency goes down with increase of current density demonstrating the same linear behavior with the same slope as in charge process. Nevertheless, the energy performance in the discharge

process is slightly worse than in charge, and the discharge energy efficiency varies from 96 to 92 % (that is in agreement with [21]) (Fig. 5).

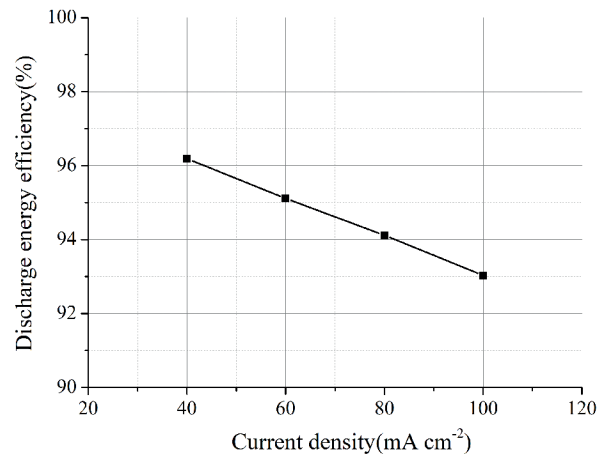


Fig. 5. Discharge energy efficiency.

The share of internal losses in discharge process is shown in Fig. 6. The crossover has a significant contribution to energy losses at low current density leading to the drop of energy efficiency on 40%. However, the share of crossover notably declines with the increase of current density, presenting 20% of losses for high current. This might be due to the fact that crossover is mainly determined by the duration of a charge or a discharge process, which shortens with increase of current density. The share of concentration losses presents approximately 15% of the total losses and remains flat for all considered current densities, which indicates that the concentration losses are directly proportional to the current in the considered region. The major contribution to the energy losses belongs to ohmic losses, which dominate over the other internal losses. The share of ohmic losses presents more than a half of energy losses at low current and goes up with the increase of current density reaching nearly 70% for the high current density.

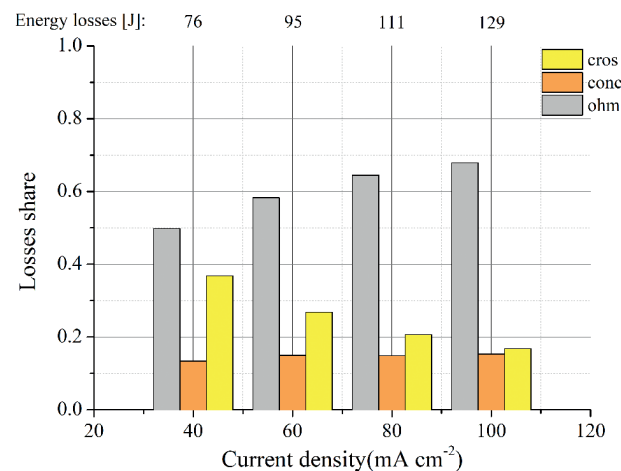


Fig. 6. The share of internal losses in the energy losses (discharge processes).

---

## VI CONCLUSIONS

The influence of internal losses on the cell energy efficiency during charge and discharge processes was analyzed. The results showed that charge and discharge energy efficiencies decline linearly having the same slope with increase of current density. The charge efficiency lies in the range of 95-98%, while discharge efficiency is a bit smaller and lies in the range of 93-96%. These data can be used for the development of advanced optimization techniques that could maximize energy efficiency of the VRFB facilities during long time operation. In addition, the observed values of energy efficiencies can be applied in more accurate techno-economic studies.

Detailed analysis of the contribution of internal losses showed that energy losses in charge processes are mainly caused by ohmic overvoltages, while in discharge they are also notably affected by concentration overvoltages and crossover. It is worth noticing that during discharge the share of concentration losses presents approximately 15% from total losses and remains the same for all considered current densities, while the impact of crossover shows significant sensitivity to the current density demonstrating a downward trend.

---

## VII ACKNOWLEDGMENT

The work was supported by Skoltech NGP Program (Skoltech – MIT joint project).

---

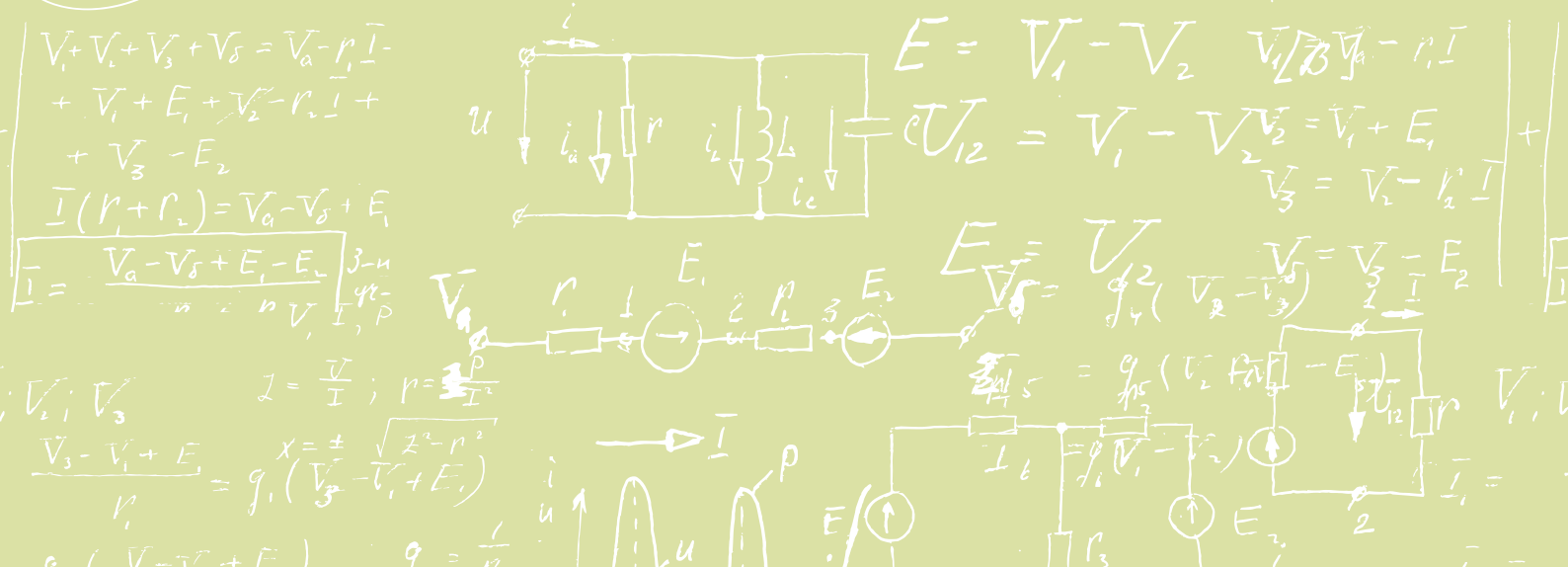
## VIII REFERENCES

- [1] C. Minke, U. Kunz, T. Turek, "Techno-economic assessment of novel vanadium redox flow batteries with large-area cells," *J. Power Sources*, vol. 361, pp. 105–114, Sept. 2017.
- [2] M. Rychcik, M. Skyllas-Kazacos, "Characteristics of a new all-vanadium redox flow battery," *J. Power Sources*, vol. 22, no. 1, pp. 59–67, Jan. 1988.
- [3] M. Aneke, M. Wang, "Energy storage technologies and real life applications – a state of the art review," *Appl. Ener.*, vol. 179, pp. 350–377, Oct. 2016.
- [4] Z. Yang, J. Zhang, M. C. W. Kintner-Meyer, X. Lu, D. Choi, J. P. Lemmon, J. Liu, "Electrochemical energy storage for green grid," *Chem. Rev.*, vol. 111, no. 5, pp. 3577–3613, Mar., 2011.
- [5] V. Viswanathan, A. Crawford, D. Stephenson, S. Kim, W. Wang, B. Li, G. Coffey, E. Thomsen, G. Graff, P. Balducci, M. Kintner-Meyer, V. Sprenkle, "Cost and performance model for redox flow batteries," *J. Power Sources*, vol. 247, pp. 1040–1051, Feb. 2014.
- [6] Y. A. Gandomi, D. S. Aaron, T. A. Zawodzinski, M. M. Mench, "In situ potential distribution measurement and validated model for all-vanadium redox flow battery," *J. Electrochem. Soc.*, vol. 163, no. 1, pp. A5188–A5201, 2016.
- [7] M. Pugach, M. Kondratenko, S. Briola, A. Bischi, "Zero dimensional dynamic model of vanadium redox flow battery cell incorporating all modes of vanadium ions crossover," *Appl. Ener.*, vol. 226, pp. 560–569, Sept. 2018.
- [8] C. Blanc, A. Rufer, "Multiphysics and energetic modeling of a vanadium redox flow battery," in *IEEE Int. Conf. Sustain. Ener. Tech.*, 2008, Singapore, pp. 696–701.

- [9] A. Tang, J. Bao, M. Skyllas-Kazacos, "Studies on pressure losses and flow rate optimization in vanadium redox flow battery," *J. Power Sources*, vol. 248, pp. 154–162, Feb. 2014.
- [10] A. Tang, J. Bao, M. Skyllas-Kazacos, "Thermal modelling of battery configuration and self-discharge reactions in vanadium redox flow battery," *J. Power Sources*, vol. 216, pp. 489–501, Oct. 2012.
- [11] A. Tang, J. Bao, M. Skyllas-Kazacos, "Dynamic modelling of the effects of ion diffusion and side reactions on the capacity loss for vanadium redox flow battery," *J. Power Sources*, vol. 196, no. 24, pp. 10737–10747, Dec. 2011.
- [12] X.-G. Yang, Q. Ye, P. Cheng, T. S. Zhao, "Effects of the electric field on ion crossover in vanadium redox flow batteries," *Appl. Ener.*, vol. 145, pp. 306–319, May 2015.
- [13] Q. Luo, L. Li, Z. Nie, W. Wang, X. Wei, B. Li, B. Chen, Z. Yang, "In-situ investigation of vanadium ion transport in redox flow battery," *J. Power Sources*, vol. 218, pp. 15–20, Nov. 2012.
- [14] B. Turker, S. A. Klein, E.-M. Hammer, B. Lenz, L. Komsiyiska, "Modeling a vanadium redox flow battery system for large scale applications," *Ener. Convers. Manag.*, vol. 66, pp. 26–32, Feb. 2013.
- [15] D.-J. Park, K.-S. Jeon, C.-H. Ryu, G.-J. Hwang, "Performance of the all-vanadium redox flow battery stack," *J. Ind. Eng. Chem.*, vol. 45, pp. 387–390, Jan. 2017.
- [16] S. Kumar, S. Jayanti, "Effect of flow field on the performance of an all-vanadium redox flow battery," *J. Power Sources*, vol. 307, pp. 782–787, Mar. 2016.
- [17] M. Al-Yasiri, J. Park, "A novel cell design of vanadium redox flow batteries for enhancing energy and power performance," *Appl. Ener.*, vol. 222, pp. 530–539, Mar. 2018.
- [18] A. Khazaeli, A. Vatani, N. Tahouni, M. H. Panjeshahi, "Numerical investigation and thermodynamic analysis of the effect of electrolyte flow rate on performance of all vanadium redox flow batteries," *J. Power Sources*, vol. 293, pp. 599–612, Oct. 2015.
- [19] X. Zhang, Y. Li, M. Skyllas-Kazacos, J. Bao, "Optimal sizing of vanadium redox flow battery systems for residential applications based on battery electrochemical characteristics," *Energies*, vol. 9, no. 10, p. 857, Oct. 2016.
- [20] D. You, H. Zhang, J. Chen, "A simple model for the vanadium redox battery," *Electrochim. Acta*, vol. 54, no. 27, pp. 6827–6836, Nov. 2009.
- [21] R. M. Darling, K. G. Gallagher, J. A. Kowalski, S. Ha, F. R. Brushett, "Pathways to low-cost electrochemical energy storage: a comparison of aqueous and nonaqueous flow batteries," *Energy Environ. Sci.*, vol. 7, no. 11, pp. 3459–3477, Sept. 2014.



# Small reviews:



---

# Review of Energy Systems Flexibility Measures and Quantification Approaches

Alvaro Gonzalez-Castellanos\*, Aldo Bischi

---

## Abstract

Renewable energy sources enable both the reduction of emissions and electricity generation at almost zero marginal cost. Nevertheless, their variability presents a challenge for electric systems to balance the net load, demanding the use of flexible measures that can promptly respond to changes in renewable energy generation. This work presents an analysis of the topic of flexibility in energy systems. The main flexibility measures in power systems are categorized and described. Based on the outlined measures, metrics for the quantification of a system's flexibility are reviewed, highlighting the multiple dimensions through which a system's flexibility can be understood and quantified. Lastly, the main challenges for the analysis and quantification of flexibility in energy systems are discussed. The presented work highlights the importance of a multidisciplinary study of energy systems flexibility and the potential areas in which this field can be improved.

---

## Index Terms

Flexibility; multi-energy systems; renewable energy; smart grids.

---

This work was supported by the Next Generation Program: Skoltech – MIT Joint Projects.

\* **A. Gonzalez-Castellanos** is with the Center for Energy Science and Technology, Skolkovo Institute of Science and Technology, Skolkovo Innovation Center, Building 3, Moscow, 121205, Russia (e-mail: alvaro.gonzalez@skolkovotech.ru).

**A. Bischi** is with the Center for Energy Science and Technology, Skolkovo Institute of Science and Technology, Skolkovo Innovation Center, Building 3, Moscow, 121205, Russia (e-mail: a.bischi@skoltech.ru).



---

## I INTRODUCTION

**E**NERGY, especially electric energy, has become an essential commodity in the XXI century. Reliability is a core function of the power system and relates to the system's ability to continuously and adequately supply electrical energy to its users [1]. Electric power interruptions may lead to users' discomfort, considerable economic losses for the industry and disrupt the provision of social services.

The power generated from a renewable energy source fluctuates stochastically, resulting in the variability of a system's net load. For this reason, reliability in power systems must be understood and analyzed in the context of renewable energy generation. A first attempt to formalize the understanding of power system's flexibility was performed by the International Energy Agency in 2009, with its technical report "*Empowering Variable Renewables – Options for Flexible Electricity Systems*" [2]. Given the increase in interest towards renewable energy generation (REGen), the International Energy Agency was tasked by the 2005 Gleneagles G8 Summit to study and provide a report on the necessary measures for the integration of renewable energy sources in large scale power systems. From this report, a fundamental definition of a flexible power system is obtained as "*a flexible electricity system is one that can respond reliably, and rapidly, to large fluctuations in supply and demand*" [2]. The most important factor influencing the need for flexibility in a power system is the supply fluctuation, i.e., variable renewable generation<sup>1</sup>; since the changes in demand have been easier to predict based on decades of industry experience [3].

Another important aspect of this flexibility definition is its relationship with the reliability of power systems operation. These two terms have been used interchangeably in the literature, but must be differentiated to allow for a better understanding of a system's flexibility [4]. Flexibility can be understood as a characteristic of a reliable power system operation. A general and adequate definition of flexibility is given by Alizadeh et al.: "*the ability of a system to deploy its resources to respond to changes in the net load, where the net load is defined as the remaining system load not served by variable generation*" [4].

The variability in the REGen must be assessed under the different operational time frames of interest for the power system: very short duration (milliseconds to 5 minutes), short duration (5 minutes to 1 hour), intermediate duration (1 hour to 3 days) and long duration (several months) [5]. Therefore, the flexibility can be initially understood and quantified as the maximum change in power, also known as ramp, that a system can undergo in a given time frame, e.g., a coal generator that can ramp up 15 MW per hour [3].

---

<sup>1</sup> Renewable generation can be either controllable, e.g., geothermal and large-scale hydropower (impoundment), and variable, e.g., solar and wind.

The purpose of this review is to present an analysis of the flexibility in energy systems. Towards that end, we present the main flexibility measures available for electric power systems. Secondly, we describe available flexibility metrics that expand the flexibility definitions presented above. Finally, we derive the main limitations that arise for an analysis of the flexibility of an energy system.

---

## II FLEXIBILITY MEASURES

For the optimal planning and operation of the power system, the installation and deployment of the available flexibility measures must be done cost-effectively, constrained by the technical limitations of the system [2]. The flexibility of a system can be enhanced by either the standalone or combined use of measures present at the supply and demand side, as well as through network mechanisms.

### A. Supply side

1) *Technical flexibility.* Planning of the generation mix must not be solely based on capacity requirements, but also on the system's ability to provide the necessary flexibility. For this purpose, it is essential to analyze the intraday and seasonal variation of REGen and contrast them with the technical characteristics of the available generation resources [6].

a) *Operating range.* Based on their physical parameters, generation plants usually have a minimum level of electric power production. The difference between this technical minimum and the maximum generation capacity of the unit constitutes the operating range of the power plant. Greater operating ranges and lower technical minima allow for higher absorption of REGen variability [7].

b) *Start-up/shut-down times:* generation units are limited by mechanical and thermal inertia during their start-up and shut-down processes. Usually, operational costs are allocated to represent the amount of fuel "wasted" from the moment in which the unit is turned on and that in which it reaches its minimum generation level. Similarly, operational costs are assigned for the shut-down process. The economic and technical start-up and shut-down characteristics of a power plant have a high influence on its cycling, i.e., its switching on and off to balance load changes [8].

c) *Minimum up and down times.* A generation unit has a characteristic time in which it cannot be turned off once started, and one that restricts its switching on after a shut-down process is completed [9]. Smaller minimum up and down times allow for the more frequent use of a generation unit to balance REGen variability [7].

d) *Ramp rates.* A plant's ability to change its electricity production is limited by its thermal and mechanical inertia, in the same manner as is the plant's time for starting up and shutting down. The maximum change in power generation, upwards and downwards, over a time range that a unit can undergo is known as the ramp rate [7]. Units

with greater ramp rates, usually labelled as faster, provide the system with better response to sudden changes in REGen production.

e) *Fuel flexibility*. In fuel-based generation units, the aforementioned technical characteristics follow the type of prime mover and its primary energy source, i.e., fuel. Therefore, in the designing of power plants, it is necessary to establish the type of fuel employed based on the flexibility requirements [10]. Additionally, some generation technologies allow for the combination of primary energy sources, modifying its technical characteristics, e.g., the blending of biofuels with synthetically generated natural gas [11].

2) *Scheduling flexibility*. Generation units have their participation in the electricity mix based on their technical and economic characteristics [8]. For the flexible operation of a power system it is necessary to consider over a sufficiently long horizon: i) the marginal cost of generation, ii) start-up and shut-down costs, and iii) minimum operation times [6]. Units with higher start-up costs and times are usually used to cover the system's base load for the entirety of the day, e.g., nuclear and coal power plants. Plants with low start-up costs are employed for load-following, i.e., to switch on/off based on small demand variations. An example of load-following generation is hydropower. Finally, when demand peaks occur with higher ramping rates, more flexible generation units are employed, e.g., natural gas combined cycles.

3) *Curtailment*. Excess REGen can be curtailed, i.e., its output can be reduced. REGen curtailment usually follows transmission congestions or excess production during periods of low demand. Even though curtailment reduces the use of green energy, and signals flexibility and transmission capacity problems within the system, curtailed variable REGen can provide ancillary regulation services to the electric grid. Increasing in this manner the system's flexibility and the revenue of REGen projects [12].

## **B. Energy storage**

Electric energy storage can provide load balancing services to the energy system by storing the excess energy produced by the REGen, and by discharging its stored energy when there is a decrease in the REGen output. Given the large variety of energy storage technologies, they can provide multiple services to the electric system based on their technical characteristics, ranging from instantaneous balancing services (in milliseconds) to seasonal shifting (several months) [13].

## **C. Demand side**

1) *Demand side management*. Since the net demand must be balanced at all times, it is possible to reduce the generation requirements by adjusting the consumers demand to offset changes in REGen, i.e., increase/decrease the demand for higher/lower REGen output. Load increase can be applied for valley filling and load growth, whereas demand decrease is applied for peak shaving, and conservation [5]. Additionally, demand can be postponed or advanced through load shifting, i.e., modifying the schedule of a process such as the use of a dishwasher or a step in an assembly line. The modification of the demand is finan-

cially compensated by the system operator based on agreed contracts or the applicable regulation. Users can participate in demand-side management programs, if they are large enough, directly in the electricity market, or with their aggregation through an electricity supplier.

2) *Electric vehicles (EVs)*. Considering that EVs can act either as load or generators by changing the charging/discharging regime of their batteries, they can be used to provide short-term balancing to the power network during the hours in which they are idle and connected to a charging station [14]. EV owners are compensated based on the utilized capacity and type of services provided, e.g., fast charging/discharging or charging interruption.

3) *Building inertia*. Electricity consumption in buildings is not limited to powering consumer appliances but also accounts for the motorizing and controlling of heat, ventilation and air conditioning (HVAC) systems that provide thermal comfort. HVAC systems are operated in a manner that regulates the spaces' temperature and air quality within an established comfort region. The change in temperature and air quality in buildings follows slow processes defined by the physical characteristics of the HVAC system, the building and its surroundings. Therefore, the smart connection/disconnection of HVAC systems permits the modification of the building's demand, while maintaining the comfort conditions within the fixed boundaries [15].

#### D. Network

Proper modeling and operation of power networks can allow the unlocking of flexibility resources commonly "hidden" by conservative engineering limits and jurisdictional barriers for their operation. Being an investment-intensive resource, power networks require accurate assessment of the possible flexibility measures that can delay the installation of new power lines.

1) *Transmission capacity*. Electric energy transmission is performed through insulated conductors ranging from tens of meters to hundreds of kilometers. Each conductor has a rated transmission capacity, in megawatts (MW) or amperes (A), based on its thermal characteristics. Traditionally the lines' thermal rating is considered as a constant parameter, based on manufacturer information and the average temperature at the installation site. In reality, the transmission capacity of a power line changes with weather parameters, such as solar radiation, temperature, and wind speed, thus allowing for the transmission of higher amounts of power when higher wind speeds occur [16].

2) *Balancing areas*. Net load balancing must be achieved for the electric power system as a whole, but it is possible to diminish the flexibility requirements for one area, i.e., electric jurisdiction, via its interconnection with adjacent ones [7]. The different load and REGen profiles, as well as the flexibility resources, can be shared among the areas for balancing while providing economic benefits for those that provide flexibility services. An example of large-scale aggregation of balancing areas is the NordPool market, which allows the transmission of cheap Danish wind generation, balanced by controllable Norwegian hydroelectricity [2].

3) *Import/export interconnections*. Analogously to the use of balancing areas, it is possible

to increase a system's flexibility via electricity import and export. In the case of importing and exporting, the balancing of the area is not ensured by a centralized controller but instead aided by the transmission of electricity between two systems based on commercial contracts.

## E. Multi-energy systems

Electric power systems are already connected to other energy systems, such as district heating networks through cogeneration units, district cooling through trigeneration plants, gas networks for fuel supply to the power plants, among others. This interconnection between multiple energy carriers was firstly categorized by Geidl and Andersson as an *energy hub* [17]. An energy hub is a system where multiple energy carriers can be converted, conditioned and stored for the supply of users' demand. The energy hub concept introduced the notion of supply flexibility to the already existing literature of integrated energy infrastructures, which was mostly addressing costs and emissions reduction. The increase in the system's flexibility is achieved through the synergy between the different subsystems and their characteristics, i.e., electricity can be efficiently transmitted over long distances, gas and chemical carriers can be cheaply stored, and heating and cooling networks count with thermal inertia, which allows them to act as an energy buffer through slow energy release [18].

The redundancy of connections between the supply and demand sides also allows increasing the system flexibility and ensuring its optimum economic operation. Connection redundancy can be seen in the generation units that link the different energy systems together, e.g., heat pumps, co- and tri-generation units.

1) *Flexibility in thermal networks.* Unlike electric processes which occur almost instantly, thermal systems have an intrinsic source of inertia in the form of thermal capacity [19]. Sources of inertia in thermal networks can be found in heat/cold carrier fluids, thermal energy storage, and buildings. With the use of cogeneration plants, which produce both electricity and heat from fossil fuels, it is possible to transfer the variability of REGen to the thermals systems. For example, during periods of high REGen production, it is possible to produce more heat and less electricity, allowing the thermal inertia of the system to accumulate the extra heat and release it during hours where the REGen is lower and more electricity is needed. This type of operation would allow maintaining the plant's efficiency at an optimum level since the first principle thermodynamic efficiency of a cogeneration plant is a function of the generated heat and electricity.

2) *Electricity-to-thermal energy.* In a similar way to the flexible use of the cogeneration plant to harness the heating network thermal inertia, it is possible to directly transfer the increase in REGen by converting the excess electricity into thermal energy through the use of heat pumps [20]. Thus, not only increasing the system's flexibility, but also reducing its fuel-related costs and emissions.

3) *Power-to-gas.* The use of natural gas as a fuel for power plants has enabled their use for load balancing when higher ramping levels are required, in detriment of slower coal

plants. Synthetic natural gas can be produced during high REGen periods, to be either locally consumed, transported through the gas network or stored for later consumption [21]. Therefore, allowing its use for balancing in very short duration or as seasonal storage.

4) *Power-to-hydrogen*. As with synthetic natural gas, it is possible to generate hydrogen from excess electricity (through electrolysis) [5]. The produced hydrogen can then be injected into natural gas networks, under safety limits for its blending, for powering natural gas plants [22]. The injection of hydrogen in gas networks allows reducing the overall system's emissions.

5) *Power-to-liquid*. An alternative to the conversion of excess REGen electricity into gas fuels is its use for the production of liquid fuels. By combining CO<sub>2</sub>, water and electricity, it is possible to produce synthetic gas that can then be processed into liquid hydrocarbons for transportation and base chemical materials [23].

6) *Renewable energy desalination*. In remote desert locations there is usually an abundance of sun, wind, or both, and a lack of easy access to fresh water. Renewable energy can be employed to produce both the heat and electricity required for the water desalination process, either by direct production with the use of concentrated solar power or by combining heat pumps with solar photovoltaic and wind generation [24]. Water desalination plants can be employed as demand response mechanisms that can modify the systems' net load when required by locally consuming excess renewable power generation.

---

### III FLEXIBILITY QUANTIFICATION

Integration of REGen technologies in energy systems requires assessing not only their contributions in meeting capacity requirements, but also their impact on net load dynamics. Lack of consideration of the system's operational requirements during the planning process could lead to the violation of flexibility requirements and increase the project's overall cost with the ex-post installation of flexibility measures [25]. Therefore, it is necessary to develop methodologies for the estimation of a system's flexibility, which characterize the system's behavior during its different operation timeframes [7].

The IEA's technical report "*Empowering Variable Renewables – Options for Flexible Electricity Systems*" defined a system's net flexibility resource (NFR) as a metric for the estimation of the amount of variable REGen that can be installed in a system [2]. The NFR is calculated as the difference between the available flexibility measures and the required flexibility. The available flexibility resources are measured as ramps (power over time) over different time ranges. Generation ramps, transmission interconnection, demand response, and energy storage are included in the calculation of the available

flexibility. The flexibility requirements account the forecasted variability in demand, probable contingencies and the variability in REGen. A normalized NFR against the system's installed capacity allows the comparison between different systems and reflects their capability of REGen introduction, based on their generation mix and existing regulation.

The North American Electric Reliability Corporation proposed the quantification of the flexibility requirements for net load variations based on the metrics of magnitude, ramp response, and frequency [7]. The magnitude relates to the maximum power variation; the ramp response relates to the event's magnitude with the analyzed time frame (15 min., 30 min., one hr.); and finally, the frequency quantifies how often does the event occur. A fourth dimension to the variability of REGen is the event's intensity, which combines the event's magnitude and ramp response. Variability events with high magnitude and short duration derive into high flexibility requirements to the system, i.e., they are high-intensity events. Proper classification of the REGen variability events based on their frequency and intensity would allow a system planner/operator to optimally decide the necessary flexibility measures to be installed/operated to meet the reliability requirements.

The flexibility assessment (FAST) method proposed by the IEA was an extension of the NFR and sets the methodology for the proper dimensioning of a system's capability to install variable REGen [3]. The FAST method identifies bottlenecks in the deployment of flexibility measures and follows four main steps:

- i. Quantify the installed technical flexibility resource (TR), as for the NFR.
- ii. Based on system conditions, analyze the TR that is available for use, i.e., the available flexible resources (AFR) that are not limited by transmission, market, and environmental constraints.
- iii. Calculate the system's flexibility requirement (FR), as done for the NFR.
- iv. By establishing the remaining flexibility resource,  $AFR - FR$ , it is possible to establish the system's Present VRE Penetration Potential (PVP).

Obtaining a system's PVP for different time scales and seasons, enables the proper dimensioning of the maximum variable REGen that can be installed, not only by capacity but also by technology.

Denholm and Hand introduced a normalized metric for the calculation of the maximum demand share of a system's that can be met by introducing variable REGen [26]. The proposed Renewable Energy Flexibility (REFlex) method, considers only the installed generation capacity at its minimum generation level, does not include controllable REGen such as hydropower, nor quantifies the flexibility introduced by transmission interconnection. REFlex simulates hourly load balances with the installed thermal capacity and different variable REGen technologies. The REFlex curtails excess variable REGen when necessary, thus providing a metric for the need of flexibility measures in the system, correspondent to the considered variable renewable resource.

Ma et al. establish the net flexibility index (NFI) for the evaluation of generators' contribution to the overall system flexibility [27]. A generator's NFI is calculated as the averaged sum of its operating range and ramp, divided by the system's installed capacity. The NFI can be used to characterize the system's generation units as flexible (above the average NFI) and inflexible (below the system's average). This classification, combined with the units' marginal costs, allows the system operator to prioritize the use of generators during periods of high REGen variability. Additionally, Ma et al. provided in the same work a metric for the estimation of the expected number of hours during which wind curtailment could take place, labeled as loss of wind estimation (LOWE). The LOWE represents the probability of a system's generation being unable to flexibly balance the variations in the net demand due to: i) having a minimum generation level below the net load, ii) not following quickly enough ramp-down events, and iii) having a maximum ramp-up slower than the net load increase. Probabilistic data for the wind characterization can be used in combination with the systems' flexibility characteristics (minimum generation levels, cumulated ramp-up and -down) to estimate the LOWE for different levels of wind penetration.

With the aim to quantify a system's ability to meet the expected and unexpected ramping requirements, Lannoye et al. proposed a methodology for the calculation of insufficient ramping resource expectation (IRRE) [6]. Based on the expected demand, variable REGen generation and scheduled generation, the IRRE is calculated via the following steps:

- i. Estimate the upward and downward ramping requirements for the time horizons of interest.
- ii. Calculate the available ramping capabilities of the generation units based on their scheduled operation.
- iii. Calculate the system's available flexibility distribution (AFD). The  $AFD(X)_t$  indicates the probability, for each time horizon  $t$ , that a ramping requirement  $X$  cannot be met by the available flexibility resources.
- iv. Based on the estimated ramping requirements and the AFD, calculate the insufficient ramp resource probability (IRRP).
- v. Finally, the IRRE (for upwards and downward ramping) is obtained as the summation of the IRRP over the entire time series in the chosen time horizon.

As with the LOWE, the IRRE provides the system operator with an index for the quantification of the system's reliability, through the analysis of its flexibility capabilities.

So far, the reviewed works have focused on a system's ramping capabilities to quantify its flexibility. Nuytten et al. propose the analysis of a combined heat and power (CHP) system flexibility by estimating its resilience, i.e., the number of hours that it can entirely operate with one of its generation resources, either with a cogeneration unit or an energy storage system [28]. For this purpose, they analyzed the system under two operation modes: delayed operation flexibility and forced operation flexibility. For the



delayed operation flexibility, the system is set to use only the cogeneration unit, while the energy storage is charging. Whereas in the forced operation flexibility, the demand is balanced solely by the use of the energy storage. The maximum number of hours that the system can endure in these operation regimes is calculated for each time step of the time horizon of interest. This type of quantification allows in planning stages the estimation of the impact of the units' sizes in the overall system flexibility and resilience. The flexibility contribution of a flexibility measure can be characterized by its power capacity  $\pi$  in MW, its maximum ramp rate  $\rho$  in MW/min, its energy provision capacity  $\varepsilon$  in MWh, and ramp duration  $\tau$  in min [29]. Since the ramp duration can be derived from the selected time horizon and the energy provision capacity, the characterization of a flexibility measure can be performed with  $\pi$ ,  $\rho$ , and  $\varepsilon$ . Additionally, each flexibility dimension can be set with a minimum and a maximum value, or + and -, i.e.,  $\pi^{+/-}$  are respectively the minimum and maximum power generation levels (of negative value if power consumption is present),  $\rho^{+/-}$  represent the upward and downward ramp rates, and  $\varepsilon^{+/-}$  the maximum energy that a measure can produce (positive) and receive (negative). Based on this flexibility metrics, Ulbig and Andersson proposed a simple method for the quantification of a system's flexibility capability, the flexibility required by a variable resource and event, and the remaining flexibility after the requirements are satisfied [30]. The aggregated flexibility of a system and the total flexibility requirement can be calculated by a Minkowski summation of its flexibility metrics. For example, the aggregated system ramps are calculated by

$$\rho_{total}^+ = \sum_{g \in units} \rho_g^+ \quad (1)$$

$$\rho_{total}^- = \sum_{g \in units} \rho_g^- \quad (2)$$

The Minkowski summation is used analogously for estimating  $\pi$  and  $\varepsilon$ . Once  $\pi$ ,  $\rho$ , and  $\varepsilon$  are calculated for both the flexibility measures and requirement, they can be subtracted (dimension by dimension) for the estimation of the remaining flexibility available. The one by one comparison of a system's aggregated flexibility resource and its required flexibility allow to identify possible limitations of its resilient operation, i.e., if at least one of the dimensions of the aggregated available flexibility is lower than its required counterpart, the system will fail to match the net load variability in that respective component. Additionally, by being able to represent the flexibility characteristics of a given measure in a tridimensional space, it is possible to easily compare the strengths and weaknesses of the analyzed flexibility measure, and compare it with other viable options. This type of comparison between a storage and a conventional generation unit is presented in Fig. 1. In the figure it can be seen how the generation unit is more suitable for balancing events that require higher amounts of energy, while the storage unit can provide a faster response, for both up and down ramps.

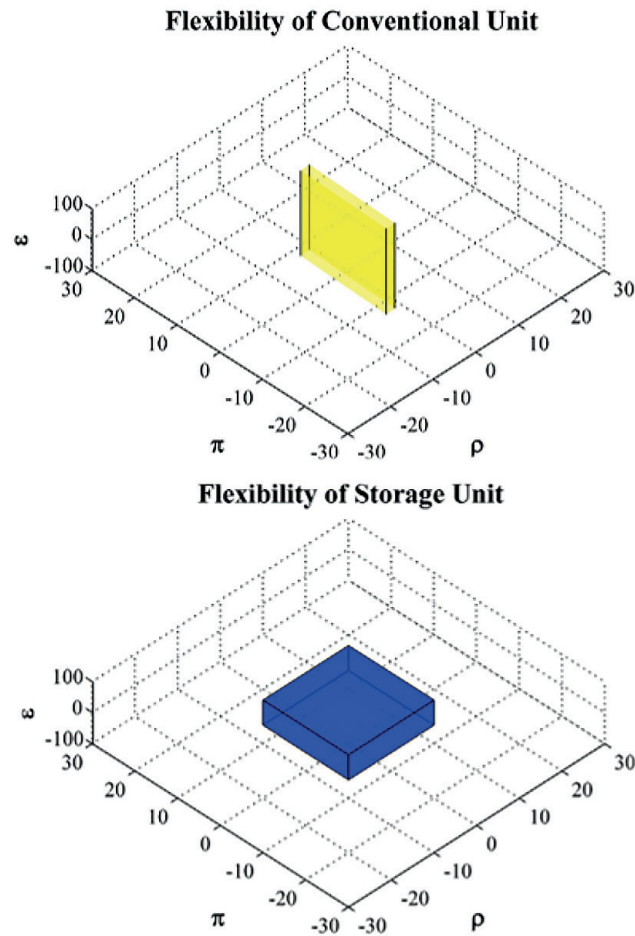


Fig. 1. Flexibility volumes for a conventional generation unit (yellow) and an energy storage unit (blue) [30].

The characterization of the flexibility in buildings through a cost curve has been proposed by DeConinck and Helsens [31]. The flexibility of a building can be quantified as the maximum deviation from its optimal energy consumption while maintaining the comfort levels within the established boundaries. Higher deviations from the optimal setting yield higher costs for the building operator, which can be translated into cost curves and furtherly characterized for different time frames in which the flexibility can be requested. The comparison of the buildings' cost curves can be used by an aggregator to decide the activation order for demand response mechanisms.

A more technical approach in the definition of a building's flexibility, via analysis of its transient response, is provided by Junker et al. [15]. The authors propose a flexibility function (FF) composed of 6 measures, shown in Fig. 2, for the quantification of a building's response to a change in its operation:

- $\tau$ : the time delay between the control signal and the building's response;
- $\Delta$ : the maximum power reduction in the load during the response;
- $\alpha$ : time between the start of the response and reaching ;
- $\beta$ : total time of decreased demand;
- $A$ : total energy reduction;
- $B$ : total extra energy consumed to return the system to the equilibrium estate.

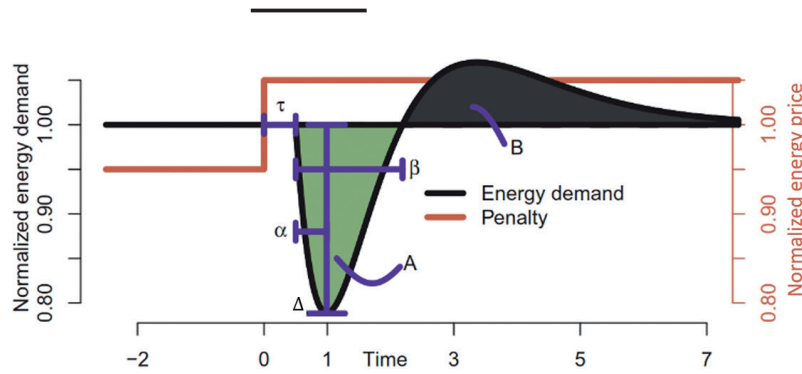


Fig. 2. Flexibility characteristics of a building based on its response dynamics [15].

The proper assessment and comparison of the response characteristics of buildings and loads, in general, could allow a flexibility aggregator to match flexibility measures with variability events. For instance, if the wind resource has faster oscillations with small power changes, then it is necessary to activate a load with a smaller  $\tau$  and  $\alpha$ , and not so great  $\Delta$ . These flexibility measures, in conjunction with the flexibility cost curves introduced by DeConinck and Helsen [31], could provide a system operator with a base for the enhancement of the flexible operation of an energy system.

A building's flexibility function could be used for the calculation of a normalized flexibility index. This index reflects the reduction of its operation objective when it is operated smartly, i.e., how much is the system's objective function reduced (operation cost, maximum peak, hours of energy import, among others) when a signal for the activation of the flexible operation is sent, in comparison with its standard operation. Thus, allowing quantification of the benefits introduced by the use of different flexibility measures under different operation objectives.

The provision of flexibility from microgrids to the transmission system has gained interest in the power system community and is known as the “*distribution and transmission system operator (DSO-TSO) interconnection*”. Contreras and Rudion provided a methodology for calculating the flexibility range of a microgrid (in terms of active and reactive power) for DSO-TSO coordination, by defining each of its flexibility measures with a characteristic polygon, limited by linear inequalities [32]. A flexibility measure is thus defined by the region in which it can operate, based on its current operation point and its ramp rates, for both active and reactive power. The authors categorized different flexibility measures into five types, based on the shape of their flexibility ranges. The flexibility regions of the five types are presented in Fig. 3, and are characterized as follows:

- Type 1: this type of units has fixed minimum and maximum bounds for their active and reactive power production. The bounds  $P_A$ ,  $P_B$ ,  $Q_A$ , and  $Q_B$ , can be adjusted to represent a wide range of devices, such as full converter wind generators ( $P_B=0$ ), capacitor banks ( $P_A=P_B=0$ ), among others.
- Type 2: this type represents the units with constant power factor  $\cos \phi$ , i.e., the ratio between active and reactive power consumption.

- Type 3: this type represents wind generators with doubly fed induction generators and rotor side converters. This set of units has a limited production of reactive power, set by the inverter, for lower active power levels.
- Type 4: the reactive power production of a photovoltaic system can be regulated by modifying its power factor within the allowed range.
- Type 5: synchronous generators can be modeled as having maximum apparent power ( $S = \sqrt{P^2 + Q^2}$ ), and subsequently approximating the area in its operating range through piecewise linearization.

Once the available flexibility measures are characterized based on their flexibility regions, their aggregation can be performed through the optimization of the boundary points that satisfy the system's technical constraints. The aggregated flexibility region, along with the operation point, can then be sent to the TSO for the use for net load balancing. It must be noted that the presented methodology can be expanded by performing it for each time step of DSO-TSO coordination, and must not only consider the present time step but a time horizon that adequately characterizes the changes in the microgrid operation.

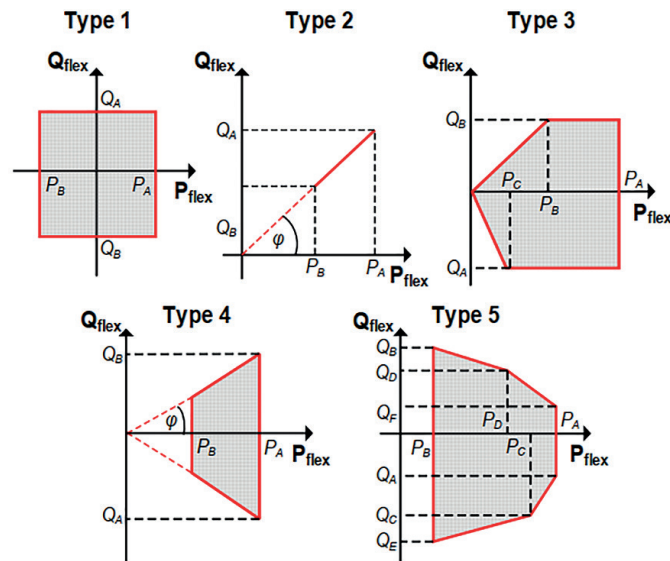


Fig. 3. Flexibility region for different types of units [32].

#### IV FLEXIBILITY LIMITING FACTORS

As seen in the previous sections, there is no unified framework for the quantification of a system's flexibility. The lack of consensus in the literature corresponds to the extensive array of flexibility measures within the electric power system, and the additional layers of complexity introduced by its interconnection with other energy systems. Unlocking flexibility through the centralized operation of multi-energy systems albeit technically feasible must also correspond with the

seamless coordination of the different energy markets, which operate at different time scales [4].

An additional limitation for the flexibility analysis of energy systems is the gap existing between the control layer (order of a second) in which the flexibility measures must operate and the planning horizon (in years) for the sizing and selection of these measures. The flexibility study must also include the stochastic nature of variable renewable resources, which increases the mathematical complexity of full system consideration.

Finally, decentralized control and communication infrastructures must be developed for the optimal coordination of the different flexibility and energy systems to enable a fast and cost-effective response to variable REGen.

---

## V CONCLUSIONS AND OUTLOOK

This paper presents a comprehensive analysis of the primary methodologies for the flexibility quantification in energy systems. The wide range of flexibility measures in electric networks and their possible interconnection with other energy systems provide a challenging and attractive field for the developing of market, communication, control, and planning strategies for the flexible operation of power systems.

A holistic methodology for the quantification of flexibility in integrated energy systems in a multi-temporal and stochastic manner is necessary to unlock existing system capabilities, without incurring new investments.

---

## VI REFERENCES

- [1] R. Billinton, R. N. Allan, "Power-system reliability in perspective," *Electron. Power*, vol. 30, no. 3, pp. 231–236, Mar. 1984.
- [2] International Energy Agency, "Empowering Variable Renewables – Options for Flexible Electricity Systems," OECD, Oct. 2009.
- [3] International Energy Agency and Organisation for Economic Co-operation and Development, Eds., *Harnessing variable renewables: a guide to the balancing challenge*. Paris: OECD/IEA, 2011.
- [4] M. I. Alizadeh, M. Parsa Moghaddam, N. Amjady, P. Siano, M. K. Sheikh-El-Eslami, "Flexibility in future power systems with high renewable penetration: A review," *Renew. Sustain. Energy Rev.*, vol. 57, pp. 1186–1193, May 2016.
- [5] P. D. Lund, J. Lindgren, J. Mikkola, J. Salpakari, "Review of energy system flexibility measures to enable high levels of variable renewable electricity," *Renew. Sustain. Energy Rev.*, vol. 45, pp. 785–807, May 2015.
- [6] E. Lannoye, D. Flynn, M. O'Malley, "Evaluation of power system flexibility," *IEEE Trans. Power Syst.*, vol. 27, no. 2, pp. 922–931, May 2012.
- [7] North American Electric Reliability Corporation, "Flexibility Requirements and Metrics for Variable Generation: Implications for System Planning Studies," Princeton, NJ, Aug. 2010.
- [8] L. M. Abadie, "Operating flexibility at power plants: A market valuation," *Int. J. Electr. Power Energy Syst.*, vol. 64, pp. 41–49, Jan. 2015.
- [9] M. F. Anjos, A. J. Conejo, "Unit commitment in electric energy systems," *Found. Trends Electr. Energy Syst.*, vol. 1, no. 4, pp. 220–310, 2017.

- [10] L. M. Abadie, J. M. Chamorro, "Valuing flexibility: The case of an integrated gasification combined cycle power plant," *Energy Econ.*, vol. 30, no. 4, pp. 1850–1881, Jul. 2008.
- [11] S. Rahm, J. Goldmeer, M. Moliere, A. Eranki, "GER-4601 – Addressing gas turbine fuel flexibility," presented at the POWER-GEN Middle East, Manama, Bahrain, 2009, p. 14.
- [12] L. Bird, J. Cochran, X. Wang, "Wind and solar energy curtailment: experience and practices in the United States," NREL/TP-6A20-60983, 1126842, Mar. 2014.
- [13] Robin Wiltshire, Ed., *Advanced District Heating and Cooling (DHC) Systems*. Elsevier, 2016.
- [14] K. Uddin, M. Dubarry, M. B. Glick, "The viability of vehicle-to-grid operations from a battery technology and policy perspective," *Energy Policy*, vol. 113, pp. 342–347, Feb. 2018.
- [15] R. G. Junker, A. G. Azar, R. A. Lopes, K. B. Lindberg, G. Reynders, R. Relan, H. Madsen, "Characterizing the energy flexibility of buildings and districts," *Appl. Ener.*, vol. 225, pp. 175–182, Sep. 2018.
- [16] M. Tschampion, M. A. Bucher, A. Ulbig, G. Andersson, "N-1 security assessment incorporating the flexibility offered by dynamic line rating," in *2016 Power Systems Computation Conference (PSCC)*, pp. 1–7, 2016.
- [17] M. Geidl, G. Andersson, "A modeling and optimization approach for multiple energy carrier power flow," in *2005 IEEE Russia Power Tech*, pp. 1–7, 2005.
- [18] M. Geidl, G. Koepfel, P. Favre-Perrod, B. Klockl, G. Andersson, K. Frohlich, "Energy hubs for the future," *IEEE Power Energy Mag.*, vol. 5, no. 1, pp. 24–30, Jan. 2007.
- [19] A. Vandermeulen, B. van der Heijde, L. Helsen, "Controlling district heating and cooling networks to unlock flexibility: A review," *Energy*, vol. 151, pp. 103–115, May 2018.
- [20] C. Finck, R. Li, R. Kramer, W. Zeiler, "Quantifying demand flexibility of power-to-heat and thermal energy storage in the control of building heating systems," *Appl. Energy*, vol. 209, pp. 409–425, Jan. 2018.
- [21] S. Clegg, P. Mancarella, "Storing renewables in the gas network: modelling of power-to-gas seasonal storage flexibility in low-carbon power systems," *Transm. Distrib. IET Gener.*, vol. 10, no. 3, pp. 566–575, 2016.
- [22] M. W. Melaina, O. Antonia, M. Penev, "Blending Hydrogen into Natural Gas Pipeline Networks: A Review of Key Issues," National Renewable Energy Laboratory, NREL/TP-5600-51995, Mar. 2013.
- [23] H. Blanco, W. Nijs, J. Ruf, A. Faaij, "Potential for hydrogen and Power-to-Liquid in a low-carbon EU energy system using cost optimization," *Appl. Energy*, vol. 232, pp. 617–639, Dec. 2018.
- [24] A. Alkaisi, R. Mossad, A. Sharifian-Barforoush, "A Review of the Water Desalination Systems Integrated with Renewable Energy," *Energy Procedia*, vol. 110, pp. 268–274, Mar. 2017.
- [25] M. Welsch, P. Deane, M. Howells, B. Ó Gallachóir, F. Rogan, M. Bazilian, H.-H. Rogner, "Incorporating flexibility requirements into long-term energy system models – A case study on high levels of renewable electricity penetration in Ireland," *Appl. Energy*, vol. 135, pp. 600–615, Dec. 2014.
- [26] P. Denholm, M. Hand, "Grid flexibility and storage required to achieve very high penetration of variable renewable electricity," *Energy Policy*, vol. 39, no. 3, pp. 1817–1830, Mar. 2011.
- [27] J. Ma, V. Silva, R. Belhomme, D. S. Kirschen, L. F. Ochoa, "Exploring the use of flexibility indices in low carbon power systems," in *2012 3<sup>rd</sup> IEEE PES Innovative Smart Grid Technologies Europe (ISGT Europe)*, Berlin, Germany, pp. 1–5, 2012.
- [28] T. Nuytten, B. Claessens, K. Paredis, J. Van Bael, D. Six, "Flexibility of a combined heat and power system with thermal energy storage for district heating," *Appl. Energy*, vol. 104, pp. 583–591, 2013.
- [29] Y. V. Makarov, C. Loutan, J. Ma, P. de Mello, "Operational Impacts of Wind Generation on California Power Systems," *IEEE Trans. Power Syst.*, vol. 24, no. 2, pp. 1039–1050, May 2009.
- [30] A. Ulbig, G. Andersson, "Analyzing operational flexibility of electric power systems," *Int. J. Electr. Power Energy Syst.*, vol. 72, pp. 155–164, Nov. 2015.
- [31] R. De Coninck, L. Helsen, "Quantification of flexibility in buildings by cost curves – Methodology and application," *Appl. Energy*, vol. 162, pp. 653–665, Jan. 2016.
- [32] D. A. Contreras, K. Rudion, "Improved Assessment of the Flexibility Range of Distribution Grids Using Linear Optimization," in *2018 Power Systems Computation Conference (PSCC)*, pp. 1–7, 2018.

---

# Alterations of Organic-Rich Shales during Heating: An Overview

Tagir I. Karamov\*

---

## Abstract

As recovery from conventional reservoirs decreases, there is a growing need to involve unconventional reserves such as an oil shale into development. As an alternative to hydraulic fracturing for shales, high temperature treatment is being implemented to enhance oil recovery. This overview focuses on the main insights and the most important results of experimental investigations of shale alterations during high temperature treatment. Most of the authors observed that organic matter starts to decompose at the temperature about 200° C with a generation of new hydrocarbons called "synthetic". And at 600-650° C organic matter disappears completely, which leads to the formation of a new void space with the increased porosity and permeability. Moreover, different thermal expansion of the shale components causes fracturing. Despite the numerous investigations of the process there are still open questions such as alteration of structure of pore structure formed after organic matter decomposition and changes in rock mineral matrix during the heating. Deep understanding and ability to control the mentioned processes allow efficient recovery of hydrocarbons from organic-rich shales.

---

## Index Terms

Combustion; green river; heating; pyrolysis; thermal alteration; thermal treatment; unconventional reservoir.

---

## I NOMENCLATURE

OM	organic matter
HC	hydrocarbons
TOC	total organic carbon
CT	computer tomography
TC	thermal conductivity
Fm	formation

---

\* **T.I. Karamov** is with the Center for Hydrocarbon Recovery, Skolkovo Institute of Science and Technology, Skolkovo Innovation Center, Building 3, Moscow, 121205, Russia (e-mail: tagir.karamov@skoltech.ru).

---

## II INTRODUCTION

**W**ITH the global growth of energy demand and decrease of conventional reserves recovery, the unconventional hydrocarbons have attracted increasing attention. Significant part of unconventional reserves is concentrated in shale reservoirs, which are a source rocks with retained hydrocarbons and kerogen over geological time inside its mineral matrix [1], [2].

Organic-rich shales are fine-grained sedimentary rocks enriched with organic matter. The main components are quartz, clays, carbonates, pyrite and organic matter. These types of rocks are characterized by high heterogeneity in macro- and micro- scales due to peculiarities in the distribution patterns of OM and mineral composition [3]. These rocks have very complicated nanoscale pore system (often controlled by OM) which is a reason of extremely low porosity and permeability coefficients [4].

High heterogeneity, low porosity and permeability make conventional technologies inapplicable for organic-rich shales. Only several approaches may be used to recover hydrocarbons from such types of rocks: hydraulic fracturing and thermal treatment technologies. Hydraulic fracturing may be quite effective for shale oil and gas extraction, but it requires significant volumes of water. This procedure can cause water pollution and other potential ecological hazards. Many formations in the world contain significant amount of HC in the form of kerogen (for example Bazhenov Fm in Russian Federation), and hydraulic fracturing will be futile in terms of kerogen potential transformation into HC. Thermal treatment is a technology that can be effective in conversing kerogen into the gaseous and liquid hydrocarbons with its further extraction [1], [5].

Heating of the shales leads to changes in the structure, composition and physical properties [6]. Details of the alterations during heating are poorly known; only rock structure and OM decomposition process have been analyzed to some extent by several authors [1]-[14]. Understanding of these alterations is crucial for effective implementation of the technology and further oil and gas recovery.

This overview is devoted to the most significant experimental investigations of organic-rich shale alterations during heating.

---

## III EXPERIMENTAL INVESTIGATIONS OF ORGANIC-RICH SHALES DURING HEATING

One of the first experiments aimed to investigate shale alterations during heating was performed by Tisot [7] in 1967. Seven samples from the Green River Fm with different OM content were collected and heated under controlled conditions up to 815° C in stress free conditions (Fig. 1). Physical properties were evaluated before and after heating. The main results are as follows:



- decomposition of OM continued up to 400° C;
- porosity and permeability increase with temperature rise;
- new fractures along lamination appeared after heating;
- weight loss is associated with OM decomposition.



Fig. 1. Structural alterations of samples before and after experiment [7].  
 A – raw samples; B-C – samples heated to 400° C; D-E – samples heated to 815° C.

Later, in 1975, Prats conducted similar experiment on Green River Oil Shales [8] with the aim to estimate thermal properties changes during heating. Four sets of samples were collected from different locations of the Green River Formation with different TOC. Thermal conductivity was measured with the transient line heat-source (probe) method. Samples were heated in the special oven. Prats showed that the thermal conductivity decreases (up to 30%) as the temperature increases (Fig. 2).

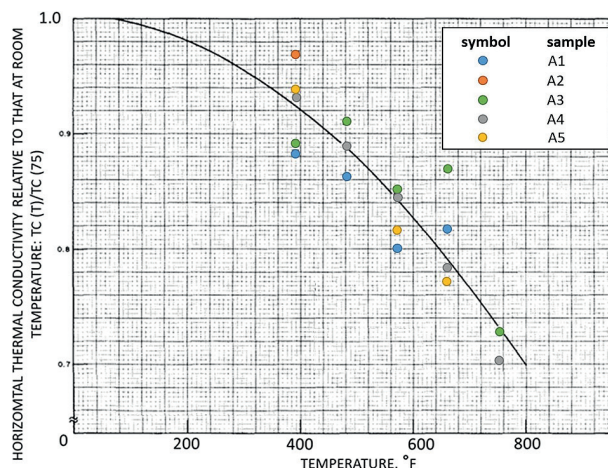


Fig. 2. Thermal conductivity change with temperature growth [8].

Prats concluded that the thermal conductivity of organic-rich shales is affected by degree of kerogen conversion into fluid products; the fraction of converted kerogen is controlled by temperature history.

Decades later in 2013 similar experiment was performed in Salt Lake City by Tiwari et al. [9]. Three samples from Green River Fm with different TOC were collected for the investigation and split into three parts (Fig. 3).

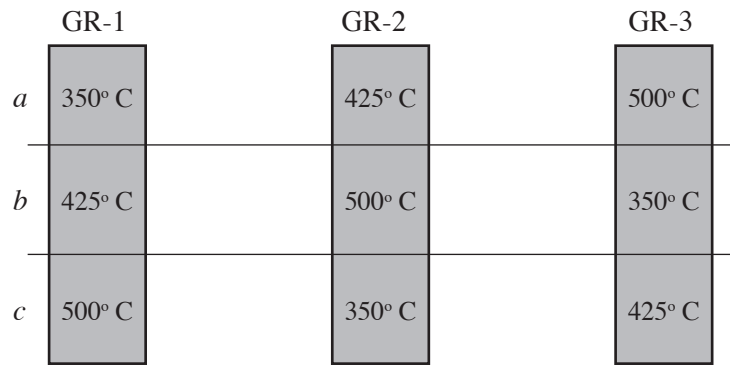


Fig. 3. Green River samples subjected to pyrolysis at different temperatures [9].

The samples were subjected to pyrolysis at different temperatures: 350° C, 425° C and 500° C in the N<sub>2</sub> atmosphere during 24 hours. After heating the weight of all samples has fallen according initial TOC content: higher TOC larger the weight loss (Table I, Table II).

TABLE I. Results of elemental analysis of the samples [9]

	GR-1	GR-2	GR-3
<b>Hydrogen</b>	2.71	1.52	2.19
<b>Total carbon</b>	25.44	17.66	20.25
<b>Total CO<sub>2</sub> as C</b>	5.17	7.33	4.79
<b>Organic Carbon</b>	20.27	10.33	15.46
<b>Nitrogen</b>	0.73	0.34	0.65
<b>Oxygen</b>	16.94	21.85	16.46
<b>Sulfur</b>	0.83	0.29	0.95

TABLE II. Weight loss of the samples [9]

Core	ID of sample	Temperature (°C)	Weight loss (%)
GR-1	1a	350	7.08
	1b	425	25.91
	1c	500	33.74
GR-2	2c	350	2.84
	2a	425	9.61
	2b	500	12.26
GR-3	3b	350	2.54
	3c	425	18.40
	3a	500	17.17

Moreover, samples characterized with the high TOC content were destroyed after temperature treatment (Fig. 4).

All samples were investigated with the micro-CT method. The authors demonstrated that new pores and fractures are associated with OM veins and lenses.

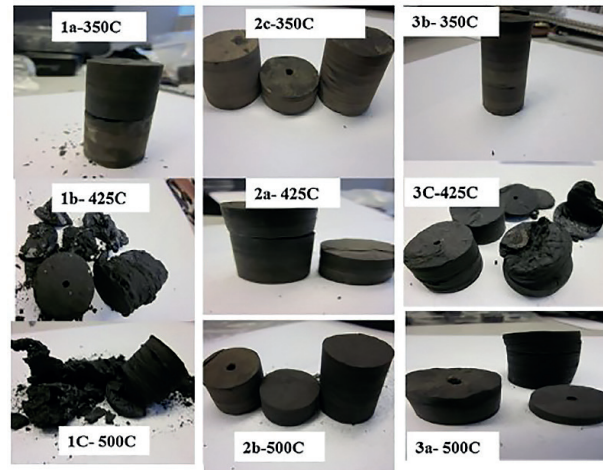


Fig. 4. Samples after pyrolysis [9].

Fig. 5 shows the image of GR-1 sample after 425° C temperature. The sample contained around 20% of TOC, after heating the major part of OM was decomposed, and a new pore space was formed. The generated void space is patchy and consistent with the initial OM distribution along laminae.

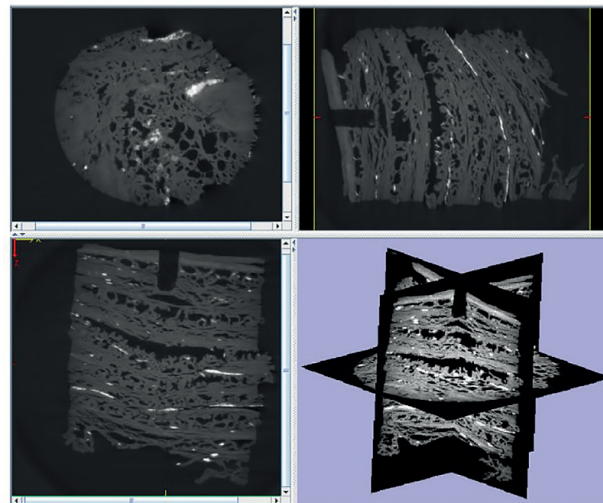


Fig. 5. Sample GR-1 (1b) after heating up 425°C [9].

The authors confirmed the previous results [1]-[5] using micro-CT. Heating of the samples with high TOC content leads to generating a new void space, and distribution of these voids is strongly controlled by OM distribution.

An identical experiment was accomplished by Chinese researchers on Daqing and Yan'an Formations (analogs of Green River Fm) [10] for two samples with different TOC content and structures. The samples were heated to the temperatures 100° C, 200° C,

300° C, 400° C, 500° C, 600° C in the pyrolysis reactor. At the temperature of 200° C new fractures started to form with the beginning OM destruction (Fig. 6). The main method for void space evaluation was also micro-CT.

The main issue of all described experiments is repeated cycles of cooling and heating of the samples: they are cooled to room temperature in order to make a micro-CT scan, then heating continues. Researchers from the University of Oslo overcame this problem [11]. Kobchenko with colleagues performed time-resolved X-ray tomography imaging of the sample during heating (from 60° to 400° C) from Green River Fm.

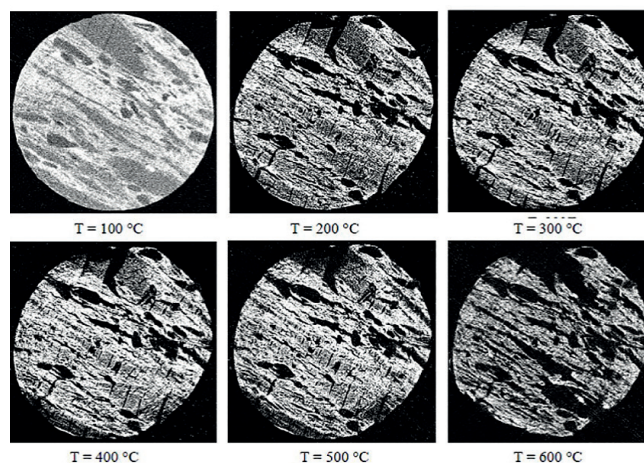


Fig. 6. Micro-CT images of the sample during heating [10].

At the temperature about 350° C, fractures along the bedding started to form in conformity with the previous experiments. Authors argue that new cracks that occurred at 350° C were associated with significant mass loss and release of light hydrocarbons generated by the decomposition of OM. Decomposition of kerogen caused an internal pressure build up enough to generate fractures in the sample.

---

#### IV DISCUSSION AND CONCLUSIONS

In many recent papers researchers confirmed that similar fractures appear in different organic-rich shales during heating [12]-[16]. But except fractures new pores are formed during heating in the space, which initially was occupied by OM. And there are significant uncertainties with this type of void space, which is formed after OM decomposition. Particularly, authors did not consider its volume, connectivity and structure. Since organic-rich shales contain up to 20-25% of OM these voids may have a profound impact on porosity and permeability.

The same applies to the alteration of the mineral matrix of shales during heating. The exact changes occurring during heating are poorly studied. There are a number of mineral components in shales such as clays, carbonates, sulfides and others, which are affected by high temperatures [6]. It should be mentioned that the researchers have used quite a

narrow set of methods for investigations: micro-CT, pyrolysis and some visual observations, which do not allow evaluate alterations in mineral matrix.

New methods and advanced techniques should be implemented to investigate changes during high temperature treatment. Focused ion beam scanning electron microscopy may be used for better understanding of the void space structure of shales during heating. Using of Optical Scanning Technique [17] gives detailed information about thermal properties of a rock. And involvement of X-Ray diffraction method allows to assess alterations of mineral matrix composition (especially composition of clays, which are very sensitive to temperature changes).

There are still many open questions around the issue of shales alterations during heating such as pore space structure and mineral matrix composition. And a certain need for further investigation exists with implementation of advanced methods. These studies should be aimed to better understand and develop the ability to control the processes during high temperature treatment in order to enhance effectiveness of hydrocarbon recovery from organic-rich shales.

---

## V. REFERENCES

- [1] W. Chen, Y. Lei, "Experimental study of high temperature combustion for enhanced shale gas recovery," *Energ. Fuels*, vol. 31, no. 9, pp. 10003–10010, Aug. 2017.
- [2] G. Chapiro, J. Bruining, "Combustion enhance recovery of shale gas," *J. Petrol. Sci. Eng.*, vol.127, no. 3, pp. 179–189, Mar. 2015.
- [3] D. J. K. Ross, R. M. Bustin, "The importance of shale composition and 457 pore structure upon gas storage potential of shale gas reservoirs," *Mar. Petrol. Geol.*, vol. 26, pp. 916–927, Jun. 2009.
- [4] S. A. Holditch, "Unconventional oil and gas resource development – Let's do it right," *J. Unconven. Oil and Gas Resour.*, vol. 1–2, pp. 2–8, Jun. 2013.
- [5] T. Bondarenko, A. Cheremisin, E. Kozlova, I. Zvereva, "Experimental investigation of thermal decomposition of Bazhenov formation kerogen: Mechanism and application for thermal enhanced oil recovery," *J. Petrol. Sci. Eng.*, vol. 150, no. 2, pp. 288–296, Feb. 2017.
- [6] W. H. Somerton, "Thermal alteration," in *Thermal Properties and Temperature-Related Behavior of Rock/Fluid Systems*, 1st ed. New York: Elsevier Science, 1992, ch. IX, pp. 148–180.
- [7] P. R. Tisot, "Alterations in structure and physical properties of Green River oil shale by thermal treatment," *J. Chem. Eng. Data*, vol. 12, pp. 405–411, Jul. 1967.
- [8] M. Prats, "The thermal conductivity and diffusivity of Green River oil shales," *J. Petrol. Tech.*, vol. 27, no. 1, pp. 97–107, Jan. 1975.
- [9] P. Tiwari, M. D. Deo, C. L. Lin, J. D. Miller, "Characterization of oil shale pore structure before and after pyrolysis by using X-ray micro CT," *Fuel*, vol. 107, pp. 547–554, May 2013.
- [10] J. Zhao, D. Yang, "A micro-ct-study of changes in the internal structure of Daqing and Yan'an oil shales at high temperatures," *Oil Shales*, vol. 29, no. 4, pp. 357–367, Jan. 2012.
- [11] M. Kobchenko, H. Panahi, F. Renard, D. K. Dysthe, A. Malthe-Sørenssen, A. Mazzini, J. Scheibert, B. Jamtveit, P. Meakin, "4D imaging of fracturing in organic rich shales during heating," *J. Geophys. Res.: Solid Earth*, vol. 116, no. B12, pp. B12201, Dec. 2011.
- [12] T. Saif, Q. Lin, A.R Butcher, B. Bijeljic, "Multi-scale multidimensional microstructure imaging of oil shale pyrolysis using X-ray micro-tomography Automated ultra-high resolution SEM, MAPS Mineralogy and FIB-SEM," *Appl. Ener.*, vol. 202, pp. 628–647, Sep. 2017.
- [13] C. Ma, D. Elsworth, C. Dong, C. Lin, G. Luan, B. Chen, X. Liu, J. M. Muhammad, A. Z. Muhammad, Z. Shen, F. Tian, "Controls of hydrocarbon generation on the development of expulsion fractures in organicrich shale:

Based on the Paleogene Shahejie Formation in the Jiyang Depression, Bohai Bay Basin, East China," *Mar. Petrol. Geol.*, vol. 86, pp. 1406–1416, Sep. 2017.

- [14] M. G. Teixeira, F. Donzé, "Microfracturing during primary migration in shales," *Tectonophysics*, vol. 694, pp. 268–279, Jan. 2017.
- [15] T. M. Bondarenko, A. Z. Mukhametdinova, E. Popov, A. Cheremisin, "Analysis of changes in Bazhenov formation rock properties as a result of high-pressure air injection based on laboratory modelling data," *Oil Ind. J.*, vol. 2017, no. 3, pp. 40–44, Mar. 2017.
- [16] D. R. Gafurova, D. V. Korost, E. Kozlova, A. Kalmykov, "Pore space change of various lithotypes of the kerogen domanic rocks at different heating rates," *Georesursy*, vol. 19, no. 3, pp.225–263, Mar. 2017.
- [17] Y. Popov, G. Beardsmore, C. Clauser, S. Roy, "ISRM suggested methods for determining thermal properties of rocks from laboratory tests at atmospheric pressure," *Rock Mech. Rock Eng.*, vol. 49, no. 10, pp. 4179–4207, Oct. 2016.

---

# Overview of Protective Coatings for Cathode Materials for Li-ion Batteries

A. Shevtsov\*

---

## Abstract

High-energy cathodes suffer from significant capacity and voltage fade partially due to the surface degradation of the electrode. The core-shell concept relies on a protective layer that separates the active material from the electrolyte. This paper is an overview of different coating materials, their advantages/disadvantages and methods of their application.

---

## Index Terms

Capacity fade; cathode; core-shell; Li-ion battery; protective layer; voltage fade.

---

## I NOMENCLATURE

$c_p$	practical specific capacity ( $\text{mAhg}^{-1}$ )
$c_{th}$	theoretical specific capacity ( $\text{mAhg}^{-1}$ )
$U$	voltage (V)
$E$	energy density (W/kg)
$C$	current density ( $\text{mA}\text{g}^{-1}$ )

---

## II INTRODUCTION

**F**OR over two decades, lithium-ion batteries have been used in portable electronic devices and electric vehicles; now they are also considered for the stationary energy storage [1]-[3]. The end user always wants a cellphone or a laptop that works longer

---

\* A. Shevtsov is with the Center for Energy Science and Technology, Skolkovo Institute of Science and Technology, Skolkovo Innovation Center, Building 3, Moscow, 121205, Russia (e-mail: andrey.shevtsov@skolkovotech.ru).

and charges faster, thus the prerequisites for anodes and especially the cathodes have become increasingly strict over the years: more energy density, greater currents and slower degradation [4], [5]. To satisfy the demand, researchers all over the world try to synthesize new compounds, which would replace the graphite anode and the still dominating  $\text{LiCO}_2$  cathode.

Unfortunately, most high-energy materials suffer from low Coulombic efficiency and accumulative degradation, resulting in the capacity and voltage fade [6]. For these reasons, they can never be commercialized. Using chemistry and materials science scientists found ways to mitigate the decomposition processes: the structural deterioration, due to ionic migration in the core, can be somewhat limited by doping [7] and the surface phase transitions require protective coatings to limit the decay [8]-[11].

The use of core-shell structures for electrode materials has been known for a long time [12], yet the interest to the topic has only been increasing over the years, see Fig. 1.

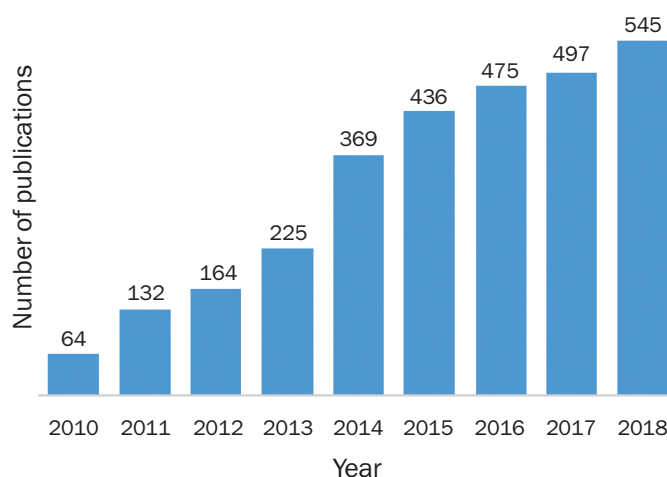


Fig. 1. Publications per year for “core-shell for batteries” between 2010 and 2018 generated by data collected from Web of Science® database.

The cathode stores the most of the electrochemical energy in a metal-ion battery and undergoes the surface decomposition first, thus finding new coatings, preventing that, would greatly improve the battery’s overall performance. This work is dedicated to the overview of different possible protective layers for cathode materials.

---

### III PROTECTIVE COATINGS

The surface treatment is viewed as a promising approach in limiting detrimental effects caused by the interaction between the electrode and the electrolyte at high potentials [8]-[12]. The core provides high capacity, and the shell increases the surface stability and conductivity of the core. The synthetic techniques used to obtain the core-shell are numerous and diverse. Among others, they include sol-gel route [13], chemical vapor deposition [14] and atomic layer deposition [15] for ultrathin nanocoatings, hydroxide and carbonate coprecipitation with evaporation for thick protective layers [16].



From a chemical standpoint, there are different possibilities in protecting cathode materials – the coatings may be differentiated depending on the applied compounds: inert oxides, carbon, fluorides, lithium containing oxides, electrolytes, inert phosphates, polymers, lithium borate glass (LBO), electrochemically active oxides and phosphates; or structural modifications: double layers and particles with a concentration gradient [9], [17]. Below we shall review some of them.

### A. Inert oxides

The coating of cathodes with inert oxides was the first type of physical separation of an electrode and the electrolyte [12]. The experimental data shows that doping with, for example, aluminum is an inferior technique to a protective coating of the oxide of the same cation,  $\text{Al}_2\text{O}_3$  [18], for  $\text{LiCoO}_2$ , although doping cobalt by 25% with an insulating ion seems excessive [19]. The initial capacity (170 to 125  $\text{mAhg}^{-1}$ ) and its retention (94 to 51%) are significantly better for the core-shell structure.

Other metal oxides such as  $\text{ZnO}$ ,  $\text{TiO}_2$ ,  $\text{ZrO}_2$  and  $\text{CeO}_2$  have also been used as coatings [20]-[23], despite these materials being poor electronic and Li-ion conductors. The oxide protective layer leads to increased ohmic losses that can only be mitigated by lowering its thickness [24]. Thus, the most used technique for these coatings is the atomic layer deposition (ALD) [22], [23], as it offers better control over the thickness of the applied layers compared to other methods. ALD is mostly confined to binary oxides ( $\text{MO}_x$ ); as otherwise, it requires the construction of dedicated reactors.

### B. Fluorides

The main attractive feature of fluorides lies in their inertness to HF formed as a by-product in electrolytes like  $\text{LiF}_6$  with trace of  $\text{H}_2\text{O}$  present. This autocatalytic reaction results in the formation of insulating LiF and the failure of the battery [25].

$\text{AlF}_3$  is the most common fluoride coating, also used to protect current collectors [9]. Among other compounds, it has been applied to various layered oxides such as,  $\text{LiCoO}_2$  [26], [27],  $\text{LiNi}_{0.5}\text{Co}_{0.2}\text{Mn}_{0.3}\text{O}_2$  [28],  $\text{LiNi}_{1/3}\text{Mn}_{1/3}\text{Co}_{1/3}\text{O}_2$  [29], [30],  $\text{Li}_{0.19}\text{Ni}_{0.16}\text{Co}_{0.08}\text{Mn}_{0.57}\text{O}_2$  [31] and  $\text{Li}[\text{Li}_{0.2}\text{Mn}_{0.54}\text{Ni}_{0.13}\text{Co}_{0.13}]\text{O}_2$  (Li-rich NMC) [32]. The application of aluminum fluoride is similar to all aforementioned works and involves a coprecipitation with subsequent evaporation of the solvent. The general idea is similar to that of inert oxides, a thin >10 nm layer of the insulating  $\text{AlF}_3$  has a positive impact on the electrochemical properties of the cathode.

There are also other possibilities for fluoride coatings:  $\text{MgF}_2$  [33],  $\text{LaF}_3$  [34],  $\text{LiF}$  [35] and  $\text{ZrF}_x$  [36]. They have the same effect as  $\text{AlF}_3$ , because they share the same electrochemical properties in regards of electric conductivity and reactivity with HF.

### C. Solid Electrolytes

A more advanced approach involves coating by applying lithium-containing oxides  $\text{LiTaO}_3$ ,  $\text{Li}_2\text{ZrO}_3$ ,  $\text{LiAlO}_2$  or  $\text{Li}_2\text{TiO}_3$  layers [37]-[40]. The overall idea is to make a protective layer to limit the interaction with the electrolyte, which would also be a conductor of  $\text{Li}^+$  ions.

The cycling stability and rate capability of the cathode at high voltages were improved with this type of surface coating. It was documented that 1 wt.%  $\text{Li}_2\text{ZrO}_3$  shell can stabilize the crystal structure of the core, decrease the oxygen loss, and improve the thermal stability of the electrode charged to 4.8 V [39]. Although it is a clear improvement over the binary oxide coating, the electric conductivity is still lackluster.  $\text{Li}_2\text{TiO}_3$  has a positive influence on the rate and cycling performance of the high-voltage  $\text{LiNi}_{0.5}\text{Mn}_{1.5}\text{O}_4$  spinel cathode material has been reported [41].

Li-conducting phosphates  $\text{Li}_3\text{PO}_4$ ,  $\text{Li}_4\text{P}_2\text{O}_7$ , and  $\text{AlPO}_4$  were also studied as coating materials for the high voltage spinel and layered cathodes [41]-[44]. They bring the same pros and cons as the oxide electrolytes. Recently, it has been shown that a simple deposition, ALD in this case, is not sufficient [45]. Particles are not ideal spheres – they have surface defects, thus the intergranular cracks also need to be coated, which requires an extra annealing step.

#### D. Cathode materials

Covering the active electrode material with an actual cathode (unlike in prior sections the material has reversible electrochemical activity) has many benefits: increased conducting properties, better stability versus the electrolyte at high voltages and less mechanical degradation of the shell due to the formation of voids [17]. The great challenge, however, is to make a homogeneous core-shell particle with heterogenic crystal phases. The best fitting candidates are already established and commercialized compounds: spinel oxides  $\text{LiM}_2\text{O}_4$ , layered oxides  $\text{LiMO}_2$  or phosphates  $\text{LiMPO}_4$ . They have all of the aforementioned advantages, besides their synthesis is well known and easy to reproduce.

Spinel  $\text{LiM}_2\text{O}_4$  has always been regarded as a promising cathode material thanks to its cheapness, low toxicity and easy preparation [46]. However, it has a serious drawback:  $\text{Mn}^{3+}$  ions undergo a disproportionation reaction, which results in the degradation of the material [47]. Thus, some of the manganese ions were replaced by  $\text{Ni}^{2+}$  to stabilize the crystallographic structure and form  $\text{LiMn}_{1.5}\text{Ni}_{0.5}\text{O}_4$ . This substituted spinel oxide shows significantly enhanced electrochemical properties and higher stability [46]. It is regarded as the reference spinel cathode.

It is surprising that several authors reported the use of just  $\text{LiMn}_2\text{O}_4$  as a protective layer for  $\text{LiCoO}_2$  [48],  $\text{LiNi}_{0.7}\text{Co}_{0.15}\text{Mn}_{0.15}\text{O}_2$  (Ni-rich NMC) [49] and Li-rich NMC [50], as this spinel oxide has a lower shell life compared all of them. For all three electrodes, the core-shell structure was synthesized using the coprecipitation of precursor hydroxides. The galvanostatic cycling shows improved capacity retention (around 80% for all three cores), but the Coulombic efficiency stays the same, which undermines the whole effort.

Although the choice of the coating is questionable, the manganese spinel is the easiest to synthesize, as  $\text{LiMn}_2\text{O}_4$  is a bimetallic system and  $\text{LiMn}_{1.5}\text{Ni}_{0.5}\text{O}_4$  is a trimetallic system. Thus, the substituted spinel is more difficult to obtain, and it is even more challenging to ensure its homogeneity. The obvious next step would be to synthesize a substituted spinel coating.

Attempts were made to stabilize the Li-rich spinel  $\text{Li}_{1.1}\text{Mn}_{1.9}\text{O}_4$  with  $\text{LiMn}_{1.5}\text{Ni}_{0.5}\text{O}_4$  [51]. The synthetic route consisted for the precipitation of a carbonate shell on the surface of the carbonate precursor. The resulting core-shell was cycled at 60° C in a higher voltage window between 3-5 V, compared to the pristine material, with a capacity retention of 95.6% for  $117 \text{ mAhg}^{-1}$ . It is curious that a higher voltage did not contribute to the degradation of the material, and that the electrochemical measurements were performed at elevated temperatures. The authors attribute their success to the thick coating, which protected the core from HF. No effect of the disproportionation reaction was reported. In addition, the lack of EDX analysis of the particles makes one wonder whether the nickel simply diffused in the spinel to form  $\text{Li}_{1.08}\text{Mn}_{1.8}\text{Ni}_{0.12}\text{O}_4$ , because the authors claim to have synthesized a Li-rich core and ordinary spinel shell, while the precursor core-shell consisted of heterogeneous carbonates.

The substituted Ni-rich  $\text{LiMO}_2$  layered oxides by design were supposed to replace  $\text{LiCoO}_2$ . The self-heating problem, the capacity and voltage fade, caused by the interlayer migration of  $\text{Ni}^{2+}$ , hinder the introduction of these materials to the market. There were multiple studies to limit the degradation using protective coatings [52]-[57]. The attraction lies in the similarity of the coated particle and the protective layer, which resolves issues like the volumetric change during charge/discharge or structural compatibility for ionic conductivity.

Amongst the first core-shells with a coating of a layered oxide consisted of  $\text{LiNi}_{0.5}\text{Mn}_{0.5}\text{O}_2$  on  $\text{LiNi}_{0.8}\text{Co}_{0.1}\text{Mn}_{0.1}\text{O}_2$  via the hydroxide coprecipitation route [52]. The galvanostatic measurements of the obtained material reveal a significantly improved capacity retention from 81 to 96% over 500 charge-discharge cycles with the current density of  $20 \text{ mA}g^{-1}$  (approx. C/5). The authors emphasized that the core material has a major impact on the overall energy density, whereas the surrounding shell mainly influences the capacity retention. The subsequent designs core-shell of cathode materials had the same coating, the same synthetic route and included  $\text{Li}[(\text{Ni}_{0.8}\text{Co}_{0.1}\text{Mn}_{0.1})_{1-x}(\text{Ni}_{0.5}\text{Mn}_{0.5})_x]\text{O}_2$  [53],  $\text{Li}[(\text{Ni}_{0.8}\text{Co}_{0.2})_{0.8}(\text{Ni}_{0.5}\text{Mn}_{0.5})_{0.2}]\text{O}_2$  [54], and  $\text{Li}[(\text{Ni}_{1/3}\text{Co}_{1/3}\text{Mn}_{1/3})_{0.8}(\text{Ni}_{1/2}\text{Mn}_{1/2})_{0.2}]\text{O}_2$  [55]. These core-shell cathode materials achieved significant improvements over the pristine component. Especially in the author's following works, it was shown that the coating has the same capacity retention as the core-shell, but lower capacity [55]; the core has the same initial capacity that the core-shell, but it fades faster (77 to 99%).

With the emergence of Ni-rich NMC attempts were made to stabilize its capacity:  $\text{Li}[(\text{Ni}_{0.8}\text{Co}_{0.15}\text{Al}_{0.05})_{0.8}(\text{Ni}_{0.5}\text{Mn}_{0.5})_{0.2}]\text{O}_2$  [56] and  $\text{Li}[(\text{Ni}_{0.8}\text{Co}_{0.1}\text{Mn}_{0.1})_{0.7}(\text{Ni}_{0.45}\text{Co}_{0.1}\text{Mn}_{0.45})_{0.3}]\text{O}_2$  [57].

The  $\text{LiNi}_{0.5}\text{Mn}_{0.5}\text{O}_2$  layered oxide is notorious to form  $\text{LiNi}_{0.5}\text{Mn}_{1.5}\text{O}_4$  on its surface [58]. Notably many studies did not take that in consideration, as this oxide is not the most suitable as a protective coating. Alas, the crystallographic examination of the cycled cathode electrode to determine the surface phase was not performed to prove or deny the hypothesis leaving room for speculation.

The olivine structured  $\text{LiMPO}_4$  cathodes were the first to benefit from the core-shell structure on an industrial scale, as they suffer from very low electric conductivity [59] and need a carbon coating to decrease the resistance. The  $\text{LiFePO}_4$  is the only commercialized phosphate cathode thanks to the resistance to high currents, good capacity and voltage

retention. Nevertheless, its low theoretical capacity and a working potential between 3.2-3.5 V vs  $\text{Li}^+/\text{Li}$  leave a lot to desire. Thus, less attractive phosphates, like the isomorph  $\text{LiMnPO}_4$  or  $\text{LiCoPO}_4$ , with even lower electric conductivity, but higher working potential of 4.1 V vs  $\text{Li}^+/\text{Li}$  were investigated [60], demonstrating very poor reversible capacity.  $\text{LiMnPO}_4$  also suffers from the disproportionation reaction of  $\text{Mn}^{3+}$  and, as a result, manganese ions may be washed out by the electrolyte.

A partially substituted lithium manganese phosphate  $\text{LiMn}_{0.85}\text{Fe}_{0.15}\text{PO}_4$  was coated with  $\text{LiFePO}_4$  and then with conducting carbon [61] via the coprecipitation route. Although, the electrodes were cycled at an elevated temperature  $60^\circ\text{C}$ , the second voltage plateau is at 4.1 V vs  $\text{Li}^+/\text{Li}$ . The working potential does not fade and the capacity retention of 97% (initial  $152\text{ mAhg}^{-1}$ ) vs 80% for the pristine material – this proves that the core-shell clearly has superior electrochemical properties, compared to the core. However, the shell does not solve the conductivity problems of the materials, and in this case, the use of doping may be better [62].

The lithium cobalt phosphate is notorious for its high capacity and surface degradation. The  $\text{LiCoPO}_4@ \text{LiFePO}_4$  core-shell was synthesized using the solvothermal method in the Anton Paar microwave reactor [63]. The resulting material is not interesting from an electrochemical standpoint, but the synthetic route is very appealing, as the Coulombic efficiency is low and the capacity retention is nonexistent. Nevertheless, considering the core is lithium cobalt phosphate – the result is impressive.

The  $\text{LiFePO}_4$  was also used as a coating for Ni-rich NMC [64]. The synthesis of the core-shell is unconventional, to say the least, as it was performed in a ball-mill. This was done before for a layered oxide with a limited success [65]. The problem of the mechano-activation synthesis is in the fact the layered structure of the core is fragile to the ball-mill, as, from personal experience, the layers lose uniform orientation and form a flower-like structure. Despite that, the authors showed increased capacity retention for 10% of  $\text{LiFePO}_4$  coating over 150 cycles. Another alarming feature: there is no mention of the carbon coating to increase the conductivity of the phosphate protective layer, which is relatively thick.

Regardless of the synthetic difficulties to obtain a heterogeneous core-shell structure, the phosphates are probably the most promising way to coat cathode materials, due to their chemical and mechanical properties.

---

## IV CONCLUSIONS

For the past three decades, the development of safe, cheap and powerful electrodes for Li-ion batteries was the main driving force in the field. The overviewed core-shell structures revealed a large variety of possible coating and synthetic routes to conceive new electrode materials. As a rule of thumb, these electrodes combine the high-energy density of the core, as well as the chemical inertness versus electrolyte and the electrochemical stability of the shell components.

The previously uninvestigated chemistry of the electrode-electrolyte interface plays an essential part in keeping a greater shelf life of the cathode materials. No longer scientists can investigate new compounds without considering the impact of the surface. The “ideal cathode” inert to electrolyte at high voltages, with high working potential and specific capacity may never be discovered, yet we are in need of materials that can provide more energy density and are resistant to higher currents at the same price. For these reasons, the development of the science of the particle architecture is primordial.

Each type of protective coating presents its advantages and disadvantages, see Table I. The inert oxides and fluorides are cheap, easy to deposit and are uniform (meaning, one does not need to research a specific shell for a different core – you can apply the same core to all materials). Yet, the poor ionic and electric conductivity is a major issue, as usually high voltage materials are poor conductors, thus covering their surface with an insulator is not helpful.

That is even more impactful for electrolytes, as by design they are insulators with a high voltage stability window. They are far more expensive and difficult to use as coatings. The volumetric changes of electrodes during cycling (not so impactful for amorphous binary systems) create voids on the core-shell interface, which significantly decrease the cathode’s efficiency. Despite all that, they almost completely prevent the catalytic surface activity of the cathode material vs the electrolyte, which diminishes the capacity and voltage fade.

TABLE I. Pros and cons of the reviewed types of protective coatings

<b>Coating type</b>	<b>Pros</b>	<b>Cons</b>
Inert oxides and fluorides	+ easy synthesis + cheap fabrication	- Poor electric and ionic conductors
Electrolytes	+ Fewer surface activity at high $V$	- Difficult synthesis - Strong insulators
Active cathodes $\text{LiM}_2\text{O}_4$ , $\text{LiMO}_2$ , $\text{LiMPO}_4$	+ Less voltage and capacity decay + Shell adhesion + No ionic washing + Ionic and electric conductivity	- Difficult synthesis - Expensive coating - No industrialized uniform method yet - Requires specific shell for each core

The approach of using an electroactive material on the surface of the cathode combines the benefits of both, inert oxides and electrolytes: the conductivity is not hindered and the capacity/voltage fade is strongly reduced. The appearance of voids on the interface is not as significant, if the volumetric variation of the core and the shell are compatible.

Yet this concept introduces many additional challenges. The synthetic routes vary from coating to coating and require a case-to-case attitude. The cost of production

also rises substantially, as the synthesis is more problematic and the shell chemicals are more expensive. Nevertheless, I believe that these problems are temporary and will be overcome eventually.

Currently, the active cathode coating field is dominated by core-shells with homogeneous crystal structure, meaning one would make a layered coating for a high-energy layered cathode. However, this approach greatly limits the possible core-shell combinations. Thus, new heterogeneous systems and combinations need to be researched.

To conclude, the core-shell field attracts a lot of attention both from academic and industrial researches. Unfortunately, the vast majority of scientific papers and patents are not on par with the imposed challenges. Many abuse the simplest tricks, as for example, not annealing the particles long enough to form a well-crystallized phase and after the thermal treatment with such coating they claim a miraculous improvement of the electrochemical properties. Editors and patent officers should be more wary of these issues.

---

## V ACKNOWLEDGMENT

The author gratefully acknowledges the contributions of prof. A.M. Abakumov and prof. E.V. Tikhomirova for their work on the original version of this document.

---

## VI REFERENCES

- [1] B. Dunn, H. Kamath, J.-M. Tarascon, "Electrical energy storage for the grid: a battery of choices," *Science*, vol. 334, no. 6058, pp. 928–935, Nov. 2011.
- [2] J. B. Goodenough, K.-S. Park, "The Li-ion rechargeable battery: a perspective," *J. Am. Chem. Soc.*, vol. 135, no. 4, pp. 1167–1176, Jan. 2013.
- [3] R. Marom, S. F. Amalraj, N. Leifer, D. Jacob, D. Aurbach, "A review of advanced and practical lithium battery materials," *J. Mater. Chem.*, vol. 21, no. 27, pp. 9938–9954, Jan. 2011.
- [4] V. Etacheri, R. Marom, R. Elazari, G. Salitra, D. Aurbach, "Challenges in the development of advanced Li-ion batteries: a review," *Energy Environ. Sci.*, vol. 4, no. 9, pp. 3243–3262, Jun. 2011.
- [5] J. Li, C. Daniel, D. Wood, "Materials processing for lithium-ion batteries," *J. Power Sources*, vol. 196, no. 5, pp. 2452–2460, Nov. 2010.
- [6] S. Hy, H. Liu, M. Zhang, D. Qian, B.-J. Hwang, Y. S. Meng, "Performance and design considerations for lithium excess layered oxide positive electrode materials for lithium-ion batteries," *Energy Environ. Sci.*, vol. 9, no. 6, pp. 1931–1954, Apr. 2016.
- [7] P. K. Nayak, J. Grinblat, M. Levi, E. Levi, S. Kim, J. W. Choi, D. Aurbach, "Al doping for mitigating the capacity fading and voltage decay of layered Li and Mn-rich cathodes for Li-ion batteries," *Adv. Ener. Mater.*, vol. 6, no. 8, 1502398, Feb. 2016.
- [8] K. T. Lee, S. Jeong, J. Cho, "Roles of surface chemistry on safety and electrochemistry in lithium-ion batteries," *Acc. Chem. Res.*, vol. 46, no. 5, pp. 1161–1170, Apr. 2012.
- [9] A. Mauger, C. Julien, "Surface modifications of electrode materials for lithium-ion batteries: status and trends," *Ionics*, vol. 20, no. 6, pp. 751–787, Mar. 2014.
- [10] O. Yuhong, S. Nam, S. Wi, S. Hong, B. Park, "Review paper: nanoscale interface control for high-performance Li-ion batteries," *Elect. Mater. Lett.*, vol. 8, no. 2, pp. 91–105, 2012.

- [11] G. Xu, Z. Liu, C. Zhang, G. Cui, L. Chen, "Strategies for improving the cyclability and thermo-stability of  $\text{LiMn}_2\text{O}_4$  - based batteries at elevated temperatures," *J. Mater. Chem. A*, vol. 3, no. 8, pp. 4092–4123, Nov. 2014.
- [12] I. Kuribayashi, M. Yokoyama, M. Yamashita, "Battery characteristics with various carbonaceous materials," *J. Power Sources*, vol. 54, no. 1, pp. 1–5, Mar. 1995.
- [13] W. Duan, Z. Hu, K. Zhang, F. Cheng, Z. Tao, J. Chen, " $\text{Li}_3\text{V}_2(\text{PO}_4)_3$ @C core-shell nanocomposite as a superior cathode material for lithium-ion batteries," *Nanoscale*, vol. 5, no. 14, pp. 6485–6490, May 2013.
- [14] R. Tian, H. Liu, Y. Jiang, J. Chen, X. Tan, G. Liu, L. Zhang, X. Gu, Y. Guo, H. Wang, L. Sun, W. Chu, "Drastically enhanced high-rate performance of carbon-coated  $\text{LiFePO}_4$  nanorods using a green chemical vapor deposition (CVD) method for lithium-ion battery: a selective carbon coating process," *ACS Appl. Mater. Interfaces*, vol. 7, no. 21, pp. 11377–11386, May 2015.
- [15] B. Ahmed, C. Xia, H. N. Alshareef, "Electrode surface engineering by atomic layer deposition: a promising pathway toward better energy storage," *Nano Today*, vol. 11, no. 2, pp. 250–271, Apr. 2016.
- [16] S.-T. Myung, H.-J. Noh, S.-J. Yoon, E.-J. Lee, Y.-K. Sun, "Progress in high-capacity core-shell cathode materials for rechargeable lithium batteries," *J. Phys. Chem. Lett.*, vol. 5, no. 4, pp. 671–679, Jan. 2014.
- [17] P. Hou, H. Zhang, Z. Zi, L. Zhang, X. Xu, "Core-shell and concentration gradient cathodes prepared via co-precipitation reaction for advanced lithium-ion batteries," *J. Mater. Chem. A*, vol. 5, no. 9, pp. 4254–4279, Jan. 2017.
- [18] J. Cho, Y. J. Kim, B. Park, "Novel  $\text{LiCoO}_2$  cathode material with  $\text{Al}_2\text{O}_3$  coating for a Li-ion cell," *Chem. Mater.*, vol. 12, no. 12, pp. 3788–3791, Nov. 2000.
- [19] Y. Jang, B. Huang, H. Wang, D. R. Sadoway, G. Ceder, Y. Chiang, H. Liu, H. Tamura, " $\text{LiAl}_y\text{Co}_{1-y}\text{O}_2$  (R-3m) intercalation electrode for rechargeable lithium batteries," *J. Electrochem. Soc.*, vol. 146, no. 3, pp. 862–868, Sep. 1999.
- [20] Y.-K. Suna, Y.-S. Lee, M. Yoshio, K. Amine, "Synthesis and electrochemical properties of ZnO-coated  $\text{LiNi}_{0.5}\text{Mn}_{1.5}\text{O}_4$  spinel as 5 V cathode material for lithium secondary batteries," *Electrochem. Solid-State Lett.*, vol. 5, no. 5, pp. A99–A102, Mar. 2002.
- [21] I. Bloom, L. Trahey, A. Abouimrane, I. Belharouak, X. Zhang, Q. Wu, W. Lu, D. P. Abraham, M. Bettge, J. W. Elam, X. Meng, A. K. Burrell, C. Ban, R. Tenent, J. Nanda, N. Dudney, "Effect of interface modifications on voltage fade in  $0.5\text{Li}_2\text{MnO}_3$ - $0.5\text{LiNi}_{0.375}\text{Mn}_{0.375}\text{Co}_{0.25}\text{O}_2$  cathode materials," *J. Power Sources*, vol. 249, pp. 509–514, Mar. 2014.
- [22] X. Meng, X.-Q. Yang, X. Sun, "Emerging applications of atomic layer deposition for lithium-ion battery studies," *Adv. Mater.*, vol. 24, no. 27, pp. 3589–3615, July 2012.
- [23] X. Wang, G. Yushin, "Chemical vapor deposition and atomic layer deposition for advanced lithium-ion batteries and supercapacitors," *Energy Environ. Sci.*, vol. 8, no. 7, pp. 1889–1904, May 2015.
- [24] M. Bettge, Y. Li, B. Sankaran, N. D. Rago, T. Spila, R. T. Haasch, I. Petrov, D. P. Abraham, "Improving high-capacity  $\text{Li}_{1.2}\text{Ni}_{0.15}\text{Mn}_{0.55}\text{Co}_{0.1}\text{O}_2$ -based lithium-ion cells by modifying the positive electrode with alumina," *J. Power Sources*, vol. 233, pp. 346–357, July 2013.
- [25] D. Aurbach, B. Markovsky, G. Salitra, E. Markevich, Y. Talyossef, M. Koltypin, L. Nazar, B. Ellis, D. Kovacheva, "Review on electrode–electrolyte solution interactions, related to cathode materials for Li-ion batteries," *J. Power Sources*, vol. 165, no. 2, pp. 491–499, Mar. 2007.
- [26] Y.-K. Sun, J.-M. Han, S.-T. Myung, S.-W. Lee, K. Amine, "Significant improvement of high voltage cycling behavior  $\text{AlF}_3$ -coated  $\text{LiCoO}_2$  cathode," *Electrochem. Commun.*, vol. 8, no. 5, pp. 821–826, May 2006.
- [27] Y.-K. Sun, S.-W. Cho, S.-T. Myung, K. Amine, J. Prakash, "Effect of  $\text{AlF}_3$  coating amount on high voltage cycling performance of  $\text{LiCoO}_2$ ," *Electrochim. Acta*, vol. 53, no. 2, pp. 1013–1019, Dec. 2007.
- [28] K. Yang, L.-Z. Fan, J. Guo, X. Qu, "Significant improvement of electrochemical properties of  $\text{AlF}_3$ -coated  $\text{LiNi}_{0.5}\text{Co}_{0.2}\text{Mn}_{0.3}\text{O}_2$  cathode materials," *Electrochim. Acta*, vol. 63, pp. 363–368, Feb. 2012.
- [29] K.-S. Lee, S.-T. Myung, D.-W. Kim, Y.-K. Sun, " $\text{AlF}_3$ -coated  $\text{LiCoO}_2$  and  $\text{Li}[\text{Ni}_{1/3}\text{Co}_{1/3}\text{Mn}_{1/3}]\text{O}_2$  blend composite cathode for lithium-ion batteries," *J. Power Sources*, vol. 196, no. 16, pp. 6974–6977, Aug. 2011.
- [30] B.-C. Park, H.-B. Kim, S.-T. Myung, K. Amine, I. Belharouak, S.-M. Lee, Y.-K. Sun, "Improvement of structural and electrochemical properties of  $\text{AlF}_3$ -coated  $\text{Li}[\text{Ni}_{1/3}\text{Co}_{1/3}\text{Mn}_{1/3}]\text{O}_2$  cathode materials on high voltage region," *J. Power Sources*, vol. 178, no. 2, pp. 826–831, Apr. 2008.
- [31] Y.-K. Sun, M.-J. Lee, C. S. Yoon, J. Hassoun, K. Amine, B. Scrosati, "The role of  $\text{AlF}_3$  coatings in improving electrochemical cycling of li-enriched nickel-manganese oxide electrodes for Li-ion batteries," *Adv. Mater.*, vol. 24, no. 9, pp. 1192–1196, Mar. 2012.
- [32] J. M. Zheng, Z. R. Zhang, X. B. Wu, Z. X. Dong, Z. Zhu, Y. Yang, "The effects of  $\text{AlF}_3$  coating on the performance of  $\text{Li}[\text{Li}_{0.2}\text{Mn}_{0.54}\text{Ni}_{0.13}\text{Co}_{0.13}]\text{O}_2$  positive electrode material for lithium-ion battery," *J. Electrochem. Soc.*, vol. 155, no. 10, pp. A775–A782, Jul. 2008.

- [33] H. J. Lee, Y. J. Park, "Interface characterization of MgF<sub>2</sub>-coated LiCoO<sub>2</sub> thin films," *Solid State Ionics*, vol. 230, pp. 86–91, Jan. 2013.
- [34] Z. Yang, Q. Qiao, W. Yang, "Improvement of structural and electrochemical properties of commercial LiCoO<sub>2</sub> by coating with LaF<sub>3</sub>," *Electrochim. Acta*, vol. 56, no. 13, pp. 4791–4796, May 2011.
- [35] D. Li, Y. Sasaki, K. Kobayakawa, H. Noguchi, Y. Sato, "Preparation, morphology and electrochemical characteristics of LiNi<sub>1/3</sub>Mn<sub>1/3</sub>Co<sub>1/3</sub>O<sub>2</sub> with LiF addition," *Electrochim. Acta*, vol. 52, no. 2, pp. 643–648, Oct. 2006.
- [36] S. H. Yun, K.-S. Park, Y. J. Park, "The electrochemical property of ZrFx-coated Li[Ni<sub>1/3</sub>Co<sub>1/3</sub>Mn<sub>1/3</sub>]O<sub>2</sub> cathode material," *J. Power Sources*, vol. 195, no. 18, pp. 6108–6115, Sept. 2010.
- [37] X. Li, J. Liu, M. N. Banis, A. Lushington, R. Li, M. Cai, X. Sun, "Atomic layer deposition of solid-state electrolyte coated cathode materials with superior high-voltage cycling behavior for lithium-ion battery application," *Energy Environ. Sci.*, vol. 7, no. 2, pp. 768–778, Nov. 2014.
- [38] X. Zhang, S. Sun, Qi. Wu, N. Wan, D. Pan, Y. Bai, "Improved electrochemical and thermal performances of layered Li[Li<sub>0.2</sub>Ni<sub>0.17</sub>Co<sub>0.07</sub>Mn<sub>0.56</sub>]O<sub>2</sub> via Li<sub>2</sub>ZrO<sub>3</sub> surface modification," *J. Power Sources*, vol. 282, pp. 378–384, May 2015.
- [39] J. Liu, X. Sun, "Elegant design of electrode and electrode/electrolyte interface in lithium-ion batteries by atomic layer deposition," *Nanotechnology*, vol. 26, no. 2, 024001, Dec. 2014.
- [40] H. Deng, P. Nie, H. Luo, Y. Zhang, J. Wang, X. Zhang, "Highly enhanced lithium storage capability of LiNi<sub>0.5</sub>Mn<sub>1.5</sub>O<sub>4</sub> by coating with Li<sub>2</sub>TiO<sub>3</sub> for Li-ion batteries," *J. Mater. Chem. A.*, vol. 2, no. 43, pp. 18256–18262, Sept. 2014.
- [41] J. Chong, S. Xun, X. Song, G. Liu, V. S. Battaglia, "Surface stabilized LiNi<sub>0.5</sub>Mn<sub>1.5</sub>O<sub>4</sub> cathode materials with high-rate capability and long cycle life for lithium-ion batteries," *Nano Energy*, vol. 2, no. 2, pp. 283–293, Mar. 2012.
- [42] J. Chong, S. Xun, J. Zhang, X. Song, H. Xie, V. Battaglia, R. Wang, "Li<sub>3</sub>PO<sub>4</sub>-coated LiNi<sub>0.5</sub>Mn<sub>1.5</sub>O<sub>4</sub>: a stable high-voltage cathode material for lithium-ion batteries," *Chem. Eur. J.*, vol. 20, no. 24, pp. 7479–7485, Apr. 2014.
- [43] S. K. Martha, J. Nanda, Y. Kim, R. R. Unocic, S. Pannala, N. J. Dudney, "Solid electrolyte coated high voltage layered-layered lithium-rich composite cathode: Li<sub>1.2</sub>Mn<sub>0.525</sub>Ni<sub>0.175</sub>Co<sub>0.1</sub>O<sub>2</sub>," *J. Mater. Chem. A*, vol. 1, no. 18, pp. 5587–5595, Feb. 2013.
- [44] J. Cho, H. Kim, B. Park, "Comparison of overcharge behavior of AlPO<sub>4</sub>-coated LiCoO<sub>2</sub> and LiNi<sub>0.8</sub>Co<sub>0.1</sub>Mn<sub>0.1</sub>O<sub>2</sub> cathode materials in Li-ion cells," *J. Electrochem. Soc.*, vol. 151, no. 10, pp. A1707–A1711, Sept. 2004.
- [45] P. Yan, J. Zheng, J. Q. Liu, B. Wang, X. Cheng, Y. Zhang, X. Sun, C. Wang, J.-G. Zhang, "Tailoring grain boundary structures and chemistry of Ni-rich layered cathodes for enhanced cycle stability of lithium-ion batteries," *Nature Energy*, vol. 3, pp. 600–605, Jul. 2018.
- [46] D. Liu, W. Zhu, J. Trottier, C. Gagnon, F. Barry, A. Guerfi, A. Mauger, H. Groult, C. M. Julien, J. B. Goodenough, K. Zaghib, "Spinel materials for high-voltage cathodes in Li-ion batteries," *RCS Adv.*, vol. 4, pp. 154–167, Nov. 2013.
- [47] I. N. S. Jackson, R. C. Liebermann, A. E. Ringwoodl, "Disproportionation of spinels to mixed oxides: significance of cation configuration and implications for the mantle," *Earth and Planetary Sci. Lett.*, vol. 24, no. 2, pp. 203–208, Dec. 1974.
- [48] J. Cho, G. Kim, "Enhancement of thermal stability of LiCoO<sub>2</sub> by LiMn<sub>2</sub>O<sub>4</sub> coating," *Electrochem. Solid-State Lett.*, vol. 2, no. 6, pp. 253–255, Mar. 1999.
- [49] Y. Cho, S. Lee, Y. Lee, T. Hong, J. Cho, "Spinel-layered core-shell cathode materials for Li-ion batteries," *Adv. Energy Mater.*, vol. 1, no. 5, pp. 821–828, Jul. 2011.
- [50] F. Wu, N. Li, Y. Su, L. Zhang, L. Bao, J. Wang, L. Chen, Y. Zheng, L. Dai, J. Peng, S. Chen, "Ultrathin spinel membrane-encapsulated layered lithium-rich cathode material for advanced Li-ion batteries," *Nano Lett.*, vol. 14, no. 6, pp. 3550–3555, May 2014.
- [51] S.-T. Myung, K.-S. Lee, D.-W. Kim, B. Scrosati, Y.-K. Sun, "Spherical core-shell Li[(Li<sub>0.05</sub>Mn<sub>0.95</sub>)<sub>0.8</sub>(Ni<sub>0.25</sub>Mn<sub>0.75</sub>)<sub>0.2</sub>]O<sub>4</sub> spinels as high performance cathodes for lithium batteries," *Energy Environ. Sci.*, vol. 4, no. 3, pp. 935–939, Nov. 2010.
- [52] Y.-K. Sun, S.-T. Myung, M.-H. Kim, J. Prakash, K. Amine, "Synthesis and characterization of Li[(Ni<sub>0.8</sub>Co<sub>0.1</sub>Mn<sub>0.1</sub>)<sub>0.8</sub>(Ni<sub>0.5</sub>Mn<sub>0.5</sub>)<sub>0.2</sub>]O<sub>2</sub> with the microscale core-shell structure as the positive electrode material for lithium batteries," *J. Am. Chem. Soc.*, vol. 127, no. 38, pp. 13411–13418, June 2005.
- [53] Y.-K. Sun, S.-T. Myung, B.-C. Park, K. Amine, "Synthesis of spherical nano- to microscale core-shell particles Li[(Ni<sub>0.8</sub>Co<sub>0.1</sub>Mn<sub>0.1</sub>)<sub>1-x</sub>(Ni<sub>0.5</sub>Mn<sub>0.5</sub>)<sub>x</sub>]O<sub>2</sub> and their applications to lithium batteries," *Chem. Mater.*, vol. 18, no. 22, pp. 5159–5163, Oct. 2006.



- [54] Y.-K. Sun, S.-T. Myung, H.-S. Shin, Y. C. Bae, C. S. Yoon, "Novel core-shell-structured  $\text{Li}[(\text{Ni}_{0.8}\text{Co}_{0.2})_{0.8}(\text{Ni}_{0.5}\text{Mn}_{0.5})_{0.2}]\text{O}_2$  via coprecipitation as positive electrode material for lithium secondary batteries," *J. Phys. Chem. B*, vol. 110, no. 13, pp. 6810–6815, Mar. 2006.
- [55] K.-S. Lee, S.-T. Myung, Y.-K. Sun, "Synthesis and electrochemical performances of core-shell structured  $\text{Li}[(\text{Ni}_{1/3}\text{Co}_{1/3}\text{Mn}_{1/3})_{0.8}(\text{Ni}_{1/2}\text{Mn}_{1/2})_{0.2}]\text{O}_2$  cathode material for lithium ion batteries," *J. Power Sources*, vol. 195, no. 18, pp. 6043–6048, Sept. 2010.
- [56] J.-H. Ju, K.-S. Ryu, "Synthesis and electrochemical performance of  $\text{Li}(\text{Ni}_{0.8}\text{Co}_{0.15}\text{Al}_{0.05})_{0.8}(\text{Ni}_{0.5}\text{Mn}_{0.5})_{0.2}\text{O}_2$  with core-shell structure as cathode material for Li-ion batteries," *J. Alloys Compd.*, vol. 509, no. 30, pp. 7985–7992, July 2011.
- [57] H. Shi, X. Wang, P. Hou, E. Zhou, J. Guo, J. Zhang, D. Wang, F. Guo, D. Song, X. Shi, L. Zhang, "Core-shell structured  $\text{Li}[(\text{Ni}_{0.8}\text{Co}_{0.1}\text{Mn}_{0.1})_{0.7}(\text{Ni}_{0.45}\text{Co}_{0.1}\text{Mn}_{0.45})_{0.3}]\text{O}_2$  cathode material for high-energy lithium ion batteries," *J. Alloys Compd.*, vol. 587, pp. 710–716, Feb. 2014.
- [58] M. S. Islam, R. A. Davies, J. D. Gale, "Structural and electronic properties of the layered  $\text{LiNi}_{0.5}\text{Mn}_{0.5}\text{O}_2$  lithium battery material," *Chem. Mater.*, vol. 15, no. 22, pp. 4280–4286, Oct. 2009.
- [59] Z. Cheng, R. J. Dahn, "Reducing carbon in  $\text{LiFePO}_4/\text{C}$  composite electrodes to maximize specific energy, volumetric energy, and tap density," *J. Electrochem. Soc.*, vol. 149, no. 9, pp. 1184–1189, Jul 2002.
- [60] L. J. Hu, B. Qiu, Y. Xia, Z. Qin, L. Qin, X. Zhou, Z. Liu, "Solvochemical synthesis of Fe-doping  $\text{LiMnPO}_4$  nanomaterials for Li-ion batteries," *J. Power Sources*, vol. 248, no. 7, pp. 246–252, Apr. 2014.
- [61] S.-M. Oh, S.-T. Myung, J. B. Park, B. Scrosati, K. Amine, Y.-K. Sun, "Double-structured  $\text{LiMn}_{0.85}\text{Fe}_{0.15}\text{PO}_4$  coordinated with  $\text{LiFePO}_4$  for rechargeable lithium batteries," *Angew. Chem., Int. Ed.*, vol. 124, no. 8, pp. 1889–1892, Jan. 2012.
- [62] O. A. Drozhzhin, V. D. Sumanov, O. M. Karakulina, A. M. Abakumov, J. Hadermann, A. N. Baranov, K. J. Stevenson, E. V. Antipov, "Switching between solid solution and two-phase regimes in the  $\text{Li}_{1-x}\text{Fe}_{1-y}\text{Mn}_y\text{PO}_4$  cathode materials during lithium (de)insertion: combined PITT, in situ XRPD and electron diffraction tomography study," *Electrochim. Acta*, vol. 191, no. 10, pp. 149–157, Feb. 2016.
- [63] K. J. Kreder, A. Manthiram, "Vanadium-substituted  $\text{LiCoPO}_4$  core with a monolithic  $\text{LiFePO}_4$  shell for high-voltage lithium-ion batteries," *ACS Energy Lett.*, vol. 2, no. 1, pp. 64–69, Jan, 2017.
- [64] Z. Wu, S. Ji, T. Liu, Y. Duan, S. Xiao, Y. Lin, K. Xu, F. Pan, "Aligned  $\text{Li}^+$  tunnels in core-shell  $\text{Li}(\text{Ni}_x\text{Mn}_y\text{Co}_z)\text{O}_2@ \text{LiFePO}_4$  enhances its high voltage cycling stability as Li-ion battery cathode," *Nano Lett.*, vol. 16, no. 10, pp. 6357–6363, Sept. 2016.
- [65] W.-S. Kim, S.-B. Kim, I. C. Jang, H. H. Limb, Y. S. Lee, "Remarkable improvement in cell safety for  $\text{Li}[\text{Ni}_{0.5}\text{Co}_{0.2}\text{Mn}_{0.3}]\text{O}_2$  coated with  $\text{LiFePO}_4$ ," *J. Alloys Compd.*, vol. 492, no. 1–2, pp. L87–L90, Mar. 2010.

---

# Concepts of Commercial and Patented Smart Indoor Microclimate Control Solutions: A review

Arseniy A. Sleptsov\*

---

## Abstract

Energy performance of life-support systems in buildings is a subject undergoing an intense study. One must find a trade-off between indoor air quality and thermal comfort, and energy consumption of the systems supporting requested and required parameters of healthy indoor climate. Proper management of these systems helps to effectively operate them. Existing reviews on life-support systems in buildings focus on specific control methods. The aim of this paper is to reveal the gap between theoretical knowledge and application of the existing commercial and patented solutions. The review consists of analysis of related research, background of the technology and subject matter, outcomes of product profiles and patents search. The review shows the summarized concepts of the commercial and patented approaches. It also discusses the barriers of converting theoretical knowledge on subject matter into practice.

---

## Index Terms

Energy efficiency; heating, ventilation, air-conditioning (HVAC) systems; HVAC systems control; indoor air quality; intelligent control strategy; microclimate; smart control; sensors; thermostats; thermal comfort.

---

## I INTRODUCTION

**A**IR quality and thermal comfort are important aspects of indoor environment, and the Internet of Things (IoT) offers technical solutions to control and manage these parameters. Inhabitants use smart devices to reach the desired air quality and temperature level to achieve indoor comfort, while trying to optimize energy consumption. Thus, a gen-

---

\* **A. A. Sleptsov** is with the Center for Energy Science and Technology, Skolkovo Institute of Science and Technology, Skolkovo Innovation Center, Building 3, Moscow, 121205, Russia (e-mail: arseniy.sleptsov@skoltech.ru).

uinely smart approach is when buildings energy efficiency can be achieved by (i) hardware controllers that optimize the devices consumption keeping the prescribed set point; and (ii) operating algorithms managing the set points for all the devices in the loop based on optimality objectives.

The scientific and engineering communities are increasingly interested in the improvement of building heating, ventilation and air-conditioning (HVAC) systems responsible for indoor climate to make it more responsive/adaptive to the inhabitant's behavior, energy efficient and ecologically friendly.

Moreover, an improved HVAC systems control enables integration of distributed renewable energy generation which may broaden the role of buildings in the power and heat market, e.g. private solar panels and collectors generating power and heat may be controlled with HVAC systems energy demand. Positioning buildings as prosumers of smart grids and smart district heating networks adds substantial value to building energy consumption control and monitoring.

Outcomes of these investigations open new possibilities for the building sector, smart grids and district heating systems, smart cities, IoT and the HVAC.

In this paper, Section II provides the background by introducing indoor microclimate parameters; heating, ventilation and air-conditioning systems; control of such systems. Section III introduces the methodology applied to produce this review. Sections IV and V generalize the analyses of the surveying results. Section VI discusses barriers and future research challenges found in this research. Conclusions follow.

---

## II BACKGROUND

### A. Related reviews

There is a considerable literature on home life-support systems control. Song et al. in their review [1] pointed at the difficulties to build a detailed system and building model and to convert theory into application; and at the future perspectives on HVAC control systems: an integration of conventional and advanced control approaches, more precise human behavior detection, self-learning and modifying ability of controllers. Afram and Janabi-Sharifi compared various control methods with an emphasis on theory and applications of model predictive control (MPC) [2]. Belic et al. also accentuated predictive models for control purposes and acknowledged good results of such controllers. As the next step of development, they proposed making these controllers commercially available [3]. However, complexity of models development is the main challenge for practical application of MPC. Afroz et al. highlighted shortcomings generated from assumptions, unmeasured disturbances or uncertainties in some system properties [4]. Mirakhorli and Dong concluded that there is a need in a reliable baseline model, a more comprehensive and accurate occupancy behavior model, as well as a trade-off between complexity and performance. These were the takeaways from their review on occupancy based MPC [5].

These reviews pay attention to the importance of occupancy and occupants behavior besides control parameters. Shen et al. reviewed implicit occupancy sensing data streams. They acknowledge that the development of these technologies is on an early stage [6]. The data stream channels form the bridge between smart control and indoor environment quality. The related reviews analysis shows the lack of awareness of existing solutions reduced to practice. Therefore, there is a necessity to focus on commercialized and patented solutions concepts.

### **B. Indoor air quality and occupants' thermal comfort**

Thermal comfort and Indoor Air Quality (IAQ), mostly referred to as indoor microclimate, are part of indoor environment quality [7]. Thermal comfort, depending on human metabolic rate and clothing insulation, can be influenced by air temperature, mean radiant temperature, air velocity, and water vapor pressure. The IAQ is assessed basing on concentrations of contaminants [8] and carbon dioxide as well as humidity [9]. There are national standards and codes of practices [10], [11], building microclimate parameters must meet compliance, e.g. ASHRAE [12], REHVA [13]. These organizations propose rules and regulations related to comfort zones of indoor microclimate both to construction companies and facility providers. Other organizations such as LEED [14], BREAM [15], DNGB System [16] consult construction companies to meet pre-requisites listed in standards and award their certifications of compliance.

To meet a comfort level of these two main components of indoor environment quality, various systems were developed.

### **C. Heating, ventilation and air-conditioning systems**

Every building, flat, or room has a set of facilities, i.e. life-support system (LSS), which keeps each premise microclimate parameters within the defined boundaries. Figure 1 shows a modular set of units which may be available in a built environment: space heating unit (1), space cooling unit (2), air handling unit (3), air humidifier (4), automatic window opening/closing driver (5), internal (6) and external (7) shading devices, air purifier (8).

The basic set installed in almost all buildings is the set consisting of heating, ventilation, air-conditioning systems (1-3). Other units (4-8) are optional supplements to a home life-support system. The implementation of these facilities enhances occupants comfort, increases the cost of the building, and diversifies market opportunities, expanding functions and features of home LSS. However, with the complexity of the developed system, its management tangles, and operational cost increases.

The set of units responsible for microclimate control varies with the type of building. An ordinary flat or a residential single-family house may have only a heating unit, while a luxury brand-new building can be stuffed with a variety of listed units. Multi-family apartment buildings and commercial office buildings have centralized HVAC systems containing all the functions of heating, ventilation, air-conditioning, (de)-humidification, and air-filtration.

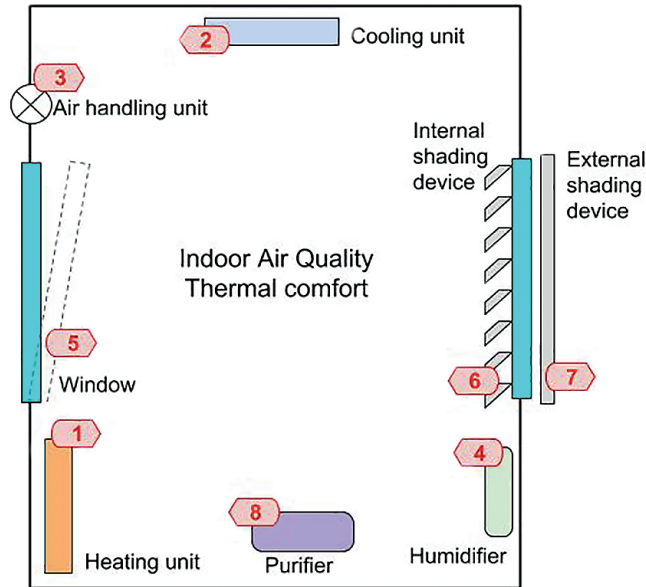


Fig. 1. Units influencing indoor microclimate parameters.

#### D. Indoor microclimate control

Each component or set of components of home life-support system has inbuilt controllers getting input signals from sensors or other communicating indicators and sending actions to the actuators of the components.

In most of the cases units (5-8) work independently. Other units (3-4) can be bundled into one system. For instance, an individual heat distribution and metering station of the building controls temperature in heat exchangers of ventilation and heating systems providing indirectly right temperature of supply air and demanded heat rate to keep room temperature within comfort zone respectively. The ventilation system contains at least components for air cooling, heating, and humidifying which have controllers working under cooperative framework of satisfying pre-requisites of supplied air quality.

With the emergence of such technologies there are expanding challenges to implement communication between components bearing different functions and to optimize their mutual operation constrained by the size of the bill.

### III METHODOLOGY

This review analyzes available commercial and patented solutions on indoor microclimate control; demonstrates customer value proposition, stakeholders, technological concepts of the solutions. It helps to understand gaps between academic research and industrial application. It shows the state of the art of implemented research findings.

#### A. Analysis of existing solutions web-pages

The analysis of technological concepts and customer value proposition of the solutions was performed surfing through web-pages of companies and startups solv-

ing microclimate control problem. Existing solutions are products of both small and big players [17]-[26].

## B. Patent search

Patents search was done using commercial web-based tool Cipher [27] which allows to create patents' classifier. The classifier was developed basing on over 150 patents abstracts' analyses. During the review patents were assessed as:

- Positive – if a patent corresponds to the technology of the research;
- Negative – if a patent does not correspond to the technology of the research;
- Ignored – if a patent cannot be classified as negative or positive.

In the process of building the classifier, the tactic of searching patents which conform to the described technology was changing. The following key words were used during the searching stages:

- “smart climate control”
- smart AND (climate OR temperature) AND control
- (smart OR intelligent) AND (climate OR temperature) AND control
- (smart OR intelligent OR “model predictive”) AND (climate OR temperature) AND control
- (smart OR intelligent OR predictive OR learning) AND (climate OR temperature OR environment) AND control
- (smart OR intelligent OR predictive OR learning) AND (climate OR temperature OR environment) AND control AND HVAC
- (smart OR intelligent OR learning OR predictive OR data) AND control AND (climate OR temperature OR environment) AND (heating OR ventilation OR air OR conditioning OR HVAC)

---

## IV COMMERCIAL INDOOR MICROCLIMATE CONTROL SOLUTIONS

The majority of technologies of microclimate control available in the market is connected with sensors of HVAC systems. These sensors send signals to the controllers installed in each unit of the system, enable communication between components and the environment. This solution exists as a baseline of each home life-support system.

We set three development steps towards “smart” home concept in the field of “smart” microclimate control technologies. The first step is expanding these sensors with human feedback channels. This solution is implemented in a form of active interaction with an occupant allowing him/her to schedule, change, remotely control and monitor the set values of microclimate parameters, e.g. temperature, humidity, and air quality. The second upgrade is expanding functions in the previous step with additional features such as geofencing,

alarming, integration with other smart home partners, unifying all controllable devices into one platform. The third development stage is the data collection. It enables to report energy performance, suggest system operation schedules to reduce the bill, automatically maintain the system basing on learned occupants and system behaviors. Moreover, the last stage of improvement includes feedback from the system to the occupants to change their behavior toward energy conservation and carbon footprint reduction sakes.

From the analysis of customer value proposition of the companies/startups providing such technologies, the main features making the technology “smart” are remote control and monitoring, scheduling and scenario setting, local weather flexibility, voice control and integration to other smart appliances such as Amazon Alexa, home & away mode powered by geofencing, etc. Rewards of such technologies leveraging market strategy are the bill reduction for home utilities through energy saving, consequently climate change mitigation; air quality improvement towards well-being and healthy lifestyle trends; ergonomics, user-friendly interface, the design of the communicating channel, e.g. thermostat, fitting to the interior of most homes.

---

## V PATENTS ON MICROCLIMATE CONTROL

The built classifier was used to find patents on invention in the field of microclimate control. We used the following key words for the searching strategy:

- (“climate control” OR “temperature control”) AND (room OR building OR household OR indoor) AND (intelligent OR smart OR predictive).

The following key words of the reviewed technology patents selected by the classifier were found: temperature control, wireless communication module, air-conditioning, energy saving, intelligent constant temperature, intelligent control system, control module.

In 2016 the activity of patent filing was the highest compared to the previous years and the last two coming years. In 2018 more than 370 patents were active, the estimated annual expenditure to obtain and maintain these patents was around \$583k.

Solutions described in the patents are specific approaches for a single component of entire HVAC system or other air quality and thermal comfort supporting facility. For instance, the infrastructure for “smart” control of heating system providing room thermal comfort, heat pump system providing each room set temperature, etc., are the patented solutions. The diversity of patents is driven by a variety of these components, multiplicity of communication infrastructure and its architecture, range of control hardware, design, and integration of multiple components. The importance of the invention is justified as CVPs of commercial products by energy saving, environment-friendliness, and user interface.

---

## VI DISCUSSION

There are a few barriers to control microclimate parameters in a smart and optimized way. The set of units ensuring IAQ and thermal comfort may be diverse depending on the need of the building and its occupants. Due to modularity of the developed facility and presence of inbuilt controllers in each component enables intervention only at communication channels level. This draws a potential of mutual platform investigation for better coordination of the components or ways of easy communication to make them work under cooperative framework.

There is a market of different market player producing certain components from the variety of the facility list. Hence, another challenge is to standardize components communication channels or to open control algorithms of these units for the third party which optimizes the operation of a group of systems.

The development of smart controllers' era has other fruitful benefits besides energy saving motivated by the climate change mitigation, bill reduction, indoor environment comfort maximization. The future energy networks require flexibility at the user side for minimization of a mismatch between energy generation and demand. A proper smarter control may suggest a number of advantages for the future energy grids.

---

## VII CONCLUSIONS

The degree of complexity of a control strategy labels a technology as smart system. We reviewed what HVAC systems control strategies are acknowledged to be smart studying concepts of commercial solutions implemented in real world cases, technologies and claims in the patents proposed by the trained patents' classifier. One of the findings is that the most commercial solutions are the thermostat enabling communication of a certain system with occupants. The technologies protected by intellectual property rights focus on specific solutions rather than on solutions integrating entire set of systems. Finally, we discussed the barriers and future challenges in the field of indoor microclimate control methods.

---

## VIII ACKNOWLEDGEMENTS

The author acknowledges Prof. Aldo Bischi, Prof. Elizaveta Tikhomirova, Prof. Alexei Buchachenko, Dr. Alexander Ryzhov and Dr. Anna Sharova for their support.



## IX REFERENCES

- [1] Y. Song, S. Wu, Y. Y. Yan, "Control strategies for indoor environment quality and energy efficiency – a review," *Int. J. Low-Carbon Technol.*, vol. 10, pp. 305–312, 2015.
- [2] A. Afram, F. Janabi-Sharifi, "Theory and applications of HVAC control systems – A review of model predictive control (MPC)," *Build. Environ.*, vol. 72, pp. 343–355, 2014.
- [3] F. Belic, "HVAC control methods – A review," in 2015 19th Int. Conf. *Syst. Theory, Control Comput.*, pp. 679–686, 2015.
- [4] Z. Afroz, G. M. Sha, T. Urmee, G. Higgins, "Modeling techniques used in building HVAC control systems: A review," *Renew. Sust. Energ. Rev.*, vol. 83, pp. 64–84, 2018.
- [5] A. Mirakhorli, B. Dong, "Occupancy behavior based model predictive control for building indoor climate – A critical review," *Energy Build.*, vol. 129, pp. 499–513, 2016.
- [6] W. Shen, G. Newsham, B. Gunay, "Advanced Engineering Informatics Leveraging existing occupancy-related data for optimal control of commercial office buildings: A review," *Adv. Eng. Informatics*, vol. 33, pp. 230–242, 2017.
- [7] USGBC, "Green Building 101: What is indoor environmental quality?," *Green Building 101*, 2014. [Online]. Available: <https://www.usgbc.org/articles/green-building-101-what-indoor-environmental-quality>. [Accessed: 21-Mar-2019].
- [8] R. M. S. F. Almeida, J. M. P. Q. de Freitas, Vasco Peixoto, Delgado, "Chapter 2: Indoor Environmental Quality," in *School Buildings Rehabilitation*, Springer, Cham, 2015.
- [9] R. H. Armon, O. Hanninen, Eds., *Environmental Indicators*. Springer Netherlands, 2015.
- [10] Госстрой России, "Строительные нормы и правила Российской Федерации. Тепловая защита зданий (Construction Rules and Regulations.375Thermal Performance of the Building)," СП 50.13330.2010., 2004. [Online]. Available: <http://docs.cntd.ru/document/1200035109>. [Accessed: 21-Mar-2019].
- [11] Госстрой России, "Строительные нормы и правила Российской Федерации. Отопление, вентиляция и кондиционирование (Construction Rules and Regulations. Heating, ventilation and air-conditioning)," СП 60.13330.2010, 2004. [Online]. Available: <http://docs.cntd.ru/document/1200035579>. [Accessed: 21-Mar-2019].
- [12] "The American Society of Heating, Refrigerating and Air-Conditioning Engineers." [Online]. Available: <https://www.ashrae.org>. [Accessed: 21-Mar-2019].
- [13] "The Federation of European Heating, Ventilation and Air Conditioning Associations." [Online]. Available: <https://www.rehva.eu/>. [Accessed: 21-Mar-2019].
- [14] "USGC LEED." [Online]. Available: <https://new.usgbc.org/leed>. [Accessed: 21-Mar-2019].
- [15] "BREEAM." [Online]. Available: <https://www.breeam.com/>. [Accessed: 21-Mar-2019].
- [16] "DNGB System." [Online]. Available: [https://www.dgnb-system.de/en/system/certification\\_system/index.php](https://www.dgnb-system.de/en/system/certification_system/index.php). [Accessed: 21-Mar-2019].
- [17] "TION: MagicAir." [Online]. Available: <https://tion.ru/product/magicair/>. [Accessed: 21-Mar-2019].
- [18] "Rubetek." [Online]. Available: <https://rubetek.com/products>. [Accessed: 21-Mar-2019].
- [19] "Siemens: Smart Thermostat." [Online]. Available: <https://new.siemens.com/global/en/products/buildings/topics/smart-thermostat.html>. [Accessed: 21-Mar-2019].
- [20] "Lux GEO." [Online]. Available: <https://www.luxproducts.com/geo/>. [Accessed: 21-Mar-2019].
- [21] "iDevices." [Online]. Available: <https://store.iddevicesinc.com/iddevices-thermostat/>. [Accessed: 21-Mar-2019].
- [22] "Honeywell Lyric T5." [Online]. Available: <https://www.honeywellhome.com/statichtml/lyric-t5-wi-fi.html>. [Accessed: 21-Mar-2019].
- [23] "Emerson: Sensi." [Online]. Available: <https://sensi.emerson.com/en-us/products/touch-thermostat>. [Accessed: 21-Mar-2019].
- [24] "ecobee." [Online]. Available: <https://www.ecobee.com/ecobee4/>. [Accessed: 21-Mar-2019].
- [25] "Johnson Controls: GLAS." [Online]. Available: <https://glas.johnsoncontrols.com/#>. [Accessed: 21-Mar-2019].
- [26] "Nest Thermostat." [Online]. Available: <https://nest.com/thermostats/>. [Accessed: 21-Mar-2019].
- [27] "CIPHER." [Online]. Available: <https://app.cipher.ai/>. [Accessed: 24-Mar-2019].

$\frac{2(n-m)^2}{m^2n^2} \cdot \frac{2(n-m)^2}{m^2n^2} \cdot \frac{m^2n^2}{mn} = mn \cdot 4 = \frac{4mn}{m^2n^2}$   
 $10(x-2)^2 - 9(y-3)^2 = 144 \Rightarrow \frac{(x-2)^2}{9} - \frac{(y-3)^2}{16} = 1 \quad e = \frac{c}{a}$   
 $2(n-m)^2 \cdot \frac{(m-n)^2}{2mn} \cdot \frac{54}{-18} \quad \frac{2(n-m)^2 \cdot (m^2-n)(m+n)}{m^2n^2 \cdot 2mn} \quad \begin{matrix} c=3 \\ a=2 \end{matrix}$   
 $g(\sqrt{y-\frac{54}{18}})^2 - (y-3)^2 = 16(x-2)^2$   
 $y-161=0 \quad 5) \frac{2(n-m)^2}{m^2n^2} \cdot \frac{(m-n)^2}{2mn} \cdot \frac{54}{-18}$   
 $S = -5k \cdot b$   
 $AD \perp CB \quad \begin{cases} 5 = -k \cdot 5 + b \\ 1 = k \cdot 3 + b \end{cases} \Leftrightarrow \begin{cases} 5 = -5k + b \\ 1 = 3k + b \end{cases}$   
 $2-54y-161=0 \quad 5 = -5k + b$   
 $\frac{(n^2-m^2)}{m^2n^2} - \frac{4mn}{m^2n^2} \quad A_1 A_2 A_3 \quad \begin{cases} -5k + b = 5 \\ 3k + b = 1 \end{cases}$   
 $\bar{n} = (-4, 11, -3)$   
 $2 = \frac{2(n^2+m^2)}{m^2n^2} \quad a \left( \frac{x+b}{2a} \right)^2 - c \frac{b^2}{4a}$   
 $(y-3)^2 \cdot 9$   
 $d = \sqrt{(x_2-x_1)^2 + (y_2-y_1)^2}$   
 $k+c=0 \quad e > 1$   
 $y^2 - 64x - 54y - 161 = 0$   
 $\left( \frac{1}{m} - \frac{1}{n} \right) \cdot \frac{(m-n)^2}{2mn}$   
 $-54y - 161 = 0$   
 $\frac{-3/2}{2/1,5} \quad \frac{10}{10} \quad \frac{10}{10}$   
 $16x^2 - 9y^2 - 64x - 54y - 161 = 0$   
 $\frac{x-x_1}{m} = \frac{y-y_1}{n} = \frac{z-z_1}{p}$   
 $16 \left( x - \frac{64}{32} \right)^2 = 16(x-2)^2 \quad \frac{(m-n)(m+n)}{2mn}$   
 $\alpha \left( \frac{x+b}{2a} \right)^2 - n$   
 $(\bar{r} = (m, n, p)) \quad \frac{4}{1} \cdot \frac{1}{mn} = \frac{4}{mn}$   
 $\frac{2(n-m)^2}{m^2n^2} \cdot y \quad A(-5, 5) \Rightarrow 5 = -k \cdot 5 + b$   
 $B(3, 1) \Rightarrow 1 = k \cdot 3 + b$   
 $V_1 + V_2 + V_3 + V_5 = V_a - r_1 \cdot I$   
 $+ V_1 + E_1 + V_2 - r_2 \cdot I +$   
 $+ V_3 - E_2$   
 $I(r_1 + r_2) = V_a - V_5 + E_1$   
 $I = \frac{V_a - V_5 + E_1 - E_2}{r_1 + r_2}$   
 $V_2 = V_3$   
 $\frac{V_3 - V_1 + E_1}{r_1} = g_1 \cdot (V_3 - V_1 + E_1)$   
 $x = \pm \sqrt{z^2 - p^2}$   
 $g = \frac{1}{r}$

# Focus:

---

# Towards Organic Polariton Devices

Anton V. Baranikov\*, Anton V. Zasedatelev, Pavlos G. Lagoudakis

---

## Abstract

Polaritons are quasiparticles arising from strong light-matter coupling possessing strong advantages of both constituents. Recent progress led to experimental demonstrations of such interesting physical phenomena as Bose-Einstein condensation, superfluidity and possibility to simulate diverse fundamental physical problems. Aside from these fundamental applications polaritons opened a road towards microscale optical devices from polariton lasers to all-optical transistor at cryogenic temperature. Necessity to work at ambient conditions has pushed polaritonics to organic matter with Frenkel excitons capable of surviving at room temperature. Here we focus on the features of organic polaritons providing for photonic technological applications and highlight the most recent remarkable experimental results.

---

## Index Terms

Bosonic stimulation; microcavity; optical amplifier; optical transistor; organic polaritonics; polariton laser; strong light-matter interaction.

---

## I INTRODUCTION

**N**OWADAYS we can clearly see how photonics change our life. Material processing, laser medicine, optical communications and biotechnology are only the tip of an iceberg. Recent breakthrough in photonics paves a way to high-tech future and outstanding technologies such as computers and optical logic circuits based on optical devices such as optical amplifiers, lasers and optical transistors. There are several reasons to replace all the conventional electronics with state-of-the-art optical technologies: 1) high-speed optical data processing; 2) low rate of energy losses and absence of heating during information transmission; 3) low energy consumption; 4) absence of the “electronic bottleneck” constraints (limit of the information processing speed due to parasitic ca-

---

\* **A. V. Baranikov** is with the Center for Photonics and Quantum Materials, Skolkovo Institute of Science and Technology, Skolkovo Innovation Center, Building 3, Moscow, 121205, Russia (e-mail: anton.baranikov@skolkovotech.ru).

**A. V. Zasedatelev**, is with the Center for Photonics and Quantum Materials, Skolkovo Institute of Science and Technology, Skolkovo Innovation Center, Building 3, Moscow, 121205, Russia.

**P. G. Lagoudakis** is with the Center for Photonics and Quantum Materials, Skolkovo Institute of Science and Technology, Skolkovo Innovation Center, Building 3, Moscow, 121205, Russia.

capacity of tightly packed electron transistor [1]) due to huge possible devices density [2]. A tendency towards the miniaturization in optical technologies [3] encouraged research in nanoscale and microscale physics like plasmonics and polaritonics arising from light-matter interaction. This phenomenon gave rise to a lot of well-known optical processes such as absorption, spontaneous and stimulated emission. However, all these cases assume negligible modification of a medium energy structure imposed by an exciting electromagnetic wave. Actually, this approximation fails when light-matter interaction becomes such a strong that new eigenstates of the medium appear and lead to a completely new physics like polaritonics mentioned above.

An outstanding pace demonstrated in this area [4]-[7] reveals high potential of polaritons as a promising platform for all-optical microscale devices.

---

## II PROPERTIES OF POLARITONS

### A. Basics

In Fig. 1 a conventional optical microcavity with just several  $\lambda/2$  length between the mirrors is depicted. Here we can confine light resulting in standing wave formation. To demonstrate an interesting physics of light-matter interactions, it is necessary to add a matter inside the cavity with a possibility to absorb confined photons. This physical process usually follows a matter excitation – an exciton, which in turn has a possibility to reemit a photon due to finite lifetime [8].

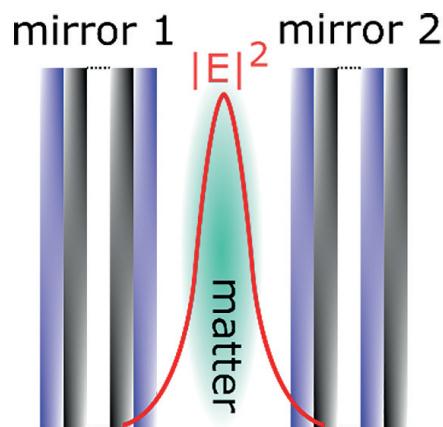


Fig. 1. A conventional microcavity schematic. Distributed Bragg reflectors act as two mirrors. The red line depicts the energy distribution of the standing wave, which intersects with matter inside.

Since the light is strongly trapped, the energy exchange between excitons and photons can be very fast. Namely, the exchange characteristic frequency  $\Omega$  should exceed two major types of energy losses in the system, defined by the cavity (photon decay  $\gamma = 1/\tau$ , where  $\tau$  is lifetime of the photon inside the cavity) and the exciton (energy loss rate  $\kappa = 1/t$ , where  $t$  is lifetime of the exciton in excited state). When this regime is

achieved, the system cannot be considered as having two separate eigenstates: bare photon and bare exciton. Instead, we must talk about two new eigenstates called upper-polariton and lower-polariton. Diagonalization of the total Hamiltonian will give the eigenenergies of new quasiparticle polariton and reveal the resulting energy splitting between lower and upper-polariton energies as shown in Fig.2.

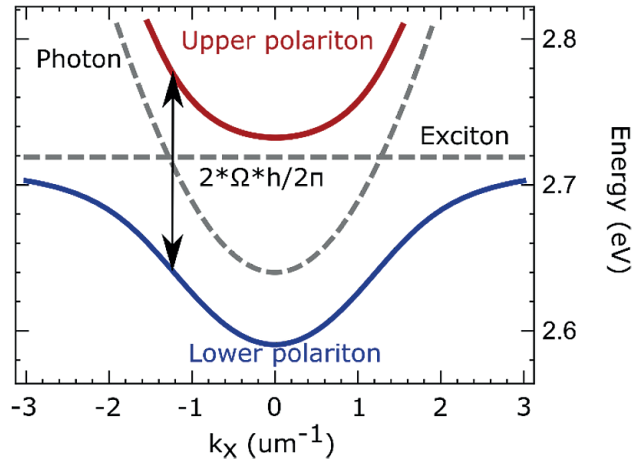


Fig. 2. Typical dispersion curves illustrating strong-light matter interaction in an optical microcavity resulting in transition from old eigenstates (exciton and photon) to new eigenstates of the system (upper polariton and lower polariton).

New eigenstates energy can be described by the following equation:

$$E_{UP/LP} = \frac{E_x + E_c}{2} \pm \frac{1}{2} \sqrt{(E_x - E_c)^2 + 4\left(\frac{\hbar}{2\pi}\right)^2 \Omega^2}, \quad (1)$$

where  $E_x$  and  $E_c$  are the exciton and photon energies, respectively.

It can be seen that the lower polariton wavefunction is a coherent superposition of initial exciton and photon wavefunctions defined as:

$$\psi_{lp} = C\psi_c + X\psi_x, \quad (2)$$

where  $|C|^2$  and  $|X|^2$  present photon and exciton fractions, respectively.

Polaritons have a very useful physical property: finite lifetime due to their photonic counterpart and leak out through the imperfect cavity mirrors in the form of photons producing photoluminescence. Using Fourier imaging of the collecting objective, experimental physicists can spectrally resolve the Fourier plane and get the dispersion directly, resulting in a picture similar to Fig. 2 on their charge coupled devices (CCD) camera.

## B. Key experimental achievements at cryogenic temperatures

Owing to integer spin, polaritons retain the bosonic nature of their constituents (excitons and photons). Thus such a phenomenon as Bose-Einstein condensation (BEC) can be expected. Bosons after some critical density or temperature can spontaneously occupy the ground state. Indeed, it was experimentally proven in

2006 [9] that after some excitation threshold an optically pumped strongly-coupled microcavity undergoes tremendous increase in photoluminescence intensity at the ground state corresponding to the lowest energy of polariton dispersion (e.g., momentum  $k_x=0$ ).

Another phenomenon definitely proving bosonic nature of polaritons is stimulated condensation, firstly demonstrated by Savvidis et al. in early 2000s [5]. His group implemented two-beam experiment (pump-probe) instead of one pump beam only and stimulated polariton condensation by another probe beam seeding the system in the ground polariton state. Moreover, they exploited stimulated polariton condensation to achieve optical amplification of the probe pulse resulting in a polariton amplifier, a brand new type of optical devices.

Inspired by this continuously developing area, the group of Sanvitto in 2013 observed all-optical transistor functionality [4]. Going further, they even managed to demonstrate optical logic gates relying on polariton propagation across the sample plane.

However, to serve as a realistic optical instrument, polariton devices should be able to operate under ambient conditions. Above works utilized inorganic microcavity structure with low binding exciton energy requiring cryogenic temperature. The desire to bring polariton devices into daily life instigated the research of organic microcavities with strongly bound Frenkel excitons.

### **C. Rise of organic polaritonics.**

The first experimental demonstration of strong light-matter interaction was achieved in 1998 [10], however the first polariton condensation was shown only in 2010 [11]. Practically, polariton condensation implies low-threshold room-temperature polariton laser operation. Since 2010, due to tremendous improvements in fabrication technologies and experimental apparatus, there have been a lot of high impact publications with polariton lasing in broad spectral range from 2.1 to 3 eV [12]-[14]. Unfortunately, weak Coulomb interactions between Frenkel excitons – rigid backbone of inorganic polariton devices – make the feasibility of polariton devices elusive. Practical applications together with fundamental investigations are still to be demonstrated in organic polaritonics.

One of the possible ways to deal with the problem is to utilize vibrons, which are quasiparticles representing collective molecular vibrations possessing strong and narrow resonances. Initial steps towards this approach have been already made both theoretically and experimentally [15]-[17]. For example, in [18] an organic microcavity was nonresonantly pumped, that is far above the exciton energy, and a photoluminescence study revealed several intensity peaks. Digging further, it has been understood that these peaks were driven by a profound role of molecular vibrons in the excitons relaxation. After relaxation from the hot exciton reservoir to cold exciton reservoir via low energy vibrational modes efficient scattering from excitons to polaritons occurred followed by the vibron emission.

---

### III. CONCLUSIONS

Huge progress of polaritonics has been demonstrated over the past decade. Some microscale polariton optical devices have been shown at cryogenic temperatures while constantly growing diversity of organic materials has already given the possibility to work at ambient conditions. Experimentalists and theoreticians have developed an exhaustive knowledge foundation both in inorganic and organic polaritonics. Based on that, further research will only bring us closer to a dramatic breakthrough in optical communication and processing.

---

### IV. REFERENCES

- [1] D. J. Richardson, "Silicon photonics: Beating the electronics bottleneck," *Nature Photonics*, vol. 3, no. 10, pp. 562–564, Oct. 2009.
- [2] D. A. Miller, "Are optical transistors the logical next step?" *Nature Photonics*, vol. 4, no. 1, pp. 3–5, Jan. 2010.
- [3] A. V. Zasedatelev, A. V. Baranikov, D. Urbonas, F. Scafirimuto, U. Scherf, T. Stöferle, R. F. Mahrt, P. G. Lagoudakis, "A room-temperature organic polariton transistor," *Nature Photonics*, vol. 13, no. 6, pp. 378–383, Jun. 2019.
- [4] D. Ballarini, M. De Giorgi, E. Cancellieri, R. Houdré, E. Giacobino, R. Cingolani, A. Bramati, G. Gigli, D. Sanvitto, "All-optical polariton transistor," *Nat. Commun.*, vol. 4, pp. 1778, Apr. 2013.
- [5] P. G. Savvidis, J. J. Baumberg, R. M. Stevenson, M. S. Skolnick, D. M. Whittaker, J. S. Roberts, "Angle-resonant stimulated polariton amplifier," *Phys. Rev. Lett.*, vol. 84, no. 7, pp. 1547–1550, Feb. 2000.
- [6] H. S. Nguyen, D. Vishnevsky, C. Sturm, D. Tanese, D. Solnyshkov, E. Galopin, A. Lemaître, I. Sagnes, A. Amo, G. Malpuech, J. Bloch, "Realization of a double-barrier resonant tunneling diode for cavity polaritons," *Phys. Rev. Lett.*, vol. 110, no. 23, pp. 236601, Jun. 2013.
- [7] F. Marsault, H. S. Nguyen, D. Tanese, A. Lemaître, E. Galopin, I. Sagnes, A. Amo, J. Bloch, "Realization of an all optical exciton-polariton router," *Appl. Phys. Lett.*, vol. 107, no. 20, pp. 201115, Nov. 2015.
- [8] A. Kavokin, J. J. Baumberg, G. Malpuech, F. P. Laussy, *Microcavities*. GB: Oxford University Press, 2017.
- [9] J. Kasprzak, M. Richard, S. Kundermann, A. Baas, P. Jeambrun, J. M. J. Keeling, F. M. Marchetti, M. H. Szymańska, R. André, J. L. Staehli, V. Savona, P. B. Littlewood, B. Deveaud, Le Si Dang, "Bose–Einstein condensation of exciton polaritons," *Nature*, vol. 443, pp. 409–414, Sept. 2006.
- [10] D. G. Lidzey, D. D. C. Bradley, M. S. Skolnick, T. Virgili, S. Walker, D. M. Whittaker, "Strong exciton–photon coupling in an organic semiconductor microcavity," *Nature*, vol. 395, pp. 53–55, Sept. 1998.
- [11] S. Kena-Cohen, S. R. Forrest, "Room-temperature polariton lasing in an organic single-crystal microcavity," *Nature Photonics*, vol. 4, no. 6, pp. 371–375, Apr. 2010.
- [12] T. Cookson, K. Georgiou, A. Zasedatelev, R. T. Grant, T. Virgili, M. Cavazzini, F. Galeotti, C. Clark, N. G. Berloff, D. G. Lidzey, P. G. Lagoudakis, "A yellow polariton condensate in a dye filled microcavity," *Adv. Opt. Mater.*, vol. 5, no. 18, pp. 1700203, Sept. 2017.
- [13] J. D. Plumhof, T. Stöferle, L. Mai, U. Scherf, R. F. Mahrt, "Room temperature Bose–Einstein condensation of cavity exciton-polaritons in a polymer," *Nat. Mater.*, vol. 13, no. 3, pp. 247–252, Dec. 2014.
- [14] C. P. Dietrich, A. Steude, L. Töpf, M. Schubert, N. M. Kronenberg, K. Ostermann, S. Höfling, M. C. Gathe, "An exciton-polariton laser based on biologically produced fluorescent protein," *Sci. Adv.*, vol. 2, no. 8, pp. e1600666, Aug. 2016.
- [15] P. Michetti, G. C. La Rocca, "Exciton–phonon scattering and photoexcitation dynamics in J-aggregate microcavities," *Phys. Rev. B*, vol. 79, pp. 035325, 2009.
- [16] L. Mazza, S. Kena-Cohen, P. Michetti, G. C. La Rocca, "Microscopic theory of polariton lasing via vibronically assisted scattering," *Phys. Rev. B*, vol. 88, pp. 075321, 2013.
- [17] D. M. Coles, P. Michetti, C. Clark, W. C. Tsoi, A. M. Adawi, J.-S. Kim, D. G. Lidzey, "Vibrationally assisted polariton-relaxation processes in strongly coupled organic-semiconductor microcavities," *Adv. Funct. Mater.*, vol. 21, no. 19, pp. 3691–3696, Oct. 2011.

# Axial Splitting in Uniaxial Compressive Testing: A Focus

Mikhail Y. Nikolaev\*

## Abstract

The main purpose of this paper is to focus on axial splitting during uniaxial compressive testing of rocks. Drillers extract cores from reservoir and cap rocks, and core analysts perform geomechanical testing of cylindrical specimens drilled out from these cores to measure the geomechanical properties of rocks. Uniaxial compression test (UCT) of rock core samples or specimens is the basic geomechanical investigation in core analysis used to analyze the process of uniaxial compressive testing. Axial splitting is a complicated failure mechanism that is normally observed during this kind of test. A short literature survey was carried out to form a solid theoretical basis on the subject. Key formulas of analytical solution for the problem simulation and the results of simulation in Matlab Simulink R2017a software were demonstrated. Readers will learn the necessary theoretical information on the axial splitting during uniaxial compressive testing of rocks, and will be given evidence that the numerical simulation of UCT is possible. The practical use of the simulation performed is described at the end of the paper.

## Index Terms

Axial splitting; core; hydraulic fracturing; uniaxial compression test; viscous-plastic deformation.

## I NOMENCLATURE

2D	two-dimensional
UCT	uniaxial compression test
$\tau$	induced shear stress (Pa)
$E$	rock elastic modulus (Pa)
$\gamma$	shear strain (-)
$\nu$	Poisson's ratio (-)
$a$	internal radius of a cylindrical shell (m)
$b$	external radius of a cylindrical shell (m)

\* **Mikhail Y. Nikolaev** is with the Space Center, Skolkovo Institute of Science and Technology, Skolkovo Innovation Center, Building 3, Moscow, 121205, Russia (e-mail: Mikhail.Nikolaev@skoltech.ru).



---

$d$	cylinder thickness (m)
$\psi$	rock dilation angle (degree)
$\sigma_t$	tensile strength of rock (Pa)
$\beta$	ratio of the thickness of a cylindrical shell to the radius of a cylindrical rock core sample (-)
$C'$	rock cohesion (Pa)
$\phi$	internal friction angle (degree)
$\phi$	porosity of the rock core sample (fraction)
$\bar{P}$	total pressure (Pa)
$P_f$	fluid pressure (Pa)

---

## II INTRODUCTION

**T**HE effectiveness of oil and gas extraction heavily depends on the amount and quality of knowledge that petroleum engineers possess about the properties of reservoir rocks containing hydrocarbons, and cap rocks preventing hydrocarbons from moving away from the reservoir. Geomechanical properties of these rocks are critical for the successful reservoir treatment during the reservoir development [1].

As a result of coring operations performed at the wellsite, a whole-sized core, that previously was a part of a reservoir or a cap rock, is obtained. This core is used as a physical model of the studied formation during the laboratory experiments [2]. Core analysts drill out cylindrical rock samples from the whole-sized cores and use them to carry out geomechanical tests. Herein, the term UCT refers to a uniaxial compression test, i.e. the experiment.

Axial splitting is the process of axial cracks propagation in rock core samples during UCT. This type of splitting and cracking is one of the possible options of the cracking process [3]. Axial splitting is interesting for investigation at the level of rock core samples due to the similarity of this process at the level of a cylindrical sample with hydraulic fracturing occurring at the level of a reservoir.

Geomechanical simulation techniques are routinely used to forecast hydraulic fracturing processes at the reservoir scale [4]. Similar simulation at the scale of a well is also often performed to predict the stability of a wellbore and any fracturing or cracking in the near wellbore area [5]. However, simulation of geomechanical tests at the scale of a rock core sample is rarely performed, although such numerical data can be directly compared with the actual laboratory measurement data to forecast the results of experiments.

This paper presents sufficient theoretical information on axial cracking during UCT and demonstrates that simulation of UCT is possible. Firstly, the basic theory of UCT is described. Secondly, a short literature review is provided. Thirdly, basic formulas of the analytical solution are presented. Finally, the results of simulation in Matlab Simulink

R2017a are delivered, and the possible application of simulation at the scale of UCT is explained.

This paper focuses on geomechanical testing in the sphere of core analysis for petroleum engineering goals.

---

### III CRACKING IN UNIAXIAL COMPRESSIVE TESTING

UCT is the basis of all geomechanical tests in core analysis. In its original form UCT can be used to study cracking of cylindrical samples, and the obtained results can be used to analyze the process of axial and radial cracks propagation in rocks. A brief explanation of UCT and corresponding literature survey are presented below.

#### A. UCT

UCT is a test when the dried core sample is placed between two platens (Fig. 1). The lower platen is fixed, and the rock core sample sits on the lower platen. The upper platen moves downwards and pressurizes the cylindrical sample until it is crushed [6]. The force and pressure values at which the sample was crushed are used to calculate the necessary geomechanical parameters.

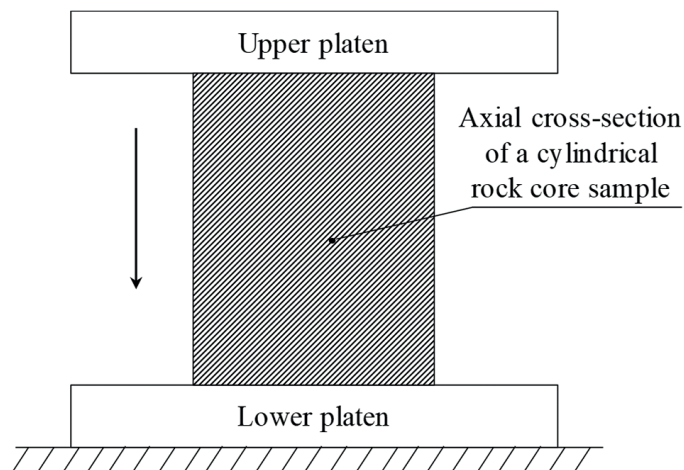


Fig. 1. Illustration of UCT.

UCT can be modified resulting in more complicated tests. In this paper, we focus on UCT as the primary available geomechanical investigation.

#### B. Articles on the Subject

The theme of axial cracking at the scale of a rock sample in UCT was highlighted in several papers in previous years.

Wawersik and Fairhurst in 1970 defined two possible failure modes: local fracturing mostly parallel to the specimen axis and both local and macroscopic shear faulting [7].

The work was continued by Holzhausen and Johnson in 1979 by the examination of UCT possibilities in induced lateral tensile stresses and axial splitting investigation. The authors raised several questions, such as the appearance of induced axial cracks and their development, sliding of an inclined internal crack, etc. [8]. Dey and Wang in 1981 considered stress inhomogeneity and crack interactions as the cause of rock fracture under compressive loading [9]. Moving to a more complex problem of the pre-existing inclined crack in the rock, Horii and Nemat-Nasser in 1985 identified the process of wing cracks extension from the tips of the pre-existing crack resulting in its final parallel orientation to the specimen free surface [10]. Bažant and Xiant in 1997 developed a fracture mechanics-based model for the compression failure of quasi-brittle materials. This paper investigates centrally or eccentrically loaded quasi-brittle columns and is important for the development of later works on axial splitting in UCT [11].

Fakhimi and Hemami in 2017 presented one of the most comprehensive papers on the subject of axial splitting in UCT [3]. Their paper is complemented by information on the Griffith theory of brittle failure from Paterson and Wong [12]. These two manuscripts are considered in more detail below.

### **C. Review of the Article by Fakhimi and Hemami**

The article by Fakhimi and Hemami proposes a theory for axial splitting in terms of axial shear cracks appearance as a result of non-uniform deformation of rock core sample ends. The paper consists of the theoretical background with a good observation of formulas stating the problem, supporting experimental research and a proposal of the simple model representing the plasticity-fracture mechanics. The theoretical explanation of axial crack appearance during UCT is the result of many corresponding processes and is therefore quite complicated [3].

For experiments, a rock core sample is loaded in a geomechanical apparatus for UCT. A non-uniform deformation at the core sample ends occurs as a result of their interaction with the end platens. Thus, the failure appears within the specimen along the surfaces of thin cylindrical shells. This failure, or dislocation, and dilation along shear planes induce lateral radial stress. Such lateral radial stress is believed to be the cause of radial cracking and subsequent surface spalling.

When a cylindrical rock core sample is pushed by a loading platen, induced contact stresses and the displacement at the interface between the platen and the sample are not uniform (based on the theory of elasticity). The non-uniform penetration of the core sample ends into the loading platens and the existence of the interface friction cause induced shear stresses. Thus, the specimen ends are envisioned of several thin overlapped cylindrical shells. Then the shear deformation results in the shear cracking associated with dilation. The induced dilation itself provides radial stress and radial cracking followed by surface spalling of the cantilever rock pieces.

Further loading causes the ends of the rock core sample to turn to the form-factor of short cylinders or cones with decreased radius. These cylinders or cones tend to punch through in the axial direction resulting in the appearance of axial cracks (Fig. 2).

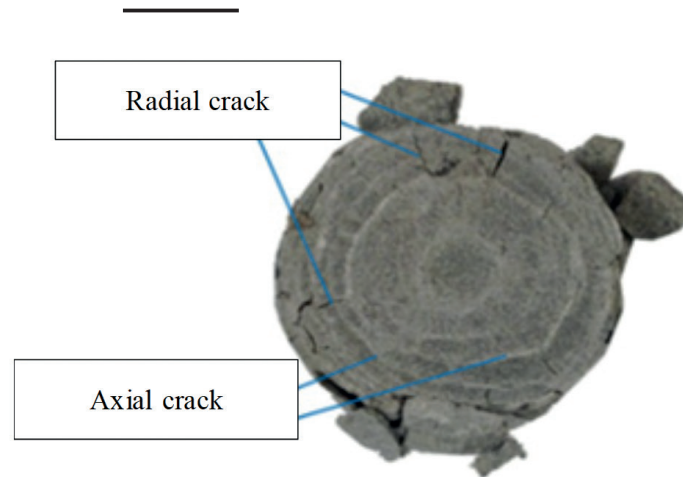


Fig. 2. Radial and axial cracks at the rock core sample ends after the carried out UCT [3].

The authors link the results of their experimental investigations with numerical simulation and a theoretical model. The basis of this theoretical model lies in the induced shear stress equation based on the Hooke's Law:

$$\tau = \frac{E_{\gamma}}{2(1 + \nu)} = \frac{E \tan(\theta)}{2(1 + \nu)}, \quad (1)$$

where  $\theta$  is the angle in the cross-section of a produced cylindrical shell (Fig. 3).

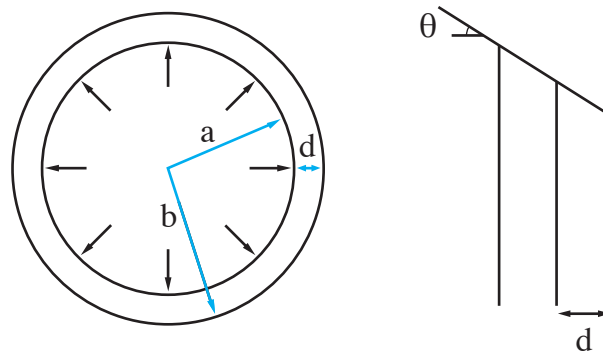


Fig. 3. The cylindrical shell (left) and its cross-section (right) [3].

Fakhimi and Hemami further develop their theoretical solution by considering the formulas for stress and strain fields in case of a hollow cylinder and implementing geometrical equation for the cylindrical shell and its cross-section. As a result of the final complex relationship between the axial shear strain and the minimum thickness of the cylindrical shell, at which the first radial crack is to be developed, the following formula is established:

$$\tan(\theta) = \frac{1}{d \tan(\psi)} \cdot \frac{a}{a^2 + b^2} \cdot \frac{\sigma_t}{E} \cdot (a^2(1 - \nu - 2\nu^2) + b^2(1 + \nu)), \quad (2)$$

where  $\tan(\theta)$  is the axial shear strain.

The derived final equation for the ratio of the thickness of a cylindrical shell to the radius of a cylindrical rock core sample is as follows:

$$\beta = \frac{1}{1 + \frac{2C'\tan(\psi)}{\sigma_t}} \quad (3)$$

The obtained equation (3) allows predicting the necessary ratio value.

Fakhimi and Hemami presented a profound and comprehensive (both theoretical and experimental) investigation in the field of axial splitting during UCT. Their findings can be useful for other researchers especially in terms of the delivered theoretical model.

An important case of brittle failure in axial splitting during UCT is described below.

#### **D. Review of the Book Chapter by Paterson and Wong**

One more important source containing theoretical information on the process of axial splitting during UCT is a book chapter on Griffith theory of brittle failure by Paterson and Wong [12].

The Griffith theory of brittle failure itself is important to explain the mechanism of initial crack appearance, and it is based on two provisions. The first one is that the initial presence of small cracks governs the strength of brittle material. The second states that failure occurs when the most vulnerably oriented crack in a population extends under the applied crack.

Paterson and Wong notice that the extension of a crack occurs when the maximum tensile stress component of any point around the crack reaches the critical value needed to overcome the interatomic cohesion of the material.

To support the explanation, the macroscopic criterion of failure, known as the Griffith criterion, was established and presented in the book. The consequence of this criterion states that there is a tendency for a crack to propagate out of its plane under predominantly compressive conditions. Failure criterion is supposed to be the sum of the surface energy of a new crack, the change in the elastic strain energy of the body and the change in the potential energy of the loading system. The sum of these components is supposed to be of a zero or a negative value.

In a particular case of UCT, two issues arise. The first one is that there are pieces of evidence opposed to the proposal that the crack during UCT should extend in its plane. The second is about that the width of the crack is not negligible as it will tend to close under the certain compressive conditions.

Hence, it can be understood that under certain loading conditions during UCT cracking that appears in a rock core sample can result in axial splitting. When these conditions are overcome, cracks can appear in the plane different than the axial one. Thus, UCT is similar to hydraulic fracturing. The main two differences between them are as follows: UCT possesses geostatic (axial) loading but lacks lithostatic (overburden) pressure, and it does not have any liquid fluid in the pore space of rock core samples. Therefore, for UCT internal (pore) pressure is neglected.

The information from the article by Fakhimi and Hemami and the book chapter by Paterson and Wong serves as good theoretical support in the simulation of axial splitting during UCT.

---

## IV AXIAL CRACK APPEARANCE SIMULATION

The simulation of axial crack appearance during UCT was conducted using Matlab Simulink R2017a software. Only specific cracks that appeared in the axial plane were considered. The main purpose of the task was to understand whether the simulation of axial cracking process was possible or not.

### A. Problem Statement and Conditions for Simulation

The purpose of simulation was to finally obtain axial splitting the way it was to occur during UCT (Fig. 1).

According to the conducted literature survey it can be assumed that axial splitting during UCT is similar to the solution of hydraulic fracturing problem. However, the difference is significant. Firstly, in hydraulic fracturing, the formation fractures due to the increase in internal pressure (internal action). Alternatively, during UCT the acting force is external. Secondly, in hydraulic fracturing, the acting fluid is to be of liquid origin (brine or oil). In UCT, it is the air in the pores that has the function of the “fluid”.

Hence, the problem of simulation consists of coding the similar process to hydraulic fracturing but with the following changes:

1) the density of the “fluid” in the pore space is equal to that of air;

2) pressurizing force in the rock core sample for UCT is vertical and directed downwards. Its starting point is located in the upper point of the rock core sample. For UCT pressure change affects the interior part of the sample. For hydraulic fracturing, pressurizing force acts horizontally having the initial point in the inside part of the formation and directed towards its exterior parts.

Main conditions for simulation are listed below (see Table I).

TABLE I. Conditions for Numerical Simulation in Matlab Software

No	Value	Explanation
1	Viscous-plastic deformation (“lazy” plasticity)	Viscosity change is considered to be the key factor. For “true” plasticity additional (different) formulas are to be considered.
2	Velocities: $V_x, V_y$	The lower platen is fixed. The upper one is moving down with the constant velocity. There is no movement along the x-axis.
3	Rock properties	All values are taken similar to that of sandstone.

Simulation in 2D is the option to be chosen as it vividly depicts cracking along the axial cross-section of the cylindrical rock core sample. The diameter of the cylinder is aligned with the x-axis as well as its height – with the y-axis. Thus, all the processes are simulated in the plane of axial cross-section possessing the 20 x 40 ( $x = 20, y = 40$ ) rectangular numerical grid.

The simulation of axial cracking during UCT also requires the knowledge of at least basic formulas for analytical solution.

### B. The Basis of Analytical Solution

The basis of analytical solution required for further numerical simulation consists of formulas used to establish the yield surface in the numerical model and to describe viscous-plastic deformation and the fluid movement in the numerical model of a rock core sample.

Established yield surface provides the numerical model with yield functions for failure in tension and in shear [12]:

$$f_{tension} = \tau' - \sigma'_m - \sigma_T, \tag{4}$$

$$f_{shear} = \tau' - \sigma'_m \sin(\phi) - C' \cos(\phi), \tag{5}$$

where  $f_{tension}$  and  $f_{shear}$  are yield functions for tension and shear respectively;  $\tau'$  is the stress deviator (Pa);  $\sigma'_m$  the main effective stress (Pa).

For the case of viscous-plastic deformation, the following formula is taken as the basis [13]:

$$\frac{d\phi}{dt} = \frac{\bar{P} - P_f}{\eta_s}, \tag{6}$$

where  $d\phi/dt$  is the incremental change of rock porosity in respect to time steps in numerical simulation;  $\eta_s$  – viscosity of the solid fraction (rock).

To describe the fluid movement the Darcy Law formula [14] and Navier-Stokes equations [15] are used.

### C. Matlab Coding Sequence

The produced code for numerical simulation in Matlab Simulink R2017a software consists of five stages (Fig. 4).

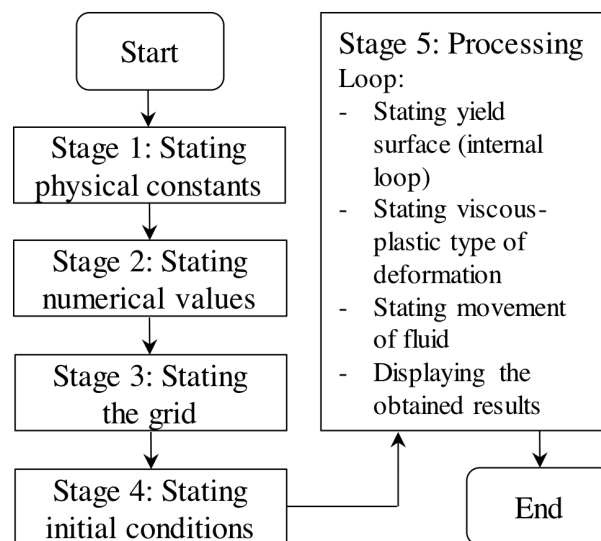


Fig. 4. Schematic block-diagram of Matlab code.

Change of rock porosity is used to represent the results of simulation as it is the direct indicator of deformation and cracking.

## D. Numerical Simulation Results

Obtained results are separated into two cases based on the initial conditions:

Case 1: the simulated cross-section of a rock core sample possesses uniform porosity value with one initial big pore, from which the cracking process starts. It allows simulating the process of cracking the way it may occur in the real sample with voids.

Case 2: porosity value is randomized along the simulated cross-section. It allows simulating the process of cracking the way it may occur in the real sample with high heterogeneity of petrophysical properties.

Graphical results of simulation for cases 1 (Fig. 5) and 2 (Fig. 6) are presented below.

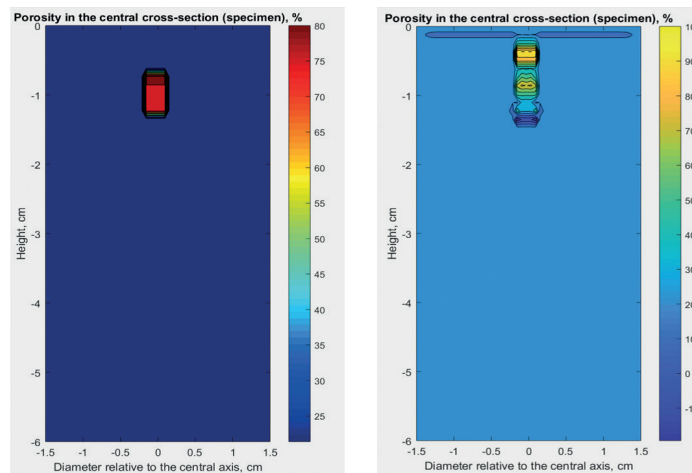


Fig. 5. Numerical simulation of axial splitting during UCT in case of one big initial pore (case 1): initial condition (left) and the appearance of radial cracks (right).

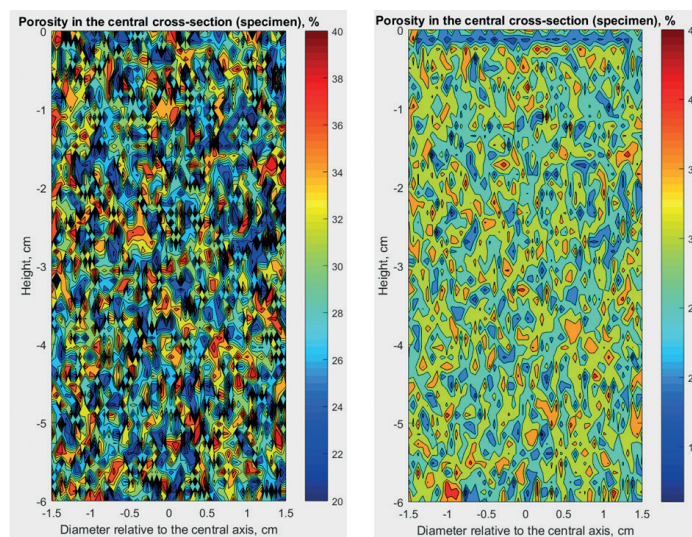


Fig. 6. Numerical simulation of axial splitting during UCT in case of randomized porosity (case 2): initial condition (left) and the appearance of radial cracks (right).

In both cases the numerical simulation results in the appearance of the horizontal zone with a uniform value of porosity equal to 20-25%, which means the appearance of radial cracks. According to the theory [3], the appearance of radial cracks will finally lead to axial cracking. Thus, it is potentially possible



to simulate the process of axial cracking at the scale of a cylindrical rock core sample.

Obtaining axial cracks and splitting as a result of further simulation requires the consideration of mathematical errors appearing during the simulation, which is a matter of a “lazy plasticity” approach (see Table I). For example, in Fig. 5 negative values of porosity are the result of such mathematical errors that can be avoided by using the “true plasticity” approach in the future.

### **E. Application of Simulation at the Scale of UCT**

Simulation at the scale of UCT is a useful operation as it potentially allows performing cross-validation and preventing expensive geomechanical laboratory equipment from the unnecessary use.

Performing cross-validation of the expected laboratory measurement results and the actually obtained values in the future will allow optimizing the specimen preparation procedure for UCT. If no positive result of the test is expected or no additional useful information is predicted to be obtained by numerical simulation, then there will be no need to carry out UCT on particular rock core samples. Considering the total breakage of specimens as a result of UCT, it will allow to economy financial budget of a core research center by avoiding the preparation of unnecessary samples.

Thus, the demonstrated possibility of numerical simulation of UCT at the scale of a rock core sample allows undertaking the practical tasks of economizing the financial budget of a core research center or a laboratory.

---

## V CONCLUSIONS

The purpose of the paper was to focus on the question of axial splitting during UCT. Its practical use for the readers consists of providing with the basic theory on axial splitting and cracking and demonstrating the possibility to perform simple numerical simulation of UCT. Ideally, it was important to reach axial splitting as a result of numerical simulation.

Several literature sources were listed and two of them were carefully analyzed to present processes and formulas that occur during axial splitting in UCT.

A numerical simulation of cracking occurring during UCT in a cross-section of a cylindrical rock core sample was performed. The results proved that it was possible to simulate UCT until the moment when radial cracks appeared. Further simulation leading to axial splitting was omitted due to the influence of appeared mathematical errors.

Numerical simulation of UCT was proposed to be a useful tool that allows performing cross-validation and avoiding the unnecessary use of expensive geomechanical equipment.

---



---

## VI ACKNOWLEDGMENT

The author gratefully acknowledges prof. Artyom Myasnikov for the information delivered during the “Geomechanics and Hydraulic Fracturing” course, prof. Elizaveta Tikhomirova for the high quality English language revision and prof. Clément Fortin as his supervisor for the permission to publish this paper.

---

## V REFERENCES

- [1] M. D. Zoback, “The tectonic stress field,” in *Reservoir Geomechanics*, 1<sup>st</sup> ed. New York: Cambridge University Press, 2010, pp. 3–4.
- [2] I. A. Vahrusheva, Y. I. Gilmanov, M. U. Nikolaev, M. I. Zagidullin, “Integrated laboratory research procedure for core cavernous samples,” presented at the SPE Russian Petroleum Technology Conference, Moscow, Russia, October 15–17, 2017.
- [3] A. Fakhimi, B. Hemami, “Rock uniaxial compression test and axial splitting,” *Procedia engineering*, vol. 191, pp. 623–630, 2017.
- [4] M. Bagheri, A. Settari, “Modeling of geomechanics in naturally fractured reservoirs,” presented at the SPE Reservoir Simulation Symposium, The Woodlands, Texas, January 31 – February 2, 2005.
- [5] J.-M. Carvajal Jiménez, L.-C. Valera Lara, A. Rueda, N.-F. Saavedra Trujillo, “Geomechanical wellbore stability modeling of exploratory wells-study case at middle Magdalena Basin,” *CT&F-Ciencia, Tecnología y Futuro*, vol. 3, no. 3, pp. 85–102, 2007.
- [6] K. Mogi, “Precise measurements of fracture strength of rocks under uniform compressive stress,” in *Experimental Rock Mechanics*, 1st ed. (Geomechanics Research Series, no. 3) Leiden, The Netherlands: CRC Press, 2007, pp. 3–4.
- [7] W. R. Wawersik, C. Fairhurst, “A study of brittle rock fracture in laboratory compression experiments,” *Int. J. Rock Mech. Mining Sci. & Geomech. Abs.*, vol. 7, no. 5, pp. 561–575, Sept. 1970.
- [8] G. R. Holzhausen, A. M. Johnson, “Analyses of longitudinal splitting of uniaxially compressed rock cylinders,” *Int. J. Rock Mech. Mining Sci. & Geomech. Abs.*, vol. 16, no. 3, pp. 163–177, 1979.
- [9] T. N. Dey, C.-Y. Wang, “Some mechanisms of microcrack growth and interaction in compressive rock failure,” *Int. J. Rock Mech. Mining Sci. & Geomech. Abs.*, vol. 18, no. 3, pp. 199–209, 1981.
- [10] H. Horii, S. Nemat-Nasser, “Compression-induced microcrack growth in brittle solids: Axial splitting and shear failure,” *J. Geophys. Res.: Solid Earth*, vol. 90, no. B4, pp. 3105–3125, 1985.
- [11] Z. P. Bažant, Y. Xiang, “Size effect in compression fracture: splitting crack band propagation,” *J. Eng. Mech.*, vol. 123, no. 2, pp. 162–172, 1997.
- [12] M. S. Paterson, T.-f. Wong, “Griffith theory of brittle failure,” in *Experimental Rock Deformation – the Brittle Field*, 2<sup>nd</sup> ed. Heidelberg, The Netherlands: Springer, 2005, pp. 45–51.
- [13] V. M. Yarushina, Y. Y. Podladchikov, “(De) compaction of porous viscoelastoplastic media: Model formulation,” *J. Geophys. Res.: Solid Earth*, vol. 120, no. 6, pp. 4146–4170, 2015.
- [14] D. Tiab, E. C. Donaldson, “Applications of Darcy’s Law,” in *Petrophysics: Theory and Practice of Measuring Reservoir Rock and Fluid Transport Properties*, 2nd ed. Burlington: Gulf Professional Publishing, 2004, pp. 416–420.
- [15] G. T. Mase, G. E. Mase, “Classical fluids,” in *Continuum Mechanics for Engineers*, 2<sup>nd</sup> ed. Boca Raton: CRC Press LLC, 1999, pp. 298–300.

---

# Polariton Lasing in Organic-Based Microcavities

T. F. Yagafarov\*, D. A. Sannikov, P. G. Lagoudakis

---

## Abstract

Polariton is a bosonic quasiparticle which arises from the coherent superposition of exciton and photon confined in the microcavity. Above a threshold density polaritons form a condensate occupying the same quantum state, and lasing is observed from the microcavity. Polariton lasers based on organic materials are promising systems for augmented reality, and due to advantages of organics they can be utilized as a microdisplays and scanning lasers with retinal projection. In this paper we focus on polariton lasing phenomena in organic filled microcavities. In particular, we explain polaritonics principles and consider the strong coupling criterion, which is a crucial condition for the polariton lasing. The polariton lasing process is described. We discuss the pioneering works and the first observations of organic polariton lasing realized at room temperatures on various types of organic materials. In addition, the realization of tunable polariton laser is mentioned.

---

## Index Terms

Organic microcavity; polariton lasing; strong coupling.

---

## I NOMENCLATURE

DBR	Distributed Bragg Reflector
UPB	Upper Polariton Branch
LPB	Lower Polariton Branch
$\Omega$	Rabi frequency
$\gamma$	Exciton dissipation in microcavity
$\tau$	Photon dissipation in microcavity
$M(k)$	Interaction matrix
$E_x(k)$	Exciton resonance

---

\* **T. F. Yagafarov** is with the Center for Photonics and Quantum Materials, Skolkovo Institute of Science and Technology, Skolkovo Innovation Center, Building 3, Moscow, 121205, Russia (e-mail: timur.yagafarov@skolkovotech.ru).

**D. A. Sannikov** is with the Center for Photonics and Quantum Materials, Skolkovo Institute of Science and Technology, Skolkovo Innovation Center, Building 3, Moscow, 121205, Russia.

**P. G. Lagoudakis** is with the Center for Photonics and Quantum Materials, Skolkovo Institute of Science and Technology, Skolkovo Innovation Center, Building 3, Moscow, 121205, Russia.

$E_c(k)$	Photon resonance
$\hbar\Omega$	Rabi energy
$\psi_{UP/LP}$	UP/LP Upper/Lower Polariton wavefunction
$\psi_c$	Photon wavefunction
$\psi_x$	Exciton wavefunction
$ X ^2$	Exciton fraction
$ C ^2$	Photon fraction

## II INTRODUCTION INTO ORGANIC POLARITONICS

**F**OR more than half of the century lasers have been an inseparable part of our life. They are widely used in different areas such as energy, communications, medicine, microscopy, spectroscopy, and others. One of the most futuristic and intriguing applications of the lasers is augmented reality [1], [2]. Various huge companies have put a lot of efforts to create the augmented reality glasses such as Microsoft “HoloLens 2” [3], Google “Glass X” [4], Epson “Moverio BT-300” [5], etc. There are different expensive and complicated technical realizations for such devices, and the most promising nowadays are micro-displays and scanning lasers with retinal projection [6], where tunability of the light sources is the crucial parameter. These technologies caused the demand in the microscale light sources with rich colors. This demand can be satisfied by polariton lasers based on organic microcavities. This type of lasers has numerous technological advantages based on the properties of the organic materials, such as high quantum yield and broad spectral tunability. The micron thickness of those devices and cheap nonepitaxial growth on different substrates make them attractive for micro-displays and laser technology with retinal projection.

To understand the principles of organic polariton laser, the explanation for the polariton is needed first. Consider the microcavity which consists of two high-reflectivity mirrors,

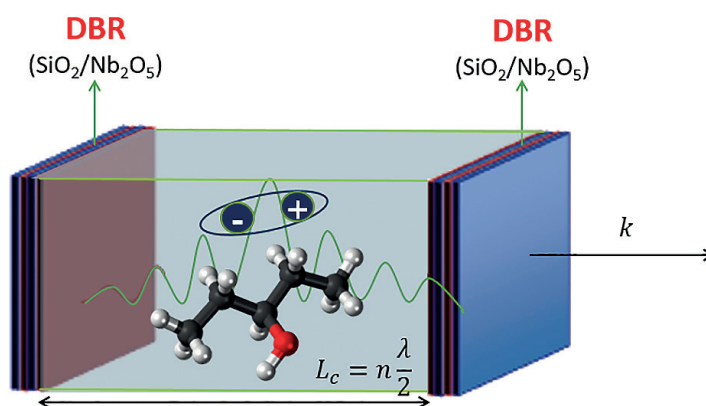


Fig. 1. Schematic representation of multi-lambda half microcavity filled with organic material. Green wave – confined optical field, blue ellipse – organic material exciton.  $k$  – wavevector of the emission from the cavity.

typically represented by Distributed Bragg Reflectors (DBR) composed from several layers of  $\text{SiO}_2/\text{Nb}_2\text{O}_5$  (see Fig. 1).

The distance between the DBRs should be multi-lambda half to confine an optical field inside the cavity. To couple optical field with some excitation an active medium, for example, organic material, inserted in the cavity. When the photons are injected in the system they could be absorbed by the medium and exciton created. After some time exciton will relax and emit the photon again. This process of energy exchange can happen very fast. If the exchange characteristic – coupling strength  $\Omega$ , called Rabi frequency, is bigger than any dissipations in the system ( $\gamma$  – exciton and  $\tau$  – photon dissipations caused by finite lifetimes), two new modes will appear – upper (UPB) and lower polariton branches (LPB) which are schematically shown in Fig. 2.

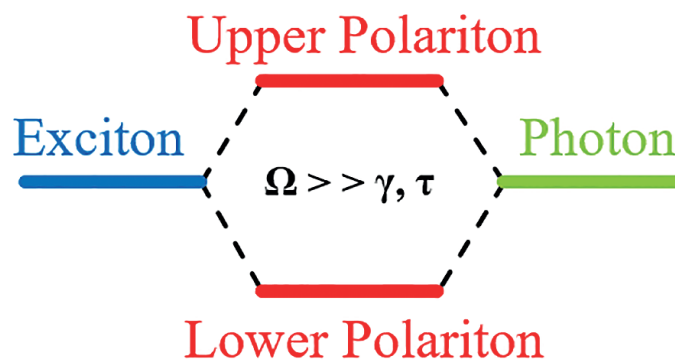


Fig. 2. Schematic representation of Exciton (blue), Photon (green) and Upper/Lower Polariton (red) branches. To observe new polariton modes, strong coupling condition (formula inset) is required.

Thus, it is clear that in a strong coupling condition, the new half-light half-matter quasiparticle occurs in microcavity, and it is called polariton. Once the strong coupling regime achieved, there is an opportunity to observe emission of polaritons, in the form of photons, which are leaking from the cavity with different wavevectors  $k$ . This process is very similar to the coupled harmonic oscillator problem when one has two pendulums coupled with the spring. If the spring constant is higher than any oscillation dissipation of pendulums, then we will find that they oscillate with the different frequencies than each pendulum individually.

To find the new eigenstates of the system, an interaction matrix should be considered:

$$M(k) = \begin{vmatrix} E_x(k) & \hbar\Omega \\ \hbar\Omega & E_c(k) \end{vmatrix}, \quad (1)$$

where  $E_c$  – the cavity resonance,  $E_x$  – exciton resonance and  $\hbar\Omega$  – Rabi energy. After the diagonalization of the interaction matrix we will get two new states for LPB and UPB which are given with equations:

$$E_{UP/LP}(k) = \frac{E_x(k) + E_c(k)}{2} \pm \frac{1}{2} \sqrt{(E_c(k) - E_x(k))^2 + 4\hbar^2\Omega^2}, \quad (2)$$

and now it is clear that polariton is a superposition of two initial states. The polariton wavefunction, in that case, could be written as follows:

$$\psi_{UP/LP} = |X_{UP/LP}|^2 \psi_x + |C_{UP/LP}|^2 \psi_c, \quad (3)$$

where  $|X|^2$  and  $|C|^2$  are the Hopfield coefficients, that represent the photon and exciton fractions of the polariton at lower/upper polariton branches.

Summarizing the information above: from eq. (3) it is clear that polariton is the superposition of both exciton and photon states, and if the structure supports a strong coupling regime, the polariton lasing could be observed from the microcavity. When the structure is pumped electrically or optically, the new eigenstates are formed and polaritons populate this states. Initially, while increasing the pump fluence, only spontaneous polariton emission observed, but after some threshold density polaritons scatter to the bottom of LPB due to bosonic stimulation. It means that large population of polaritons accumulated in the same energy state and they form a macroscopic coherent condensate in the ground polariton state, which can decay through the microcavity mirrors in the form of photons. Thus, coherent emission from the microcavity is observed, and it is called polariton lasing. From eq. (2) it is clear that the LPB energy could be changed, if we change any components which it depends on. For example, the cavity mode could be controllably changed via distance between the DBRs during the fabrication processes, hence, polariton modes will be also modified and, finally, lasing with preferred wavelengths could be obtained.

---

### III ORGANIC POLARITON LASING OBSERVATIONS

Before '90s polaritonics mainly developed within inorganic structures. Wannier–Mott nature of the excitons [7], [8] in inorganic systems led to low exciton binding energies, that is why cryogenic temperatures required for inorganic structures. However, in organic systems we meet with Frenkel type of excitons [9], which feature is high binding energies. That is why, in 1998, Lidzey et al. observed the strong coupling in an organic microcavity for the very first time at room temperatures [10]! In their work, they observed the mode splitting on the angular reflectivity measurements of the cavity and strong coupling was supported by anticrossing of these modes at a defined angle. On that stage, the possibility of polariton lasing at room temperatures was only mentioned, and it took more than a decade to demonstrate it.

In 2010, the first polariton lasing was observed on crystalline anthracene film by Kena-Cohen and Forrest [11]. It was shown that after some threshold the non-linear polariton lasing phenomenon takes place and is accompanied by a dramatic increase in emission intensity and linewidth narrowing. This work has triggered intense studies of the various organic materials application in polaritonics. The next material applied for polariton lasing observation was conjugated MeLPPP polymer, and in 2013 Plumhof et al. produced a comprehensive set of experimental evidence for polariton lasing [12]. The important fact here is that the emergence of long-range phase coherence was

proved by interferometry measurements: the polariton emission sent into a Michelson interferometer and interference pattern of the inverted image, overlapped with the original one, was obtained.

Strongly coupled organic microcavities, developed to date, filled with various organic materials – oligofluorenes [13], molecular dyes [14], [15], crystalline organic molecules [11], [16], J-aggregates [17] and conjugated polymers [12]. In 2016, Dietrich et al. realized polariton lasing also on organic microcavity filled with biologically produced fluorescent protein [18]. All the organic polariton lasing observed to date can cover the biggest part of the visible range from 2.1 up to 3 eV. But in the biggest part of these works lasing observed only in a narrow spectral range. As it was mentioned in the beginning, augmented reality technologies caused the demand in laser sources with wide color range, and polariton lasers can be fitted here. Recently, it has been demonstrated by our group that it is possible to generate polariton lasing at room temperature over a broad spectral range in frames of one material system. We utilized the boron-dipyrromethene filled organic microcavity with gradually changed detuning and were able to observe lasing in green-yellow portion of visible spectrum [15].

---

## IV CONCLUSIONS

Since polariton lasing based on organics is a rapidly developed topic in the last decade, scientific groups all over the world are investigating the different materials and utilizing all kinds of architectures for the microcavities. In the past decade, a number of articles have been published where authors discovered various types of organics and demonstrated a lasing of the polaritonic structures. We should note that in Section III of present paper only the first published representative for each type of organic materials is mentioned, but there are a lot of studies (which have not been covered here) on each type of material. Polariton lasing achieved over a broad spectral range spanning 2.1-3 eV, and the tunable control over the emission wavelength shown to date. We believe that the development of the tunable polariton lasers based on strongly coupled organic microcavities will pave the way for microdisplays and retinal laser projectors for deep color augmented reality applications.

---

## V ACKNOWLEDGMENTS

The authors acknowledge the supported by the U.K. Engineering and Physical Sciences Research Council (EPSRC) via Programme Grant EP/M025330/1 (Hybrid Polaritonics), the Skoltech NGP Program (Skoltech-MIT joint project), and the Russian Scientific Foundation (RSF) grant No. 18-72-00227.

## VI REFERENCES

- [1] A. B. Craig, *Understanding Augmented Reality: Concepts and Applications*, 1st ed. Morgan Kaufmann: San Francisco, CA, USA, 2013, pp. 69–124.
- [2] R. T. Azuma, "A survey of augmented reality," *Presence: Teleoperators and Virtual Environments*, vol. 6, no. 4, pp. 355–385, Aug. 1997.
- [3] G. Evans, J. Miller, M. I. Pena, A. MacAllister, E. Winer, "Evaluating the Microsoft HoloLens through an augmented reality assembly application," in *Proc. SPIE*, vol. 10197, 2017, pp. 101970V-1–101970V-16.
- [4] Glass Enterprise Edition, "Helping people work faster and safer with smart glasses," 2018. [Online]. Available: <https://x.company/projects/glass/>.
- [5] Epson exceed your vision, "A whole new way of seeing the world," 2018. [Online]. Available: <https://www.epson.eu/products/see-through-mobile-viewer/moverio-bt-300>.
- [6] R. L. S. Silva, J. C. Oliveira, G. A. Giralardi, "Introduction to Augmented Reality" (Technical Report 25/2003). *National Laboratory for Scientific Computation*, Petrópolis, Brazil.
- [7] D. W. Snoke, J. Keeling, "The new era of polariton condensates," *Phys. Today*, vol. 70, no. 10, p. 54, Oct. 2017.
- [8] D. Sanvitto, S. Kéna-Cohen, "The road towards polaritonic devices," *Nat. Mater.*, vol. 15, pp. 1061–1073, Jul. 2016,
- [9] G. D. Scholes, G. Rumbles, "Excitons in nanoscale systems," *Nat. Mater.*, vol. 5, pp. 683–696, Sept. 2006.
- [10] D. G. Lidzey, D. D. C. Bradley, M. S. Skolnick, T. Virgili, S. Walker, D. M. Whittaker, "Strong exciton–photon coupling in an organic semiconductor microcavity," *Nature*, vol. 395, pp. 53–55, Sept. 1998.
- [11] S. Kéna-Cohen, S. R. Forrest, "Room-temperature polariton lasing in an organic single-crystal microcavity," *Nature Photonics*, vol. 4, no. 6, pp. 371–375, Apr. 2010.
- [12] J. D. Plumhof, T. Stöferle, L. Mai, U. Scherf, R. F. Mahrt, "Room temperature Bose–Einstein condensation of cavity exciton-polaritons in a polymer," *Nat. Mater.*, vol. 13, no. 3, pp. 247–252, Dec. 2014.
- [13] K. S. Daskalakis, S. A. Maier, R. Murray, S. Kéna-Cohen, "Nonlinear interactions in an organic polariton condensate," *Nat. Mater.*, vol. 13, pp. 271–278, Feb. 2014.
- [14] T. Cookson, K. Georgiou, A. Zasedatelev, R. T. Grant, T. Virgili, M. Cavazzini, F. Galeotti, C. Clark, N. G. Berloff, D. G. Lidzey, P. G. Lagoudakis, "A yellow polariton condensate in a dye-filled microcavity," *Adv. Opt. Mater.*, vol. 5, no. 18, pp. 1700203, Sept. 2017.
- [15] D. Sannikov, T. Yagafarov, K. Georgiou, A. Zasedatelev, A. Baranikov, Z. Shen, D. Lidzey, P. Lagoudakis, "Room temperature broadband polariton lasing from a dye-filled microcavity," *Adv. Opt. Mater.*, vol. 3, pp. 1900163, Mar. 2019.
- [16] C. Zhang, C.-L. Zou, Y. Yan, R. Hao, F.-W. Sun, Z.-F. Han, Y. S. Zhao, J. Yao, "Two-photon pumped lasing in single-crystal organic nanowire exciton polariton resonators," *J. Am. Chem. Soc.*, vol. 133, no. 19, pp. 7276–7279, Apr. 2011.
- [17] G. G. Paschos, N. Somaschi, S. I. Tsintzos, D. Coles, J. L. Bricks, Z. Hatzopoulos, D. G. Lidzey, P. G. Lagoudakis, P. G. Savvidis, "Hybrid organic-inorganic polariton laser," *Sci. Rep.*, vol. 7, pp. 11377, Sept. 2017.
- [18] C. P. Dietrich, A. Steude, L. Tropic, M. Schubert, N. M. Kronenberg, K. Ostermann, S. Höfling, M. C. Gathe, "An exciton-polariton laser based on biologically produced fluorescent protein," *Sci. Adv.*, vol. 2, no. 8, pp. e1600666, Aug. 2016.









$$\frac{(n-m)^2}{m^2 n^2} \cdot \frac{(m-n)^2}{2mn} \cdot \frac{54}{-18} = \frac{2(n-m)^2}{m^2 n^2} \cdot \frac{(m-n)(m-n)}{2mn} \cdot \frac{c=3}{a=2}$$

$$\frac{(x-2)^2}{9} - \frac{(y-3)^2}{16} = 1 \quad e = \frac{c}{a}$$

$$9\left(y - \frac{54}{18}\right)^2 - (y-3)^2 = 16(x-2)^2 - 9(y-3)^2 = 1$$

$$\frac{(x-2)^2}{9} - \frac{(y-3)^2}{16} = 1 \quad 1) \frac{1}{n} - \frac{1}{m} = \frac{m-n}{mn}$$

$$2) \frac{2}{m^2} \cdot \frac{2}{n^2} = \frac{2n^2}{m^2 n^2} = \frac{2m^2}{m^2 n^2}$$

$$\frac{(x+2)^2}{2a} - c = \frac{b^2}{4a}$$

$$\frac{(x_1 - x_2)^2}{2a} + (y_2 - y_1)^2$$

$$Ex. c=6, a=3$$

$$e = \frac{c}{a} = \frac{6}{3} = 2$$


$$16x^2 - 64x - 161 = 0$$

$$\frac{x - x_1}{m} = \frac{y - y_1}{n} = \frac{z - z_1}{p}$$

$$\frac{(x-2)^2}{9} - \frac{(y-3)^2}{16} = 1$$

**Skoltech**  
Skolkovo Institute of Science and Technology

Skolkovo Institute of Science and Technology  
Skolkovo Innovation Center, Building 3  
[www.skoltech.ru/en](http://www.skoltech.ru/en)



$16(x - \frac{64}{32})^2 = 16(x-2)^2$

$(\bar{r} = (m, n, p)) \quad \frac{4}{1} \cdot \frac{1}{mn} = \frac{4}{mn}$

$\frac{2(n-m)^2}{m^2 n^2} \cdot \frac{A(-5, 5) \Rightarrow 5 = -k \cdot 5 + b \Rightarrow k = -\frac{1}{2}, b = \frac{5}{2}$

$B(3, 1) \Rightarrow 1 = k \cdot 3 + b \Rightarrow b = \frac{5}{2}$

